Atomic clusters in intense laser fields

Emma Louise Springate

Thesis submitted in partial fulfilment of the requirements for the degree of Doctor of Philosophy of the University of London

March 1999

Laser Consortium
Blackett Laboratory
Imperial College
Prince Consort Road
London SW7 2BZ
United Kingdom

Abstract

We have examined the energy distributions of ions and electrons ejected in the interaction of clusters of several thousand noble-gas atoms with high-intensity (10^{14}-10^{16} Wcm^{-2}) femtosecond laser pulses. The dependence of the ion energies on laser intensity and wavelength, cluster size and cluster medium has been studied. Ion energies of up to 1 MeV and electron energies of up to 2.5 keV have been measured. The interaction with clusters is considerably more energetic than that with single atoms or small molecules irradiated at the same intensity.

A numerical model, which treats the cluster as a spherical nanoplasma, is used to analyse the explosion of a single cluster. The model suggests that the super-heating of the clusters arises from a sharp increase in the laser-driven collisional heating. This increase occurs when the electron density in the expanding cluster drops to three times the critical electron density, at which point the electric field inside the cluster plasma is resonantly enhanced compared to the external field. We have investigated the possibility of using two pulses with different frequencies to excite the resonance in the heating twice during the expansion of the cluster, thereby enhancing the electron heating. The numerical model has been adapted to simulate the irradiation of a cluster with a sequence of laser pulses. The results of this new model support the idea that using two pulses of different frequencies will enhance the heating.

We have performed experimental investigations of the dynamics of clusters of a few thousand Xe atoms when irradiated by two laser pulses of different frequencies in sequence. The dependence of the explosion temperature on the delay between the two pulses and on their relative polarisations is examined. It is shown that using two pulses with the optimum delay between them can indeed enhance the explosion temperature. The experimental results show good agreement with the modelling.

Acknowledgements

First of all, I'd like to thank my supervisors, Jon Marangos and Henry Hutchinson, for taking me on as a PhD student. I have learnt to appreciate their very different styles of supervising. I'd like to express my gratitude to Jon for continually pestering me to finish this thesis, and thank Henry for leaving me in peace to get on with it.

I have enjoyed working with almost everyone in the Laser Consortium, even though the lack of air-conditioning and their baggy shorts means that I know them all far, far better than I really wanted to. I would especially like to thank my colleagues in the Ti:Sapphire lab, without whom I'd still be trying in vain to get the laser to mode-lock. In particular, John Tisch has made up for the lack of female company in the lab by being bitchy, broody and always noticing when I've had my hair cut. Mike Mason has shown me lots of inventive things to do with plastic spoons. Nick 'buy a new hard drive' Hay deserves thanks for at least waiting until I'd finished this before upgrading.

I'm grateful to Roland 'CPA by day, thrill-seeker by night' Smith for his continual (relentless) interest in my work and futile efforts to teach me about instrumentation while we're in the pub. I learnt a lot from working with Todd 'Sweet!' Ditmire, and I'm especially grateful to him for giving me a copy of his cluster model code. Todd is probably the most enthusiastic and emphatic person I've worked with and his tolerance for Belgian beer is awesome. I'd also like to say 'Oh, Hi!' to Yongliang Shao who gave me a lot of help in my first year.

I am still impressed by Peter Ruthven's ability to build a beautifully engineered bit of kit from a scribbled drawing and to stay awake in the Monday morning meetings – even if he does confuse me with a moose occasionally. Andy Gregory and Shahid Hanif also deserve thanks.

I've enjoyed working with Andy 'Er.. coffee, boyo?' Comley (although his inability to talk in his own voice rather than Roland's is getting slightly worrying), and I want to thank Chris Dorman, Kirstie and Marcel for always being at coffee. I should also thank the silverfish, in particular the motorcycle formation riding team, for letting me moan at them. Furthermore, working in tenuous association with Ed Gumbrell has been invariably educational, having substantially expanded my vocabulary, and in addition (to summarise the substantive points drawn throughout) taught me that, while an amusing concept may accumulate age it is (in a sense) immortal, in that the said concept can be repeated *ad infinitum* while still eliciting considerable amounts of mirth.

I owe a lot to my parents and my sister (and not only money) and I have appreciated their love and support over the past few years. Thanks also go to Paul and Ashley for their continual efforts to persuade me to give up science by just telling me their salaries. But probably my biggest debt of gratitude goes to Gill Rose, without whose inspirational teaching I'd happily be earning millions too.

Contents

Title page 1
Abstract 2
Acknowledgements 3
Contents 5
List of figures 9
List of tables 17

1 Introduction

1.1 High-intensity laser-matter interactions 18
1.1.1 Atoms 20
1.1.2 Molecules 21
1.1.3 Solids 22
1.2 Organisation of the manuscript 24

2 Theory of the laser-cluster interaction

2.1 Introduction 26
2.2 Models of the laser-cluster interaction 27
2.2.1 Coulomb explosion 27
2.2.2 Particle codes 27
2.2.3 Ionisation ignition 28
2.2.4 Inner shell excitation 29
2.2.5 Coherent electron motion 29
2.2.6 Discussion 30
2.3 Electron heating in laser-plasmas 31
2.3.1 Above-threshold ionisation 31
2.3.2 Stimulated Raman scattering 32
2.3.3 Inverse Bremsstrahlung 33
2.4 The nanoplasma model 35
2.4.1 Assumptions 35
2.4.2 Ionisation mechanisms 35
2.4.3 Heating mechanisms 36
2.4.4 Electron–ion collisions 37
2.4.5 Cluster expansion 38

2.4.6 Electron and ion temperatures 39
2.4.7 Running the model 40
2.4.8 Predictions of the nanoplasma model 41
2.5 Discussion and conclusions 46

3 High-intensity laser systems

3.1 Introduction 48
3.2 Ultrashort pulses 49
3.2.1 The optical Kerr effect 50
3.2.2 Self-focusing and optical breakdown in dielectrics 51
3.2.3 Kerr lens mode-locking 52
3.2.4 Group velocity dispersion 53
3.2.5 Self-phase modulation 54
3.3 Gain media for ultrashort pulse generation 55
3.4 Chirped pulse amplification 57
3.4.1 Limits on the recompressed pulse duration 60
3.4.1.1 Spectral clipping and narrowing 60
3.4.1.2 High-order phase terms 61
3.5 The Blackett Laboratory Laser Consortium Ti:Sapphire CPA laser system 62
3.5.1 The Oscillator 63
3.5.2 The stretcher 64
3.5.3 The regenerative amplifier 65
3.5.4 The single pulse isolator 67
3.5.5 The multi-pass power amplifiers 67
3.5.6 The compressor 69
3.5.7 Final output and focused intensity 70
3.6 Conclusions 73

4 Experimental apparatus and techniques

4.1 Cluster formation in gas-jets 74
4.1.1 Determination of cluster size 74
4.1.1.1 Hagena parameter 75
4.1.2 Rayleigh scattering 76
4.1.3 Experimental apparatus 78
4.1.4 Results 80
4.1.5 Cluster sizes 82

4.2 Experimental techniques and apparatus 84
4.2.1 Time-of flight spectrometer 84
4.2.2 Measurement of electron energies 86
4.2.3 Measurement of ion energies and charge states 87
4.2.4 Microchannel plate response 88
4.3 Conclusions 91

5 Clusters irradiated by a single high-intensity, femtosecond laser pulse

5.1 Introduction 92
5.1.1 Anomalous x-ray emission from clusters 93
5.1.2 Comparison of measurements with predictions of nanoplasma model 94
5.2 Electron energy spectra 95
5.2.1 Angular distribution of electrons 98
5.3 Ion energy spectra 100
5.3.1 Angular distribution of ions 101
5.3.2 Charge state distributions 103
5.3.3 Scaling with cluster size 106
5.3.4 Intensity dependence 108
5.3.5 Wavelength scaling 110
5.3.6 Dependence on cluster ion species 113
5.4 Discussion 117
5.5 Conclusions 122

6 The explosion of atomic clusters irradiated by a sequence of two high-intensity laser pulses

6.1 Introduction 123
6.2 Numerical modelling of the two-colour interaction 125
6.2.1 Adapting the model to simulate cluster interaction with two pulses of different frequencies 125
6.2.2 Numerical simulations of the explosion 126
6.2.2.1 Relative delay of the two pulses 128
6.2.2.2 Effect of the relative phase of the two laser pulses 130
6.3 Experiment 132
6.3.1 Method 132
6.3.1.1 The two-colour delay line 132

6.3.1.2 Spatial and temporal overlap of the two beams using N_2 breakdown 133
6.3.1.3 Finding T-zero by looking at ionisation rates in Xe^{3+} 134
6.3.2 Results 135
6.3.2.1 Varying the delay between the two pulses 135
6.3.2.2 Effect of the relative polarisations of the two pulses 138
6.4 Discussion 140
6.4.1 Cluster irradiation by two pulses of the same frequency 140
6.5 Conclusions 142

7 Conclusions

7.1 Summary 143
7.2 Further work and future directions 144
7.2.1 Cluster size distribution measurements 144
7.2.2 Self-similar expansions 145
7.2.3 Second peak in ion spectrum 145
7.2.4 Electron energy measurements 145
7.2.5 Molecular clusters 146
7.2.6 Highly stripped ions for particle accelerators 147
7.2.7 Thermonuclear fusion 147
7.3 Conclusions 148

References 149

List of figures

Figure 1.1. (a) Multiphoton ionisation. (b) Tunnel ionisation. (c) Over-the-barrier ionisation 20

Figure 1.2. Potential wells for a dielectric molecule in a strong laser field 21

Figure 2.1. Above-threshold ionisation 31

Figure 2.2. Heating rate per electron for a cluster irradiated by a 780 nm laser pulse at 1×10^{16} Wcm^{-2}. 38

Figure 2.3. Irradiation of a 5000-atom Xe cluster by a 200 fs, 780 nm laser pulse with a peak intensity of 10^{16} Wcm^{-2}. (a) The envelope of the vacuum electric field due to the laser pulse and the electric field in the cluster. (b) Ionisation rates due to thermal, tunnel and laser-driven collisional ionisation 41

Figure 2.4. (a) The ratio of the electron density in the cluster, n_e, to the critical electron density $n_{critical}$. (b) Electron temperature 42

Figure 2.5. (a) The charge build-up on the cluster (b) Escape energy. (c) Electron free-streaming rate 42

Figure 2.6. Hydrodynamic pressure from the electrons (black) and Coulomb pressure due to charge build-up on the cluster (green) 43

Figure 2.7. (a) Cluster radius, (b) expansion velocity and (c) acceleration 43

Figure 2.8. Calculated ion charge state distribution following the irradiation of a 5000-atom Xe cluster by a 200 fs, 780 nm laser pulse with a peak intensity of 10^{16} Wcm^{-2}. 44

Figure 2.9. Energy distribution of electrons which leave the cluster during the explosion 45

Figure 3.1. The Fourier transform of a series of modes, evenly spaced in frequency with a constant phase difference between them, is a train of pulses. 50

Figure 3.2. (a) Self-focusing due to the optical Kerr effect. (b) Filamentation of pulse in a Kerr medium 51

Figure 3.3. Kerr lens mode-locking. 52

Figure 3.4. A sequence of prisms which can be adjusted to give a negative value of group velocity dispersion 53

Figure 3.5. Chirped pulse. Self-phase modulation produces a frequency chirp proportional to dI/dt on the pulse 54
Figure 3.6. Chirped pulse amplification. An initially short pulse is stretched in time before being amplified and then recompressed. 57
Figure 3.7. Compressor grating configuration. 58
Figure 3.8. Pulse stretching in an optical fibre 58
Figure 3.9. Stretcher grating configuration. 59
Figure 3.10. Block diagram of the Imperial College Ti:Sapphire laser system 62
Figure 3.11. Kerr lens mode-locked Ti:sapphire oscillator 63
Figure 3.12. The stretcher. 64
Figure 3.13. Stretched pulse, measured with sampling head. 64
Figure 3.14. Ti:sapphire regenerative amplifier 65
Figure 3.15. Build-up of the IR pulse in the regenerative amplifier 65
Figure 3.16. The single pulse isolator. 66
Figure 3.17. Pre-pulse level with and without the single pulse isolator 67
Figure 3.18. Ti:sapphire double-pass pre-amplifier 68
Figure 3.19 Ti:sapphire multi-pass amplifier 68
Figure 3.20. Autocorrelations of the amplified pulse at the exit of the laser for the three major sets of laser configurations 69
Figure 3.21. Beam profile at the entrance to the compressor, obtained through measurement of the energy transmitted through a variable radius aperture. 69
Figure 3.22. Laser spectrum measured after the oscillator, where the FWHM is 9.3 nm, and at the output of the system where the spectrum has narrowed to 5.5 nm FWHM 70
Figure 3.23. Measured ion yield of Xe^{+}, Xe^{2+} and Xe^{3+} as a function of laser energy at 780 nm (a) and 390 nm (b). The laser intensity calculated from over-the-barrier appearance intensities is shown on the top axis. 71
Figure 3.24. Typical IR focal spot with f = 19.3 cm lens 71

Figure 4.1. Gas-jet used to produce clusters. 78

Figure 4.2. Experimental set-up to observe 90° scatter. 79

Figure 4.3. (a) Dependence of scatter signal on gas-jet backing pressure for xenon at 300 K, 250 K and 200 K. (b) Dependence of scatter signal on initial gas temperature for xenon at 1.4 bar, 2.8 bar and 4.1 bar. (c) Dependence of scatter signal on gas-jet backing pressure for argon, krypton and xenon at 200 K 80

Figure 4.4. Dependence of scatter signal (multiplied by T/p to account for the variation in the number of monomers) on Hagena parameter 81

Figure 4.5. Experimental configuration for measuring ion and electron energies 84

Figure 4.6. Timing and acquisition electronics 85

Figure 4.7. Sequence of trigger events required to ensure cluster beam is intercepted by laser pulse 86

Figure 4.8. (a)Time-of-flight spectrum from 4700-atom xenon clusters (backing pressure 5 bar) irradiated by a peak intensity of 2×10^{16} Wcm^{-2}. 87

Figure 4.9. Single shot of a time-of-flight trace used to compile data for pulse height analysis. 88

Figure 4.10. Pulse height distribution obtained from 2500 shots of 14000-atom Xe clusters irradiated at an intensity of 1.5×10^{16} Wcm^{-2}. The number of ion hits at each height is shown for each flight time, together with the mean pulse height. 89

Figure 4.11. Comparison of (a) the time-of-flight traces and (b) ion energy spectra obtained by analysing the data through pulse counting (red lines) and averaging (black lines). The mean ion energies calculated in each case were 8.2 keV from averaging and 7.7 keV from pulse counting 90

Figure 5.1. (a) Measured electron energy distribution from xenon clusters for a peak intensity of 1.3×10^{16} Wcm^{-2}. The gas-jet backing pressure was 4.5 bar, corresponding to an average cluster radius of 47 Å or 7000 atoms. (b) Calculated electron energy spectrum from a cluster of 7000 Xe atoms irradiated by a 170 fs, 780 nm pulse with a peak intensity of 1.3×10^{16} Wcm^{-2}. 95

Figure 5.2. Measured yield of hot electrons as a function of xenon backing pressure. 96

Figure 5.3. (a) Angular distribution of 'hot electrons' with energies ranging from 2 to 3 keV. (b) Angular distribution of 'warm electrons' with energies ranging from 0.3 to 1 keV 98

Figure 5.4. Time-of-flight spectrum from 9000-atom xenon clusters (backing pressure 5 bar) irradiated by a peak intensity of 2×10^{16} Wcm^{-2} 100

Figure 5.5. (a) Ion energy spectrum from clusters of 9000 Xe atoms irradiated by a peak intensity of 1.5×10^{16} Wcm^{-2}, derived from the time-of-flight trace shown in figure 5.4. The mean ion energy is 91 keV. (b) Solid line: Maxwellian with a mean energy of 91 keV. Dotted line: Uniform isotropic expansion with a mean energy of 91 keV 101

Figure 5.6. (a)Time-of-flight traces of ions produced by the irradiation of clusters of 5300 Xe atoms (backing pressure 4 bar) with a peak intensity of 1.3×10^{16} Wcm^{-2}. Each curve (offset for clarity) has been taken with a different angle between the laser polarisation and the detection axis. (b) Mean ion energies calculated from the time-of-flight traces in (a) 102

Figure 5.7. Ion TOF traces with 38 cm flight tube of 9000-atom Xe clusters irradiated with a peak intensity of 1.3×10^{16} Wcm^{-2} at retarding voltages of 0, 800, 1600 and 3300 V. 103

Figure 5.8. Measured charge state distribution of clusters of 9000 Xe atoms (backing pressure 5 bar) and 3100 Kr atoms (6 bar) irradiated with a peak intensity of 1.3×10^{16} Wcm^{-2} for ion kinetic energies of 1, 2, 5, 10, 20 and 30 keV. 103

Figure 5.9. Mean charge state as a function of ion kinetic energy for Xe (solid circles) and Kr (open circles), calculated from the ion charge state distributions in figure 5.8 104

Figure 5.10. Calculated charge state distributions from clusters of 10^4 Xe, Kr or Ar atoms irradiated by a 170 fs, 780 nm pulse with a peak intensity of 1.3×10^{16} Wcm^{-2}. 105

Figure 5.11. Calculated maximum ion energy as a function of mean charge state obtained in the explosion for eight different atomic species. The cluster size was 6000 atoms and the laser pulse was 780 nm. 260 fs, 2×10^{16} Wcm^{-2}. 105

Figure 5.12. Ion time-of-flight spectra from clusters of 200, 400, 1000, 5300, 14000, 28000, 47000 and 74000 xenon atoms (backing pressures 1, 1.3, 2, 4,

6, 8, 10 and 12 bar respectively) irradiated by a 230 fs pulse with a peak intensity of 2.8×10^{15} Wcm^{-2}. 106

Figure 5.13. Ion energy spectra obtained from the time-of-flight spectra in figure 5.12 from clusters of 1000, 5300, 28000 and 74000 xenon atoms (backing pressure 2, 4, 8 and 12 bar respectively) irradiated by a peak intensity of 2.8×10^{15} Wcm^{-2}. 107

Figure 5.14. (a) Maximum ion energies obtained from the time-of-flight spectra in figure 5.12. The peak laser intensity was 2.8×10^{15} Wcm^{-2}. (b) Calculated ion energies as a function of cluster size for 230 fs, 780 nm pulses with peak intensities of 1×10^{15} Wcm^{-2} (dashed line) and 3×10^{15} Wcm^{-2} (solid line) 107

Figure 5.15. (a) Maximum and (b) mean ion energies measured as a function of laser intensity from 3×10^{14} Wcm^{-2} to 2×10^{15} Wcm^{-2}. There were 5300 Xe atoms per cluster. The 780 nm laser pulse was 230 fs long 109

Figure 5.16. Calculated intensity dependence of the mean ion energy for Xe clusters of 5300 (filled circles) and 14000 atoms (open circles). The laser pulse was 230 fs long and had a wavelength of 780 nm 109

Figure 5.17. Ion time-of-flight spectra from clusters of 80, 200, 400, 1000, 5300, 14000, 28000, 47000 and 74000 xenon atoms (backing pressures 0.7, 1, 1.3, 2, 4, 6, 8, 10 and 12 bar respectively) irradiated by a 390 nm pulse with a peak intensity of 5.0×10^{15} Wcm^{-2}. 110

Figure 5.18. (a) Maximum ion energies measured in the interaction of xenon clusters with 780 nm (red circles) and 390 nm (blue circles) radiation. The peak intensity of the 390 nm pulses was 5.0×10^{15} Wcm^{-2} and that of the 780 nm pulses was 2.8×10^{15} Wcm^{-2}. (b) Calculated mean ion energy as a function of cluster size for Xe atoms irradiated by a 230 fs, 780 nm pulse (red) or a 160 fs, 390 nm pulse with a peak intensity of 3×10^{15} Wcm^{-2} (blue). 111

Figure 5.19. Measured intensity dependence of the maximum (a) and mean (b) ion energies from the irradiation of 5300-atom Xe clusters with 390 nm (blue circles) and 780 nm (red circles) laser pulses 112

Figure 5.20. Calculated intensity dependence of the mean ion energy from clusters of 5300 Xe atoms irradiated by a 230 fs, 780 nm pulse (red) or a 160 fs, 390 nm pulse (blue) with a peak intensity between 10^{13} Wcm^{-2} and 10^{17} Wcm^{-2}. 113

Figure 5.21. Ion energy spectra from Xe, Kr, Ar and Ne clusters. The gas-jet backing pressures and temperatures were 2 bar Xe at 300K (~1000 atoms), 4 bar Kr at 300 K (~1200 atoms) , 8 bar Ar at 300 K (~1500 atoms) and 12 bar Ne at 80 K (~ 29000 atoms). The laser intensity in each case was 1.3×10^{16} Wcm^{-2} for Xe, Kr and Ar, and 1.8×10^{16} Wcm^{-2} for Ne 114

Figure 5.22. (a) Measured maximum ion energies from Xe (red), Kr (green), Ar (blue) and Ne (black) clusters with a variety of cluster sizes. (b) Calculated mean ion energy from clusters of Xe, Kr, and Ar and Ne atoms irradiated by a 170 fs, 780 nm pulse with a peak intensity of 1.3×10^{16} Wcm^{-2} 114

Figure 5.23. (a) Maximum and (b) mean ion energies measured as a function of laser intensity from 3×10^{14} Wcm^{-2} to 2×10^{15} Wcm^{-2} for 5300-atom Xe clusters and 6200-atom Kr clusters. The 780 nm laser pulse was 230 fs long. 115

Figure 5.24. Calculated intensity dependence of the mean ion energy from clusters of 5300 Xe atoms (red) or 6200 Kr atoms (green) irradiated by a 230 fs, 780 nm pulse with a peak intensity between 10^{13} Wcm^{-2} and 10^{17} Wcm^{-2}. 116

Figure 6.1. Numerical modelling of the interaction of a cluster of 14000 Xe atoms irradiated by a 185 fs, 390 nm pulse with a peak intensity of 2.5×10^{14} Wcm^{-2} and a 260 fs, 780 nm pulse with a peak intensity of 4.0×10^{15} Wcm^{-2}. The centres of the two pulses are coincident at $t = 0$ fs. (a) The envelope of the electric fields of the two individual pulses. (b) Electric field inside the cluster. (c) Electron density. (d) Electron temperature in the cluster 126

Figure 6.2. Numerical modelling of a cluster irradiated with two laser pulses with intensities and delays as in figure 6.1. (a) Hydrodynamic (solid line) and Coulomb (dotted line) pressure in the cluster. (b) Acceleration of the cluster radius 127

Figure 6.3. Numerical modelling of a cluster irradiated with two laser pulses with intensities and delays as in figure 6.1. The centres of the two pulses are coincident at t = 0 fs. (a) Escape energy. (b) Electron free-streaming rate. 127

Figure 6.4. Calculated electron energy spectrum from a cluster of 14000 Xe atoms irradiated by a 185 fs, 390 nm pulse with a peak intensity of 2.5×10^{14} Wcm^{-2} and a 260 fs, 780 nm pulse with a peak intensity of 4×10^{15} Wcm^{-2} 128

Figure 6.5. Calculated electron energy spectra from clusters of 14000 Xe atoms irradiated by a 260 fs, 780 nm pulse at 4×10^{15} Wcm^{-2} and a 185 fs, 390 nm pulse with a peak intensity of 2.5×10^{15} Wcm^{-2}. (a) shows the spectrum due to the 390 nm pulse alone, while (i) shows that from the 780 nm pulse alone. (b) to (h) show the change in electron energy spectrum as the delay between the two pulses is varied from –1 ps to +1 ps. 129

Figure 6.6. Calculated maximum ion energies from the irradiation of 14000 atom Xe clusters with one 780 nm, 260 fs, 4×10^{15} Wcm^{-2} pulse and one 390 nm, 185 fs, 2.5×10^{15} Wcm^{-2} pulse as the delay between the two pulses is varied 129

Figure 6.7. Calculated maximum ion energies from clusters of 14000 Xe atoms irradiated by a 260 fs, 780 nm pulse or a 185 fs, 390 nm pulse as the peak laser intensity is varied from 1×10^{15} Wcm^{-2} to 2.5×10^{16} Wcm^{-2}. 130

Figure 6.8. Experimental set-up used to vary the relative delays, intensities and polarisations of the fundamental and second harmonic pulses 132

Figure 6.9. Using breakdown in N_2 to obtain spatial and temporal overlap of the red and blue foci. (a) Undistorted blue beam at the exit of the TOF chamber with the IR blocked. (b) IR beam at the exit of the TOF chamber showing distortion caused by breakdown in N2. (c) Blue beam at the exit of the TOF chamber after it has passed through the plasma created by the IR focus. 133

Figure 6.10. Measured ion yields of (a) Xe^{2+} and (b) Xe^{3+} as the delay between the blue and IR pulses is varied 134

Figure 6.11. Measured ion TOF spectra from the irradiation of 14000-atom Xe clusters with a 780 nm and/or 390 nm laser pulse. (a) Blue pulse only. (b) Blue precedes IR by 600 fs. (c) Blue precedes IR by 200 fs. (d) Blue pulse 600 fs after IR. (e) IR pulse only 135

Figure 6.12. (a) Mean and (b) maximum ion energies measured from the irradiation of 14000 atom Xe clusters (6 bar Xe) with one 780 nm, 6×10^{14} Wcm^{-2} pulse (1.3 mJ) and one 390 nm, 2.5×10^{15} Wcm^{-2} pulse (1.9 mJ) as the delay between the two pulses is varied. (c) Calculated ion energies. 14000 Xe atoms irradiated by 4×10^{15} Wcm^{-2}, 780 nm, 260 fs and 2.5×10^{15} Wcm^{-2}, 390 nm, 185 fs. 136

Figure 6.13. (a) Mean and (b) maximum ion energies measured from the irradiation of 14000 atom Xe clusters (6 bar Xe) with one 780 nm, 1.1 mJ pulse (~6×10^{14} Wcm^{-2}) and one 390 nm, 1.1 mJ pulse (~2.5×10^{15} Wcm^{-2}) as the delay between the two pulses is varied. (c) Calculated max ion energies from a 14000-atom Xe cluster irradiated by 2×10^{15} Wcm^{-2}, 780 nm, 260 fs and 2×10^{15} Wcm^{-2}, 390 nm, 185 fs. 137

Figure 6.14. Measured mean ion energies from the irradiation of 14000 atom Xe clusters with one 780 nm, 0.5×10^{15} Wcm^{-2} pulse and one 390 nm, 1.3×10^{15} Wcm^{-2} pulse as the delay between the two pulses is varied. Vertical polarisation means electric field is perpendicular to detection axis; with horizontal polarisation the electric field is parallel to the detection axis (a) Black circles: Blue and IR both vertically polarised. Green circles: Blue and IR both horizontally polarised. Red squares: IR horizontal, blue vertical. Blue squares: IR vertical, blue horizontal. (b) Circles: Blue and IR are polarised parallel to each other (average of green and black circles in (a)). Squares: Blue and IR are polarised perpendicular to each other (average of red and blue squares in (a)) 138

Figure 6.15. Intensity envelope from two pulses of the same frequency, one with ~ half the intensity of the other and relative phases of $\phi = 0$ (solid line) or $\phi = \pi$ (dashed line). 141

List of tables

Table 3.1. Laser media for ultrashort pulse generation 55

Table 3.2. Laser parameters in the three major sets of laser configurations 72

Table 4.1. Estimated cluster sizes for Xe, Kr, and Ar over the range of gas-jet backing pressures and temperatures investigated, calculated from equations 4.1 and 4. 11. 83

Introduction

1.1 High-intensity laser-matter interactions

Progress in laser technology means that it is now possible to reach laser intensities where the laser electric field is stronger than the electric field experienced by an electron in an atom. A new regime of laser-matter interactions can now be studied [Perry 1994]. Peak powers of a terawatt (10^{12} W) can be accessed, but the laser pulses amplified are typically shorter than a picosecond, meaning that only a very modest amount of energy (less than a joule) is contained in each laser pulse. Very short pulses also means that the system being irradiated can survive to the peak of the laser pulse and so be exposed to the highest intensities.

The intensities routinely accessible with university-scale lasers increased dramatically with the first demonstration of 'chirped pulse amplification' (CPA) in 1985 [Strickland 1985]. Prior to the advent of CPA, the intensities accessible were limited by the high peak powers in the short pulses being amplified which caused damage to the laser. CPA avoids this problem by stretching the pulse in time before amplifying it, and then recompressing the pulse down to its original length. The CPA laser used to carry out the experiments described in this thesis has a pulse length of ~200 femtoseconds and a peak focused intensity of ~10^{16} Wcm^{-2}.

The interaction of intense and ultrashort laser pulses with single atoms [Agostini 1988, Burnett 1993, Protopapas 1997], small molecules [Sheehy 1996, Codling 1994] and bulk solids [Gibbon 1996] has been extensively studied. There is a dramatic difference between the irradiation of a monatomic gas, which results in a cold (few 10s of eV) plasma [Glover 1994], and a bulk solid which is ionised to produce a hot (~ 1 keV) plasma [Caruso 1969]. This thesis describes the interaction of intense laser pulses with van der Waals bonded clusters of 10^2 – 10^5 noble gas atoms. Clusters are an intermediate state between

single atoms or molecules and bulk solids [Castleman 1988], as they have the same local density as a solid, but can have the same average density as a gas. Clusters can be created as a gas cools while expanding from a high-pressure gas-jet into vacuum. The size of the clusters produced depends on the species of gas, its initial pressure and temperature, and the geometry of the gas-jet nozzle. The radius of the clusters used in these experiments was typically a few tens of angstroms, small compared to the laser wavelength of 780 nm.

The interaction of lasers with matter at high intensities is very different to the standard 'weak field' case which can be studied using perturbation theory to describe the laser as a small perturbation on the atomic system.

The laser pulses used in the experiments described in this thesis had peak focused intensities of 10^{15} - 10^{16} Wcm^{-2}. The laser intensity I is related to the electric field strength E by

$$I = \frac{1}{2} c \varepsilon_0 E^2$$
$$I[\mathrm{Wcm}^{-2}] = 1.33 \times 10^{-3} E[\mathrm{Vcm}^{-1}]^2 \qquad (1.1)$$

where c is the speed of light and ε_0 the permittivity of free space.

At an intensity of 3.5×10^{16} Wcm^{-2} (one atomic unit of intensity), the oscillating laser electric field is as strong as the Coulomb field acting on a ground-state electron in a hydrogen atom. Perturbation theory is obviously inadequate to describe the interaction at these intensities.

At high intensities, the quiver or ponderomotive energy (U_P) of an electron oscillating in a laser field can be quite substantial. Averaged over a cycle, the ponderomotive energy is

$$U_P = \frac{e^2 E^2}{4 m_e \omega^2}$$
$$U_P[\mathrm{eV}] = 9.33 \times 10^{-14} I[\mathrm{Wcm}^{-2}] \lambda[\mu\mathrm{m}]^2 \qquad (1.2)$$

where e and m_e are the electron charge and mass, and E, ω and λ the laser electric field, frequency and wavelength. For a 780 nm field at 10^{16} Wcm^{-2}, the ponderomotive energy is ~ 570 eV. In comparison, the energy of a single 780 nm photon is 1.5 eV.

The ponderomotive energy is not transferred to the electron during the laser pulse if no other force acts on the electron. The electron energy rises and then falls as the pulse passes. Energy can only be transferred to the electron if something happens to break the adiabacity. For example, the electron could collide with an ion and change direction (collisional absorption or inverse bremsstrahlung) or absorb a photon in the presence of an ion (above threshold ionisation).

In a experiments with long laser pulses (~ picoseconds), an electron can travel out of the laser focus before there are significant changes in the electric field amplitude. During its passage its total energy is conserved, so as it passes to regions of lower light intensity its ponderomotive energy is converted to directed kinetic energy. With pulse durations below ~ 500 fs, the pulse-length is short compared to the time it takes an electron to escape the ionisation region, and there is insufficient time for the electron to accelerate before the pulse leaves. The electron energy spectrum then records the actual electron energies and angular distributions at the moment of ionisation [Freeman 1987].

1.1.1Atoms

Photo-ionisation of atoms by photons with energies smaller than the ionisation potential can occur at high laser intensities. To ionise a noble gas with visible or near IR photons, the atom must absorb many photons. For example, eight 780 nm photons are required to singly ionise xenon and a laser intensity of ~ 10^{13} Wcm^{-2} is needed. This effect is known as multiphoton ionisation (MPI). It can be described as the simultaneous absorption of N photons with an ionisation rate

$$R_N = \sigma_N I^N \tag{1.3}$$

where σ_N is the cross-section for N-photon absorption and I is the laser intensity.

The multiphoton picture applies to the low intensity, short wavelength regime where the amount of ionisation in an optical cycle is small (fig 1.1a). Time-averaged quantities, such as the energy levels of the atom and the photon energy can be used to describe the process.

As the intensity or wavelength increase, we reach a regime where there is a significant amount of ionisation in an optical cycle. The laser field distorts the atomic potential over each cycle of light and electrons tunnel through the potential barrier (fig 1.1b). This is the tunnelling regime and represents the quasiclassical limit where it is more useful to think in terms of electric fields rather than photons. The ionisation rate is at its highest when the electric field is largest and the barrier at its lowest and so is phase dependent. The

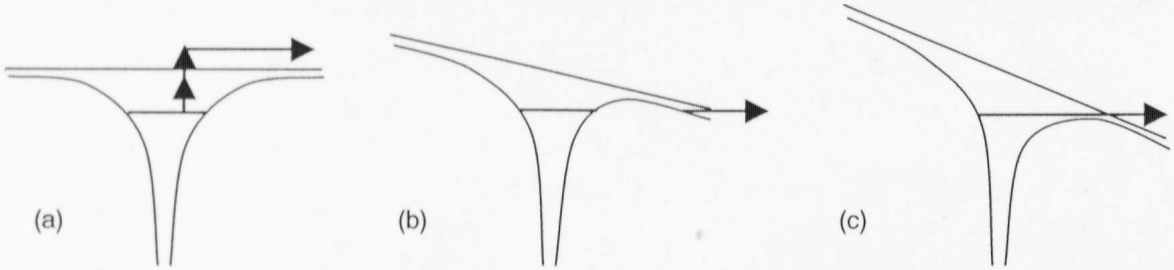


Figure 1.1. (a) Multiphoton ionisation. (b) Tunnel ionisation. The atomic potential is distorted in the laser field and the laser can tunnel through the potential barrier. (c) Over-the-barrier ionisation. At even higher laser intensities the laser field distorts the atomic potential so much that the electron can pass over the potential barrier.

probability of tunnelling remains constant as the frequency changes, because the tunnelling time is determined by the size of the potential barrier. The ionisation rate can be calculated from the 'ADK' (Ammosov, Delone and Krainov) formula [Ammosov 1986].

There is also a third regime - over the barrier field ionisation - where the atomic potential is so distorted in the laser electric field that the electron can simply pass over the potential barrier (fig 1.1c). The onset of ionisation can be approximated as the intensity at which the sum of the Coulomb and ponderomotive potentials cause the electron to be unbound [Augst 1989]. This intensity is given by

$$I_{OTB} = \frac{cI_P^4}{128\pi e^6 Z^2}$$
$$I_{OTB}[\mathrm{Wcm^{-2}}] = 4.00 \times 10^9 \frac{I_P[\mathrm{eV}]^4}{Z^2} \tag{1.4}$$

Here, I_P is the ionisation potential and Z is the charge on the ion (after ionisation)

Although there is no definite boundary between these three cases, it is possible to determine whether ionisation is taking place in the tunnelling or multiphoton regime by evaluating the Keldysh parameter [Keldysh 1965]. This is a dimensionless figure of merit defined as

$$\gamma = \left(\frac{I_P}{2U_P}\right)^{1/2}. \tag{1.5}$$

If $\gamma << 1$, ionisation is dominated by tunnelling, and if $\gamma >> 1$ it is dominated by multiphoton ionisation. For hydrogen in a 780nm field, $\gamma = 1$ at an intensity of $\sim 1.2 \times 10^{14}$ Wcm^{-2}, two orders of magnitude below the intensity at which the laser electric field is equal to the electric field experienced by the electron in a hydrogen atom.

1.1.2 Molecules

Many of the phenomena seen in single atoms in laser fields have close parallels with those observed in small molecules. As with atomic physics, molecular dynamics can be divided into strong field and weak field regimes. In the weak-field limit, molecules can ionise through multiphoton ionisation, while in intense laser fields the field ionisation model can be applied.

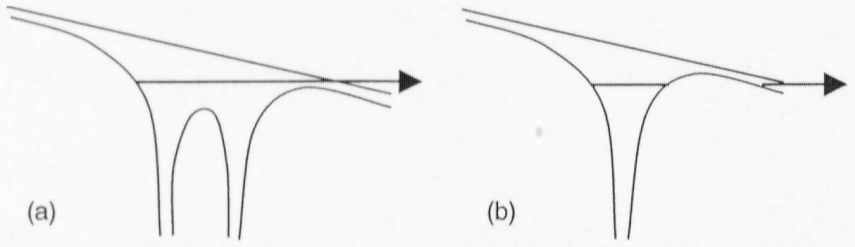


Figure 1.2. Potential wells for a dielectric molecule in a strong laser field. (a) Electric field parallel to the molecular axis. (b) Electric field perpendicular to the molecular axis.

Figure 1.2 shows the potential wells for a diatomic molecule with the electric field oriented parallel to (1.2a) and perpendicular to (1.2b) the molecular axis. There is a greater tunnelling probability when the laser electric field is along the molecular axis, as the electric field acts over a larger distance.

After the molecule is ionised, the ions in the molecule experience Coulomb repulsion. The molecule undergoes a Coulomb explosion leading to fragments with energies given by

$$E_{\text{Coulomb}} = \frac{q_1 q_2}{4\pi\varepsilon_0 r}$$
$$E_{\text{Coulomb}}[\text{eV}] = \frac{14.4 q_1 q_2}{r[\text{Å}]} \tag{1.6}$$

where q_1, q_2 are the charges on the ions and r is the internuclear separation at ionisation.

Typical measured ion energies would be, for example, 55 eV for the O^{3+} ions from CO_2 if the carbon was also triply charged [Cornaggia 1994]. The measured ion energies are consistently lower than the Coulomb repulsion energies of the ions at the equilibrium internuclear separation – approximately 50% of the calculated energies for CO_2 [Cornaggia 1994, Frasinski 1994]. These consistently low measured Coulomb explosion energies can be explained by tunnel ionisation at an optimum internuclear separation which is larger than the equilibrium separation [Codling 1989].

1.1.3 Solids

The leading edge of a high-intensity laser pulse produces free electrons at or near the surface of a solid through multiphoton processes. These electrons absorb energy and are rapidly heated (electron heating mechanisms are discussed further in Chapter 2). They then ionise the much cooler atoms, creating a high-temperature plasma at the surface of the solid.

The dispersion relation for electromagnetic waves with frequency ω and wavenumber k in a plasma is

$$\omega^2 = \omega_p^2 + k^2 c^2 , \tag{1.7}$$

where ω_p is the plasma frequency. This is the frequency associated with the charge density fluctuations caused by the motion of free electrons in a plasma (the ions are treated as a fixed, uniform, neutralising background) and is given by

$$\omega_p = \left(\frac{4\pi e^2 n_e}{m_e} \right)^{1/2}$$
$$\omega_p[\text{s}^{-1}] = 5.64 \times 10^4 \, n_e[\text{cm}^{-3}]^{1/2} \tag{1.8}$$

Here, n_e is the electron density and e and m are the charge and mass of an electron.

The minimum frequency of propagation of a light wave in a plasma is ω_p, as the wavevector k becomes imaginary for $\omega < \omega_p$. Therefore, the condition $\omega_p = \omega$ defines the maximum plasma density to which the light can penetrate (for regimes where relativistic or gross ponderomotive effects are unimportant). This is the 'critical density', $n_{critical}$, which is

$$n_{critical} = \frac{\pi c^2 m_e}{e^2 \lambda^2}$$
$$n_{critical}[\mathrm{cm}^{-3}] = \frac{1.1 \times 10^{21}}{\lambda[\mu\mathrm{m}]^2} \quad (1.9)$$

For 780 nm radiation, $n_{critical}$ is 1.8×10^{21} cm^{-3}, about 1/30th the number density of ions in a solid. Inside the target, beyond the skin-depth (c/ω_p), the free electrons partially screen the laser field by a factor $\approx \omega/\omega_p$ [Panofsky 1978]. This effect reduces the importance of any high-field or non-linear absorption mechanisms.

Laser produced plasmas have been investigated since the 1960s for applications such as inertial confinement fusion [Nuckolls 1972, Meyer-ter-Vehn 1997], x-ray lasers [Eder 1994, Matthews 1995] and sources of (incoherent) x-rays [Murnane 1991]. Plasmas created from short laser pulses are fundamentally different from those created with long (nanosecond) pulses [Caruso 1969]. If the laser pulse is much longer than a few tens of picoseconds, the plasma undergoes substantial expansion into vacuum on a time-scale shorter than the pulse duration, creating a density gradient. Light is then absorbed by collisional heating of electrons up to critical density and through resonant processes at or near the critical density. Laser light can be absorbed efficiently, resulting in low reflectivity (< 20% for a Si target [Murnane 1991]).

If the pulse creating the laser is shorter than ~ 1 ps, the density gradient will be much steeper and can be shorter than the skin-depth. This means that laser energy can be deposited at much higher densities than in nanosecond interactions [Gibbon 1996]. However, the absorption is low and ~ 90% of the incident light can be reflected [Murnane 1993].

The energy deposited into a solid target can diffuse rapidly: the high thermal gradients lead to rapid conduction into the bulk solid (by thermal and hot electrons and radiation transport), the high pressure gradients mean that the plasma can expand rapidly into vacuum, and the non-equilibrium conditions ensure that electrons cool by inelastic collisions with atoms and ions.

Laser interactions with clusters differ in several fundamental respects from solid-target interactions. The small size of the clusters (they are much smaller than both the skin-depth and the laser wavelength) means that all of the atoms in a cluster experience

essentially the same laser field. As the average density of the clusters is low, there is no bulk solid to cool the plasma.

1.2 Organisation of the manuscript

This thesis describes the explosion of atomic clusters irradiated by high-intensity, femtosecond laser pulses. We have measured the energies of ions and electrons ejected in the cluster explosion and the dependence of the ion energies on laser intensity and wavelength, cluster size and cluster medium has been studied. The interaction with clusters is considerably more energetic than that with single atoms or small molecules irradiated at the same intensity. Ion energies of up to 1 MeV and electron energies of up to 2.5 keV were measured.

A numerical model which treats the cluster as a spherical nanoplasma is used to analyse the explosion of a single cluster. The model suggests that the super-heating of the clusters arises from a sharp increase in the laser-driven collisional heating. This increase occurs when the electron density in the expanding cluster drops to three times the critical electron density, at which point the electric field inside the cluster plasma is resonantly enhanced compared to the external field. The numerical model shows good qualitative agreement with the experimental results and is able to predict the shape of the electron energy spectrum and the trends in the mean ion energies.

To more fully test the nanoplasma model, we have investigated the possibility of using two pulses with different frequencies to excite the resonance in the heating twice during the expansion of the cluster, thereby enhancing the electron heating. The numerical model has been adapted to simulate the irradiation of a cluster with a sequence of laser pulses. The results of this new model support the idea that using two pulses of different frequencies will enhance the heating.

We have performed experimental investigations of the dynamics of clusters of a few thousand Xe atoms when irradiated by two laser pulses of different frequencies in sequence. The dependence of the explosion temperature on the delay between the two pulses and on their relative polarisations is examined. It is shown that using two pulses with the optimum delay between them can indeed enhance the explosion temperature. The experimental results show good agreement with the modelling.

Chapter Two of this thesis considers the theory relevant to the laser-cluster interaction. Electron-heating mechanisms in gas and solid targets are discussed and various theoretical models of the cluster explosion mechanism are reviewed. The nanoplasma model is detailed and numerical results are presented.

The Blackett Laboratory Laser Consortium Ti:Sapphire laser used was to carry out all the experiments described in this thesis. A detailed description and characterisation of the

laser, together with a discussion of the generation and amplification of ultrashort laser pulses, forms Chapter Three.

Chapter Four describes the experimental apparatus used. Our clusters were formed in the expansion of gas from a pulsed gas-jet into vacuum and their sizes have been estimated from scattering measurements. The measurement of the ion and electron energies in a time-of-flight spectrometer is detailed.

Chapter Five presents measurements of the ion and electron energies from the explosion of clusters irradiated by a single laser pulse. The scaling of the ion energies with cluster size and cluster ion species, laser wavelength and laser intensity have also been measured and these results are compared against the predictions of the nanoplasma model.

Chapter Six describes the 'two-colour' experiment. The clusters were irradiated with two laser pulses of different frequencies and the ion energies measured as the delay between the two pulses was varied. The nanoplasma model was adapted to describe this situation and the results are in good agreement with the model.

Chapter Seven concludes the thesis and presents some suggestions for future experiments.

Theory of the laser-cluster interaction

2.1 Introduction

In this chapter, various theoretical models that have been used to describe the laser-cluster interaction are discussed. Ditmire *et al* [1996] have developed a model – referred to as the 'nanoplasma' model throughout this thesis – which treats the cluster as a small spherical plasma. The nanoplasma model and its predictions are discussed in detail, as the results of this code are tested against the experimental measurements described in Chapters 5 and 6 of this thesis.

The version of the nanoplasma model described here and used for all the numerical calculations presented in this thesis differs slightly from that presented in [Ditmire 1996] as I have adapted it to allow the easy addition of a second laser pulse with a different frequency (described in Chapter 6). In particular, this version uses instantaneous rather than cycle averaged ionisation rates. The code has also been largely re-written in *C++* rather than *C* to take advantage of *C++* features such as classes and creation of arrays during run-time. This has enabled us to easily model several different atomic species. The user-interface has also been re-written to allow the code to run through large sets of initial conditions automatically.

As we treat the cluster as a plasma, the relevant electron heating mechanisms in plasmas, including above-threshold ionisation, stimulated Raman scattering and inverse bremsstrahlung, are also discussed.

2.2 Models of the laser-cluster interaction

2.2.1 Coulomb explosion

Many studies of the dissociation of small clusters (typically 2 – 60 atoms or molecules) have interpreted the resulting ion kinetic energies in terms of Coulomb explosion of the cluster [Last 1997, Purnell 1994, Rexer 1997]. In a Coulomb explosion, the electrons are assumed to leave the vicinity of the ion immediately after explosion, so they have no effect on the subsequent ion dynamics. As with small molecules, Coulomb explosions of clusters can be divided into two classes: 'vertical' where ionisation occurs at the neutral geometry of the cluster, and 'non-vertical' where ionisation takes place during the expansion when the interatomic distances are larger than in the neutral cluster. Non-vertical ionisation leads to lower kinetic energies of the fragment ions.

The vertical Coulomb explosion of small Xe clusters has been numerically modelled by Last *et al* [1997].The final average velocity of the Xe ions was found to be equal to a constant times the charge on the ion for a given cluster size, with the constant increasing as the cluster size increased from 2 to 55 atoms. However, measurements of the ion energies from $HIAr_n$ clusters [Purnell 1994] were found to be in poor agreement with the theoretical predictions for a vertical Coulomb explosion [Last 1997].

The case of non-vertical Coulomb explosion has also been examined [Last 1998] by calculating the shape of the potential wells in the expanding cluster and performing classical electron trajectory calculations. However, in these simulations the authors found that most of the electrons were, in fact, ionised when the internuclear distance was close to equilibrium. Coulomb repulsion alone may be inadequate to explain the observed ion energies from even fairly small exploding clusters and the effect of the electrons should be considered.

2.2.2 Particle codes

Classical particle dynamics simulations of small (<55 atoms) exploding clusters have been performed in which both ion and electron trajectories are tracked [Ditmire 1998c]. This is in contrast to Coulomb explosion models which ignore the electrons after ionisation. The model assumes that electrons are created through both tunnel and collisional ionisation in the cluster. For large clusters (55 atoms), a large fraction of ionised electrons were found to remain in the cluster after ionisation due to the strong positive charge on the cluster. This means that collisional ionisation by laser-driven electrons is important. For example, the model predicts that all the Ar atoms in a 55-atom cluster will be stripped to 8^+ - 10^+ at 10^{15} Wcm^{-2}, whereas 10^{18} Wcm^{-2} would be required to reach Ar^{9+} through over-the barrier ionisation [Augst 1989] (equation 1.4).

These results were compared with those obtained when the model was run ignoring the electric fields of the electrons and electron collisional ionisation and was found to be in fairly good agreement for small clusters (6 atoms) but in poor agreement for large (55-atom) clusters. This indicates that the Coulomb explosion model is only satisfactory for very small clusters, where the electrons leave the cluster volume fast.

A model of a cluster as a linear chain of 2 to 12 atoms has been developed by Brewczyk *et al* [1998]. The model treats the atoms classically, and the electrons through an electron density function. The cluster explosion was found to be sequential, with the ions at the end of the cluster leaving first and having the most kinetic energy. (For a spherical cluster this would correspond to shells of ions being thrown off.) This leads to a wide spectrum of ion kinetic energies for a given charge state. The electron heating was found to be higher when the ion density was higher, consistent with heating through inverse bremsstrahlung, and more effective in larger clusters. The heating occurs stepwise in time as the electron wave-packet is driven from one end of the linear cluster to the other.

These results have been compared to a Coulomb explosion model, in which electrons are suddenly removed from each atom in the chain. The Coulomb explosion model leads to lower final ion energies for chains of six or more ions. This again indicates that the Coulomb explosion model is only valid for extremely small clusters, and that the effect of the electrons must be considered.

2.2.3 Ionisation ignition

Cluster explosions in an intense laser field have also been theoretically modelled with classical particle dynamics simulations by Rose-Petruck *et al* [1997]. 25- and 55-atom Ne clusters and 25-atom Ar clusters irradiated by an 800 nm, 15 fs pulse at intensities of 5×10^{15} Wcm^{-2} to 5×10^{17} Wcm^{-2} were modelled. At the start of the laser pulse, some electrons are ionised through over-the-barrier ionisation. These ionised electrons are then heated by inverse bremsstrahlung before the cluster starts to expand and are quickly removed by the laser field to produce an ultrafast pulse of hot electrons. The Coulomb potential binding an electron to an ion can be lowered by the Coulomb attraction of its neighbouring ions, thereby enhancing the rate of over-the-barrier ionisation. When the laser intensity exceeds the threshold for saturation of single ionisation, an avalanche of ionisation is initiated – this is known as 'ionisation ignition'. Ionisation ignition can result in a much higher charge state being attained in clusters than in individual atoms.

A two-dimensional model of a cluster as an array of potential wells has been constructed which also examines the effect of neighbouring ions on triggering an ionisation avalanche [Hu 1997ab]. The electron in an ion experiences the Coulomb field of its parent, the combined Coulomb field of all unscreened ions, shielding of the laser field by free

electrons and scattering during laser-driven oscillatory motion. Again, it was found that the ionisation probability of an atom increases as with the number of other ions surrounding it, leading to an ionisation avalanche.

2.2.4 Inner shell excitation

Studies of clusters in strong laser fields were triggered by the realisation that previous observations of x-ray emission from gas targets had been due to the presence of clusters [McPherson 1993]. Line emission from charge states higher than would be expected in the irradiation of atoms at the same intensity was observed, and a numerical model was developed to explain these observations [McPherson 1993, 1994b].

Enhanced ionisation can occur in a cluster compared to a gas with the same average density due to collisional ionisation by electrons that are accelerated by the laser field. If the electrons are energetic enough, they can remove inner-shell electrons from ions. This puts a cluster size-dependent lower limit on the intensity. Another lower limit is given by the need for the distance the electron oscillates over in the laser field to be comparable to or larger than the cluster size. For an inner shell hole to form, there must be some electrons remaining in the upper level: this puts an upper limit on the intensity which is set by the over-the-barrier ionisation threshold. In this way, allowed regions of cluster size and laser intensity where inner shell radiation can be emitted are defined.

This model has been examined by Brunner *et al* [1997, 1998] who have calculated the optimum ion density and pulse length for achieving population inversion. They predicted that gain in XUV radiation for short wavelength (< 350 nm) pulses of less than 100 fs would be possible [Brunner 1998]. The cluster expands rapidly after ionisation, so the gain decreases and the time duration for prompt and amplified x-ray emission would be less than 50 fs [Brunner 1997].

The probability of inner shell ionisation has also been calculated by analysing the electron trajectories during cluster explosion [Rose-Petruck 1997]. These results also indicate the possibility of inner-shell vacancies and x-ray line radiation from clusters which undergo ionisation ignition.

2.2.5 Coherent electron motion

The inner-shell excitation model has been modified by the addition of several new phenomena to enable the model to more closely fit the experimental results [Boyer 1994ab, Thompson 1994]. Based only on a factor of four difference between estimates of power radiated per atom based on experiment and the 'allowed zones' model described in the previous section, the Z field-ionised electrons are now allowed to move coherently in the laser field like a quasi-particle with charge Ze and mass Zm_e [Boyer 1994a]. Simultaneous

ejection of multiple (typically 2 or 3) electrons from cluster ions is considered, and the rate is found to be comparable to the rate of removal of a single electron. Multiple transits of driven electrons in the cluster are also considered.

2.2.6 Discussion

The results of the models of the described above emphasise the importance of the electrons in the laser-cluster interaction. The high density inside a cluster means that collisional ionisation can occur, which will enhance the ionisation rates compared to that of individual atoms in low-density targets. The results of the Coulomb explosion models and particle codes suggest that electrons can be retained in the cluster by the space-charge of the ions. The laser electric field in the cluster will then be modified due to the presence of the free electrons. These factors suggest that it may be appropriate to model the ionised cluster as a small laser-produced plasma.

2.3 Electron heating in laser-plasmas

The irradiation of clusters with intense laser pulses results in ions and electrons with extremely high energies, as the experimental results in Chapters 5 and 6 will show. In order to understand the origins of these high energies and compare them to the ion and electron energies from gaseous, molecular and solid targets, some electron heating mechanisms in laser-produced plasmas must be introduced. In the following sections, electron heating during ionisation ('above threshold ionisation'), through Coulomb collisions with ions ('inverse Bremsstrahlung'), and by driving plasma waves ('stimulated Raman scattering') are discussed.

2.3.1 Above-threshold ionisation

At very high light intensities where $I_P > U_P > h\nu$ and $\gamma > 1$ the electron energy spectrum following multiphoton ionisation of any atom changes from a single well-defined threshold peak (figure 2.1a) into multiple peaks separated from one another by the photon energy. These peaks are due to ionisation following the absorption of more than the minimum number of photons required for ionisation (figure 2.1b): this is above threshold ionisation or ATI.

ATI occurs only in intense fields. A free electron cannot absorb a photon as it is impossible for both energy and momentum to be conserved. The conservation rules can, however, be satisfied when the electron is coupled to the ion by the Coulomb interaction. In weak field ionisation, the electron has left the region of the strong Coulomb field before there is a high probability of absorbing another photon, while in an intense laser field there is a high probability of absorption of further photons while the 'ionised' electron is still near the

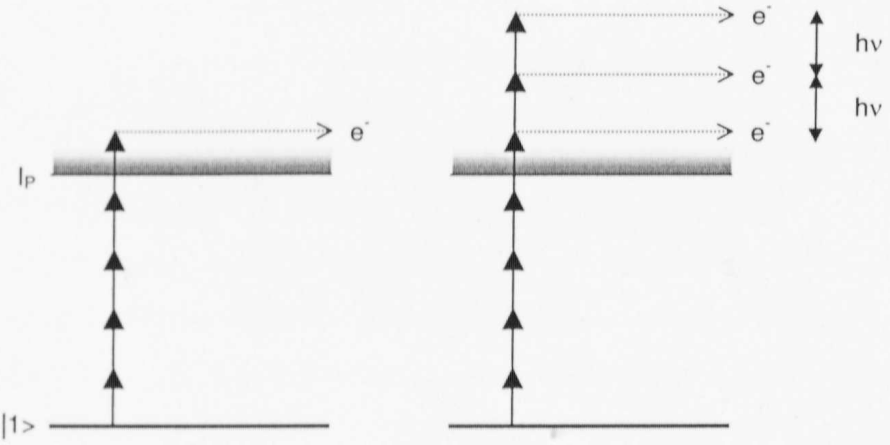


Figure 2.1. Above-threshold ionisation. At very high light intensities the electron energy spectrum following multiphoton ionisation of an atom changes from a single well-defined threshold peak (a) into multiple peaks separated from one another by the photon energy (b). These peaks are due to ionisation following the absorption of more than the minimum number of photons.

ion core.

By examining the photoelectron spectra, it can be seen that ATI cannot adequately be described by perturbation theory. Contrary to the expectations of perturbation theory, the intensity of the photoelectron peaks does not decrease rapidly with increasing order but reaches a plateau at ~10th order [Paulus 1994].

In the tunnelling regime where $U_P > I_P \gg h\nu$ and $\gamma < 1$, ATI occurs as a two-stage process [Corkum 1989]. The first stage is the ionisation stage, where the electron is released from the atom near the peak amplitude of the oscillating field with zero initial velocity. In the second (above-threshold) stage, the electron moves in the strong field and is periodically returned to the ion. Ionisation occurs when it does not return to the nucleus. The ATI energy depends on the drift velocity that the electron gains from the field and therefore on the phase of the field at which the electron is born.

In a linearly polarised laser field, $E = E_{0x}\cos\omega t$, the electron has a velocity

$$v_x = \frac{eE_{0x}}{m_e\omega}\left(\sin\omega t - \sin\omega t'\right) \tag{2.1}$$

where t' is the time at which the electron was born (so the electron has zero velocity at birth). Averaged over a laser cycle, its mean energy is proportional to $\sin^2\Delta\phi$, where $\Delta\phi$ is the phase difference between the peak of the electric field and the time at which the electron is ionised. The ATI energy is then zero at the peak of the field, where the ionisation rate is highest. This results in a cold plasma. Measurements of the ATI spectra from He irradiated at 7×10^{15} Wcm^{-2} [Mohideen 1993] produced an electron spectrum which was a good fit to a 30 eV Maxwellian, compared to the ponderomotive energy of 430 eV. The resulting ion energies are even lower, typically only a few eV [Glover 1994].

In a circularly polarised field, the electron always drifts perpendicular to the field in which it was released and its energy is independent of the phase of the field [Corkum 1989]. The electron energy spectrum is significantly hotter in this case. Mohideen *et al* [1993] reported a spectrum centred at 65 eV with circularly polarised light.

2.3.2 Stimulated Raman scattering

A third electron heating mechanism is 'stimulated Raman scattering' (SRS), which is the decay of an electromagnetic wave (with frequency ω and wavenumber k) into an electron plasma wave (ω_p, k_p) and a scattered electromagnetic wave (ω_s, k_s). The frequencies and wavenumbers obey the relations

$$\begin{aligned}\omega &= \omega_p + \omega_s \\ \mathbf{k} &= \mathbf{k}_p + \mathbf{k}_s\end{aligned} \tag{2.2}$$

The minimum frequency of a light wave in plasma is ω_p, so SRS requires that $\omega > 2\omega_p$, i.e. $n_e < n_{critical}/4$.

The energy transferred to the plasma wave heats the plasma as the electron wave damps. As the electron plasma wave can have a phase velocity close to the speed of light it can produce extremely energetic electrons when it damps [Kruer 1988]. For example, 2 MeV electrons have been measured from SRS in a He plasma with an electron density of ~ 10^{19} cm^{-3} irradiated by 600 fs, 1mm pulses with intensities of 8×10^{17} Wcm^{-2} [Coverdale 1995].

The scattered and plasma waves grow exponentially due to a feedback loop which creates an instability. If a light wave propagates through a plasma with density fluctuations it generates a transverse current. This current generates a scattered light wave. The scattered wave interferes with the incident light to produce a variation in wave pressure, which can in turn create density fluctuations.

SRS from ultrashort laser pulses differs from that observed with longer pulses as the laser pulse duration is comparable to the instability growth time [Darrow 1992]. With sub-picosecond laser pulses, heating through Raman scattering becomes significant only at high intensities. Blyth *et al* [1995] found that the SRS reflectivity of a Ne plasma increased by four orders of magnitude as the intensity of their 350 fs, 248 nm pulses increased by only a factor of three, from $1 - 3 \times 10^{17}$ Wcm^{-2}. Electron temperatures in excess of 1 keV were also measured.

The intensities at which we would expect to observe significant electron heating through SRS are far higher than the intensities at which the experiments described in Chapters Five and Six of this thesis were performed. However, it should be noted that several of the experiments performed by other groups were at intensities in excess of 10^{18} Wcm^{-2} [McPherson 1994a, Borisov 1996, Kondo 1997, Dobosz 1998] and the possibility of a contribution to the electron heating from SRS should not be neglected. McPherson *et al* [1996] have, in fact, looked for forward Raman scattering from a gas of Xe clusters irradiated at 10^{19} Wcm^{-2} and found that it does not occur at significant levels. They suggested that the growth of the Raman wave was suppressed due to absorption of the Raman wave by the clusters and electrons being forced out of the focal region due to the high ponderomotive force.

2.3.3 Inverse Bremsstrahlung

When an oscillating electron collides with a charged ion it is able to absorb energy from the laser field – this is collisional heating or inverse Bremsstrahlung. As discussed in Chapter 1, the energy an electron gains by oscillating in the laser field returns to zero as the

laser field passes unless the electron is perturbed in some way. If the electron undergoes a collision which dephases it, the electron maintains energy after the field has passed.

If the electrons are scattered at a collision frequency ν_{ei}, the rate at which the oscillatory energy of electrons is randomised by scattering is given by

$$\frac{\partial U}{\partial t} = \frac{1}{2} n_e m_e \mathrm{v}_{osc}^2 \nu_{ei} . \tag{2.3}$$

In a collisional plasma, the oscillation velocity is [Kruer 1988]

$$\mathbf{v}_{\mathrm{osc}} = -\frac{ie\mathbf{E}}{m(\omega + i\nu_{ei})} \tag{2.4}$$

so

$$\frac{\partial U}{\partial t} = \frac{\nu_{ei}\omega_p E^2}{8\pi(\omega^2 + \nu_{ei}^2)} . \tag{2.5}$$

The electron-ion collision frequencies have been calculated by Silin [1965] from the plasma kinetic equation. In the limits where the electron thermal velocity, v_{kT}, is very much smaller or larger than the oscillation velocity in the laser field, v_{osc}, the Silin collision frequencies have exact solutions. The collision frequencies, ν_{Silin}, in these limits are given by

$$\begin{aligned} \nu_{Silin} &= \frac{4}{9}\left(\frac{2\pi}{3}\right)^{1/2} \frac{Z^2 e^4 n_i}{m_e^{1/2}(k_B T_e)^{3/2}} \ln\Lambda, \quad \mathrm{v}_{osc} << \mathrm{v}_{kT} \\ \nu_{Silin} &= \frac{16 Z^2 e n_i m_e \omega^3}{E^3}\left(\ln\left[\frac{\mathrm{v}_{osc}}{2\mathrm{v}_{kT}}\right] + 1\right)\ln\Lambda, \quad \mathrm{v}_{osc} >> \mathrm{v}_{kT} \end{aligned} . \tag{2.6}$$

Here, n_i is the ion density, Z is the charge per ion, k_B is the Boltzmann constant, T_e the electron temperature and $\ln\Lambda$ the Coulomb logarithm. (The Coulomb logarithm is the log of the ratio of the maximum to minimum impact parameters for an electron colliding with an ion. The maximum impact parameter is the Debye length, since other electrons in the plasma shield out the Coulomb potential over this distance. The minimum impact parameter is the larger of either the classical distance of closest approach or the DeBroglie wavelength of the electron.) At 1×10^{16} Wcm^{-2}, v_{osc} is comparable to v_{kT} at a temperature of 570 eV. Note that in the high-field limit, the collision frequency decreases with increasing laser intensity as $I^{-3/2}$.

2.4 The nanoplasma model

2.4.1 Assumptions

The nanoplasma model [Ditmire 1996] assumes that the exploding cluster is a small spherical plasma, with uniform temperature and density across the cluster and a Maxwellian electron energy distribution. If the cluster is small compared to the skin-depth, then it can be assumed that all the atoms in the cluster simultaneously experience the same laser electric field strength.

For the cluster to be treated as a plasma, it must be larger than a Debye length,

$$\lambda_D = \left(\frac{k_B T_e}{4\pi n_e e^2} \right)^{1/2}$$
$$\lambda_D[\text{Å}] = 743 \times 10^8 \left(\frac{k_B T_e[\text{eV}]}{n_e[\text{cm}^{-3}]} \right)^{1/2}, \tag{2.7}$$

where n_e is the electron density. For a solid density Xe plasma ionised to 5^+ with an electron temperature of 1 keV, the Debye length λ_D is 8 Å, which corresponds to a 40-atom Xe cluster. We expect that the nanoplasma model will not be valid for clusters of much less than a hundred atoms.

The temperature distribution across the plasma will be isotropic if the plasma is small enough and collisional enough that there are no temperature gradients. The ion density distribution is assumed to be uniform across the cluster and the expansion is assumed to be self-similar, so the density remains uniform across the cluster throughout the expansion. The electron energy distribution is assumed to be Maxwellian throughout, which is not strictly true as the hot electrons leave the cluster first. We have to assume that the electron thermalisation happens on an extremely fast time-scale.

2.4.2 Ionisation mechanisms

Ionisation in the cluster is assumed to take place through three mechanisms: tunnel ionisation by the electric field of the laser inside the cluster, thermal collisional ionisation (inverse bremsstrahlung) and collisional ionisation of the electrons driven by the laser field.

The instantaneous tunnel ionisation rate, W_{tunnel}, is given by the ADK [Ammosov 1986] formulae

$$W_{tunnel} = \omega_a \frac{(2l+1)(l+|m|)!}{2^m |m|!(l-|m|)!} \left(\frac{2e}{n^*} \right)^{n^*} \frac{1}{2\pi n^*} I_p \left(\frac{2(2I_p)^{3/2}}{E} \right)^{2n^*-|m|-1}$$
$$\times \exp\left(\frac{-2(2I_p)^{3/2}}{3E} \right) \tag{2.8}$$

where ω_a is the atomic frequency (4.3×10^{16} s^{-1}), l is the angular momentum quantum number, m is the magnetic quantum number, n^* is the effective principle quantum number, I_P is the ionisation potential in eV, and E is the instantaneous value of the electric field inside the cluster. (The ionisation rate averaged over a cycle is obtained by multiplying equation 2.8 by

$$\left(\frac{3E}{\pi(2I_P)^{3/2}}\right)^{1/2} \tag{2.9}$$

[Perelomov 1966].)

The thermal collisional ionisation rate, W_{kT}, is calculated from the Lotz empirical ionisation rate [Lotz 1968],

$$W_{kT} = n_e \frac{a_i q_i}{I_p (k_B T_e)^{1/2}} \int_{I_p/k_B T_e}^{\infty} \frac{e^{-x}}{x} dx \,. \tag{2.10}$$

Here, a_i is an empirical constant (4.5×10^{-14} eV^2 cm^{-3}) and q_i is the number of degenerate electrons in the outer shell of the ion.

The laser-driven collisional ionisation is calculated by assuming that the electrons have a pure sinusoidal velocity in the laser field. This will tend to over-estimate the ionisation rate as the electron velocity is reduced through collisions. The laser-driven ionisation rate, $W_{laser\text{-}driven}$, is given by

$$\begin{aligned} W_{laser-driven} &= n_e \sigma_i \mid v_{osc} \mid \qquad K_e > I_p \\ &= 0 \qquad\qquad\qquad K_e < I_p \end{aligned} \tag{2.11}$$

where v_{osc} is the electron velocity in the laser field, σ_i is given by

$$\sigma_i = a_i q_i \frac{\ln(K_e/I_p)}{K_e I_p} \tag{2.12}$$

and K_e is the electron kinetic energy.

2.4.3 Heating mechanisms

The heating of the cluster is assumed to be primarily through collisional heating of the electrons, although ATI heating is also included as the ionised electrons gain kinetic energy which depends on the phase of the field at ionisation. SRS heating is not considered, as we do not expect it to be important for the intensities we are considering (< 2×10^{16} Wcm^{-2}).

The collisional heating rate inside the cluster is obtained by considering the cluster to be a uniform dielectric sphere in a uniform electric field. The uniform field approximation is valid because the clusters considered here are much smaller than the skin depth (c/ω_p) and

the laser wavelength. A cluster of 4×10^6 Xe atoms has a radius of 39 nm, $1/20^{th}$ of the laser wavelength, and the skin depth is $\lambda/10$ at an electron density of $100 n_{critical}$.

The energy deposition rate per unit volume, $\partial U/\partial t$, into the cluster is given by

$$\frac{\partial U}{\partial t} = \frac{1}{4\pi} \mathbf{E}.\frac{\partial \mathbf{D}}{\partial t}, \tag{2.13}$$

where $\mathbf{D} = \varepsilon \mathbf{E}$ (ε is the dielectric constant) [Landau and Lifshitz 1960]. Over a cycle, the heating rate averages to

$$\frac{\partial U}{\partial t} = \frac{\omega}{8\pi} \mathrm{Im}[\varepsilon] |E|^2 . \tag{2.14}$$

The dielectric constant is calculated from [Kruer 1988]

$$\varepsilon = 1 - \frac{\omega_p^2}{\omega(\omega + i\nu_{ei})} \tag{2.15}$$

where ω is the laser frequency and ν_{ei} the electron-ion collision frequency. Substituting this into equation 2.14 gives the inverse Bremsstrahlung heating rate (equation 2.5) again.

The field inside a dielectric sphere in a uniform electric field, E, is related to the vacuum electric field E_0 by [Jackson 1975]

$$E = \frac{3}{|\varepsilon + 2|} E_0 . \tag{2.16}$$

The field inside the cluster is shielded from the external field when $\varepsilon < -5$ and reaches a peak relative to the external electric field when $\varepsilon = -2$.

Combining equations 2.13 to 2.16 gives

$$\frac{\partial U}{\partial t} = \frac{9\omega^2 \omega_p^2 \nu_{ei}}{8\pi} \frac{1}{9\omega^2(\omega^2 + \nu_{ei}^2) + \omega_p^2(\omega_p{}^2 - 6\omega^2)} |E_0|^2 . \tag{2.17}$$

The heating rate per electron calculated from this equation is shown in figure 2.2 as a function of the electron density n_e for three values of ν_{ei}/ω. The heating rate in the cluster has a maximum at $n_e = 3n_{critical}$ and this maximum heating rate is higher and sharper for lower values of ν_{ei}/ω.

2.4.4 Electron–ion collisions

The electron-ion collisional frequency in the cluster is calculated from the Silin formulae [Silin 1965] (equation 2.6). These formulae have exact solutions only in the limits where the electron thermal velocity, v_{kT}, is very much smaller or larger than the energy of oscillation in the laser field, v_{osc}. Between these two limits, an approximate analytical fit to the numerical solution of the Silin equations is used.

The Silin formulae return an unphysically high collision frequency, so to ensure that the maximum collision frequency is always less than the laser frequency we take the

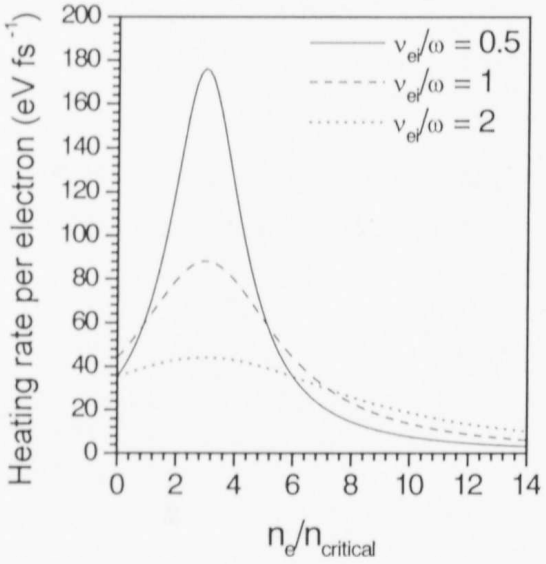


Figure 2.2. Heating rate per electron for a cluster irradiated by a 780 nm laser pulse at 1×10^{16} Wcm^{-2}. The heating rate is shown as a function of the ratio of the electron density n_e to the critical electron density $n_{critical}$ for three different ratios of collision frequency ν_{ei} to optical frequency ω.

harmonic average of the Silin collision frequency and the laser frequency. This gives a collision frequency, ν_{ei}, of

$$\frac{1}{\nu_{ei}} = \frac{1}{\nu_{Silin}} + \frac{1}{\omega}. \tag{2.18}$$

When the electron density inside the cluster is near $3\ n_{critical}$, the field inside the cluster is enhanced relative to the external field. This results in a decrease in the electron collision frequency if the electron quiver velocity in the field is larger than the thermal velocity (equation 2.6). However, as figure 2.2 shows, a decrease in the collision frequency actually results in an increase in the heating rate per electron when the electron density is close to $3\ n_{critical}$. In this way, the enhancement of the electric field at $3\ n_{critical}$ results in an increased electron heating rate.

2.4.5 Cluster expansion

The cluster expansion is driven by two mechanisms: the charge build-up on the cluster and hydrodynamic pressure from hot electrons. The hot electrons expand outwards, dragging the ions with them, so random thermal energy is converted to directed kinetic energy. The hydrodynamic pressures due to the electrons, P_e, the cold ions, P_i, (which have temperature T_i and density n_i) are given by

$$\begin{aligned} P_e &= n_e k_B T_e \\ P_i &= n_i k_B T_i \end{aligned}. \tag{2.19}$$

The Coulomb pressure $P_{Coulomb}$ from the charge Qe on a sphere of radius r is

$$P_{Coulomb} = \frac{Q^2 e^2}{8\pi r^4}. \tag{2.20}$$

The hydrodynamic pressure scales as $1/r^3$ (through the electron density n_e) while the Coulomb pressure scales as $1/r^4$. This means that Coulomb pressure is expected to be relatively more important for smaller clusters.

The cluster expansion rate is calculated by equating the rate of change of the cluster kinetic energy, $K_{cluster}$, with the rate at which work is done by the plasma in its expansion [Haught 1970].

$$P_{total} 4\pi r^2 \frac{\partial r}{\partial t} = \frac{\partial K_{cluster}}{\partial t} = \frac{1}{2} M_{cluster} \frac{\partial}{\partial t}\left(\frac{\partial r}{\partial t}\right)^2 . \tag{2.21}$$

Here, P_{total} is the total hydrodynamic and Coulomb pressure and $M_{cluster}$ is the cluster mass. The equation of the radius of the cluster obtained from this is

$$\frac{\partial^2 r}{\partial t^2} = 3\frac{P_{total}}{n_i m_i + n_e m_e}\frac{1}{r} . \tag{2.22}$$

The charge build up on the cluster is due to electrons free-streaming from the surface of the sphere. To be able to do this, the electrons must be less than one mean free path (in the direction of travel) from the surface and have an energy greater than the escape energy of the cluster. The electron mean free path is given by the Spitzer formula [Spitzer 1962],

$$\lambda_e = \frac{(k_B T_e)^2}{4\pi n_e (Z+1) e^4 \ln\Lambda} . \tag{2.23}$$

The escape energy, K_{escape}, is calculated from the potential energy on the surface of a sphere with charge Q. If the charge is distributed isotropically over the sphere, it acts as a point charge at the centre giving an escape energy of

$$K_{escape} = \frac{(Q+1)e^2}{r} . \tag{2.24}$$

2.4.6 Electron and ion temperatures

The electron and ion temperatures are calculated by accounting for the change of temperature due to the cluster expansion, electron-ion equilibration and heating of the cluster electrons,

$$\begin{aligned} \frac{\partial T_e}{\partial t} &= \left.\frac{\partial T_e}{\partial t}\right|_{\text{expansion}} + \left.\frac{\partial T_e}{\partial t}\right|_{\text{equilibration}} + \left.\frac{\partial T_e}{\partial t}\right|_{\text{heating}} \\ \frac{\partial T_i}{\partial t} &= \left.\frac{\partial T_i}{\partial t}\right|_{\text{expansion}} + \left.\frac{\partial T_i}{\partial t}\right|_{\text{equilibration}} \end{aligned} . \tag{2.25}$$

The electron temperatures are also scaled with the number of free electrons in the cluster to ensure that the total electron energy is conserved. Upon ionisation, tunnel and laser-driven collisionally ionised electrons gain kinetic energy which depends on the phase of the field at ionisation (ATI heating). The laser-driven collisionally ionised electrons are

assumed to result from an elastic collision which gives the two electrons the same thermal energy.

The change of temperature due to expansion arises because hydrodynamic pressure is the conversion of random thermal energy to directed kinetic energy. This is calculated by equating the rate at which work is done by the plasma in its expansion with the rate of change of thermal energy, so for the ions,

$$P_i 4\pi r^2 \frac{\partial r}{\partial t} = -\frac{3}{2}\left(\frac{4}{3}\pi r^3\right) n_i k_B \frac{\partial T_i}{\partial t}, \tag{2.26}$$

which gives

$$\left.\frac{\partial T_i}{\partial t}\right|_{\text{expansion}} = -2\frac{T_i}{r}\frac{\partial r}{\partial t} \tag{2.27}$$

and similarly for the electrons.

The total rate of change of electron and ion temperatures are

$$\begin{aligned} \frac{\partial T_e}{\partial t} &= -2\frac{T_e}{r}\frac{\partial r}{\partial t} - \frac{T_e - T_i}{\tau_{\text{equilibration}}} + \frac{2}{3n_e}\frac{\partial U}{\partial t} \\ \frac{\partial T_i}{\partial t} &= -2\frac{T_i}{r}\frac{\partial r}{\partial t} + \frac{T_e - T_i}{\tau_{\text{equilibration}}} \end{aligned}, \tag{2.28}$$

where the electron-ion equilibration time $\tau_{equilibration}$ is given by the standard Spitzer formula [Spitzer 1962]

$$\tau_{\text{equilibration}} = \frac{3m_e m_i}{8\sqrt{2\pi} n_i Z^2 e^4 \ln\Lambda}\left(\frac{k_B T_e}{m_e} + \frac{k_B T_i}{m_i}\right)^{3/2}. \tag{2.29}$$

2.4.7 Running the model

Equations 2.8 and 2.10 to 2.29 are combined to produce a numerical model of the interaction of a cluster of atoms with a high-intensity femtosecond laser field. The input laser parameters are the frequency, peak intensity and pulse-shape of the laser field (normally set to be Gaussian, or a sum of Gaussians to model the effects of any pre-pulse and pedestal). The density of ions in the cluster is assumed to be the same as the density of the bulk solid [Briant 1975].

At each timestep in the laser pulse, the tunnel, laser-driven and thermal ionisation rates are calculated using equations 2.8, 2.10 and 2.11. The number of ions in each charge state is then found. The total charge on the cluster after free-streaming of electrons (equations 2.23 and 2.24) is computed, together with the cluster radius and radial velocity (equation 2.22). The new number density of ions and electrons is then calculated. The ion and electron energies can then be found from equation 2.28.

To find the electron energy distribution, it is assumed that the energy distribution of electrons inside the cluster is Maxwellian at all times. All electrons with energy greater than the escape energy and within one mean free path of the surface are allowed to leave the cluster (and the energy distribution in the cluster re-thermalises). The energy distribution of the electrons which have left the cluster is then just the sum of the hot tails of these Maxwellian distributions.

This loop is repeated until the laser pulse has passed (3 pulsewidths after the peak). At this point the (low-energy) electrons remaining inside the cluster are added on to the distribution as it is assumed that they will all eventually reach the detector. The model produces a large set of output files, showing the final electron energy and ion charge state distribution as well as parameters such as cluster radius, electron energy and electric field inside the cluster as a function of time through the explosion. The model runs 60,000 timesteps in about 15 minutes on a Pentium 133.

2.4.8 Predictions of the nanoplasma model

The time-history of an exploding cluster of 5000 xenon atoms irradiated by a 200 fs, 780 nm laser pulse with a peak intensity of 1×10^{16} Wcm^{-2} is illustrated in figures 2.3 to 2.9. The peak of the laser pulse is at $t = 0$ fs.

Early on in the laser pulse, at around t = -280 fs when the intensity is $\sim 4 \times 10^{13}$ Wcm^{-2}, a few free electrons are created through tunnel ionisation (figure 2.3b).

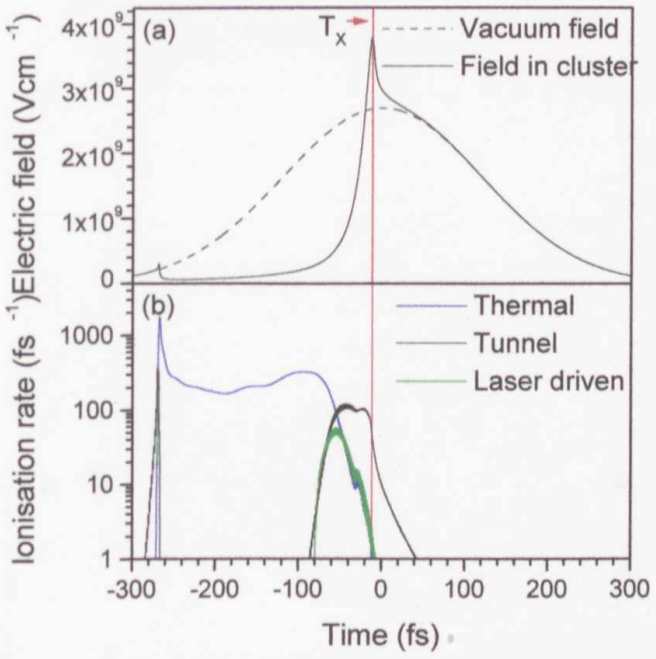


Figure 2.3. Irradiation of a 5000-atom Xe cluster by a 200 fs, 780 nm laser pulse with a peak intensity of 10^{16} Wcm^{-2}. (a) The envelope of the vacuum electric field due to the laser pulse and the electric field in the cluster. (b) Ionisation rates due to thermal, tunnel and laser-driven collisional ionisation. The red vertical line marks T_X, the point where the electron density drops through 3 $n_{critical}$.

The electron density rises to reach three times the critical electron density at t = -270 fs (figure 2.4). At this point the field in the cluster is enhanced (figure 2.3a) and more electrons are liberated through tunnel, laser-driven and thermal ionisation. The electron density is now higher than $3\ n_{critical}$ and the field inside the cluster is shielded from the external laser field.

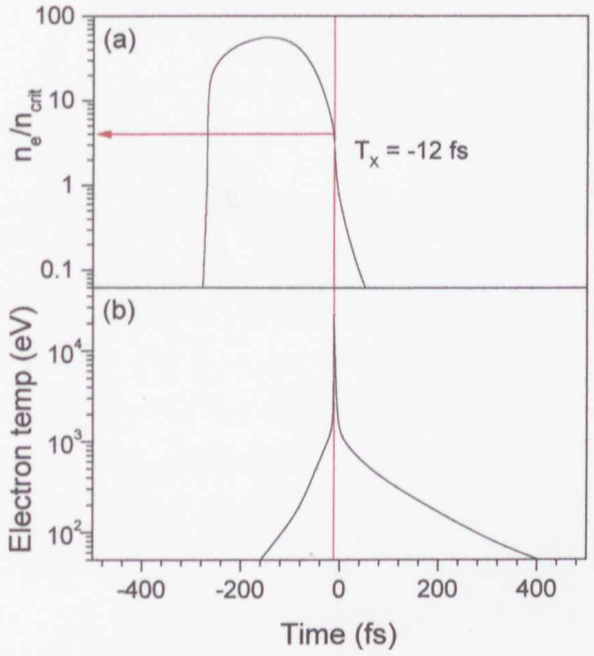


Figure 2.4. (a) The ratio of the electron density in the cluster, n_e, to the critical electron density $n_{critical}$.. (b) Electron temperature.

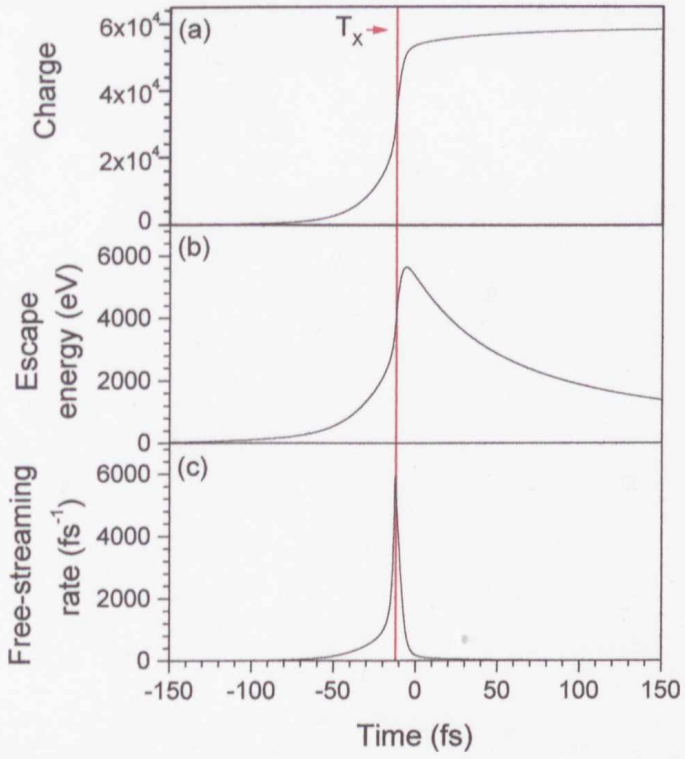


Figure 2.5. (a) The charge build-up on the cluster (b) Escape energy. (c) Electron free-streaming rate.

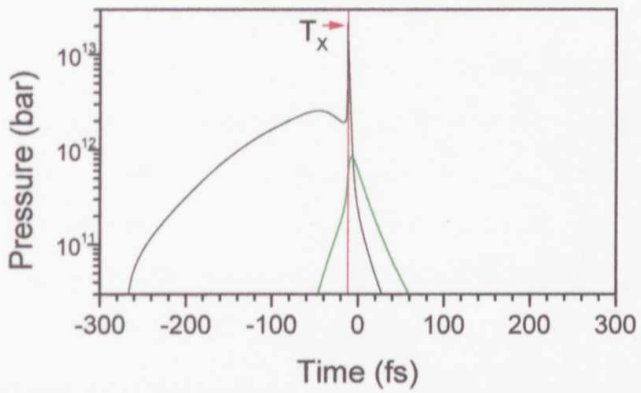


Figure 2.6. Hydrodynamic pressure from the electrons (black) and Coulomb pressure due to charge build-up on the cluster (green).

The tunnel and laser-driven ionisation rates fall off, but electrons are still created through thermal collisions.

From t = -50 fs onwards, some electrons are able to leave the cluster (figure 2.5), as the mean electron temperature is in the region of 100 – 1000 eV and the escape energy is ~ 200 – 2000 eV. The combined effect of the free-streaming of electrons out of the cluster and the hydrodynamic pressure of the electrons causing the cluster to expand is that the electron density starts to fall, after peaking at over 50 times the critical density. The field in the cluster again starts to rise as the electron density drops, so the tunnel and laser-driven ionisation rates increase while the thermal ionisation rate falls. Near the peak of the laser pulse, at t = -12 fs, the electron density in the cluster drops to $3\ n_{critical}$ (this time is marked

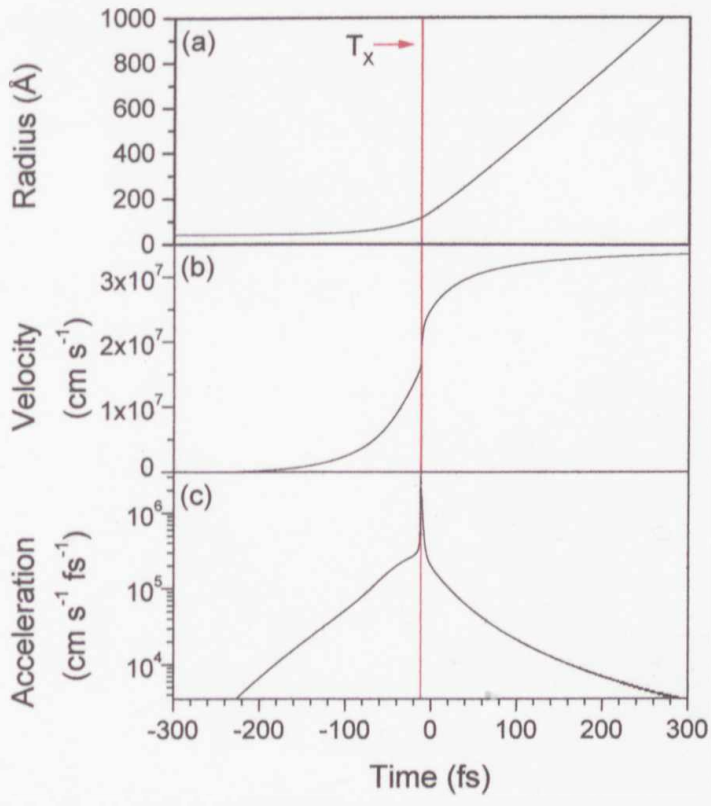


Figure 2.7. (a) Cluster radius, (b) expansion velocity and (c) acceleration.

with a vertical red line in all the time-history plots). The increased heating rate causes the electron temperature in the cluster to soar to 25 keV (figure 2.4b). The field in the cluster is also strongly enhanced and the peak intensity in the cluster reaches 2×10^{16} Wcm^{-2}, twice the intensity outside. The electron free-streaming rate (figure 2.5) increases sharply as a significant number of electrons have energies above the 4 keV escape energy.

The total charge on the cluster increases to 5.5×10^4 e, resulting in the Coulomb pressure increasing to 10 Mbar (figure 2.6). However, this is small compared to the hydrodynamic pressure due to the hot electrons of 200 Mbar. This pressure causes a sharp increase in the cluster expansion velocity (figure 2.7) as the cluster starts to explode. The final expansion velocity of the cluster is 3.3×10^7 cms^{-1}, which corresponds to a maximum ion energy of 79 keV. The ion velocity increases linearly with cluster radius from zero at the centre of the cluster, so the mean ion energy $\overline{E}$ is related to the maximum by

$$\overline{E} = \frac{3}{5}\left(\frac{1}{2} m_i v_{\text{expand}}^2\right) = \frac{3}{5} E_{\max} . \tag{2.30}$$

The average ion energy of the explosion is then 48 keV. The final electron energy is much lower, only 30 eV, as energy is transferred from hot electrons to ions in the hydrodynamic expansion. The ion temperatures never exceed a few eV during the explosion.

The ions are stripped to very high charge states: the final charge state distribution (figure 2.8) shows ions from Xe^{11+} to Xe^{16+}. The over-the-barrier threshold intensities for these charge states are $1-3 \times 10^{17}$ Wcm^{-2} for monatomic xenon (equation 1.4) [Augst 1989]. Higher charge states are therefore expected to be produced for the same peak laser intensity interacting with a cluster than with a low density gas.

Figure 2.9 shows the energy distribution of all the electrons that leave the cluster during the explosion. The model predicts that the electron energy distribution will have a characteristic double-peaked shape. The hottest peak, at ~7 keV for this set of conditions, is due to electrons which leave the cluster as the electron density drops through $3\, n_{critical}$,

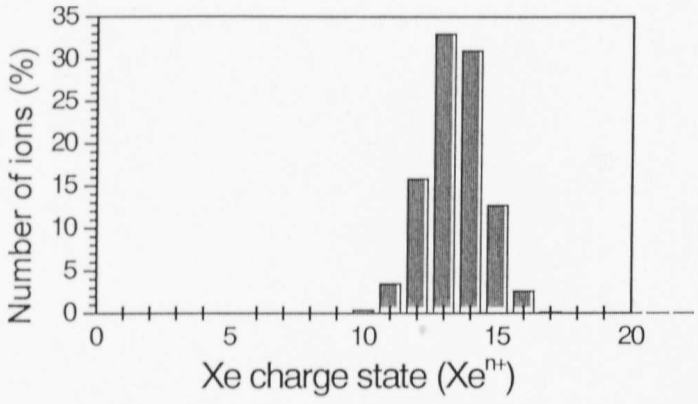


Figure 2.8. Calculated ion charge state distribution following the irradiation of a 5000-atom Xe cluster by a 200 fs, 780 nm laser pulse with a peak intensity of 10^{16} Wcm^{-2}.

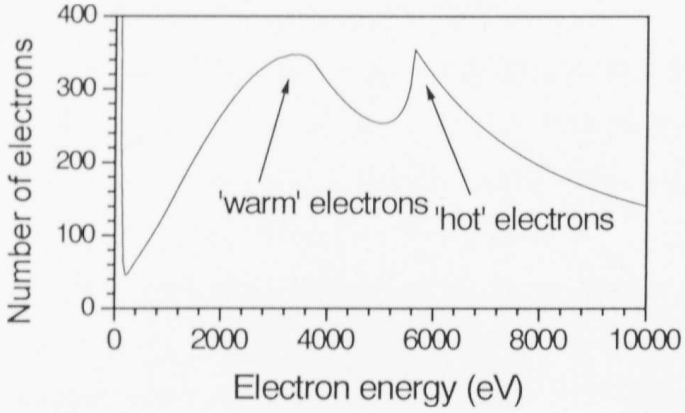


Figure 2.9. Energy distribution of electrons which leave the cluster during the explosion.

following a period of extremely high collisional heating rates in the cluster. The 'warm' peak comes from electrons which have predominantly been ionised through tunnel and laser-driven ionisation and which leave the cluster earlier in the explosion, from about t = -50 fs onwards. This group of electrons forms the 'warm' lobe of the electron distribution. The group of electrons with energies less than ~200 eV consists almost entirely of those which remain in the cluster after the laser pulse has passed.

2.5 Discussion and conclusions

The nanoplasma model of a cluster as small spherical plasma is expected to be valid for cluster sizes from few hundred atoms (so the cluster is larger than a Debye length) to a few hundred thousand atoms (so that it is small compared to the skin depth and the laser wavelength and so experiences a uniform electric field).

After ionisation, a significant proportion of electrons are retained within the cluster by the space-charge of the ions, which means that both thermal and laser-driven collisional ionisation (inverse bremsstrahlung) occurs within the cluster. ATI heating is also included as the ionised electrons gain kinetic energy which depends on the phase of the field at ionisation. SRS heating is not considered, as we do not expect it to be important for the intensities we are considering ($< 2 \times 10^{16}$ Wcm^{-2}), but this means that the model may not be valid for intensities greater than ~ 10^{17} Wcm^{-2}.

The presence of the free electrons means that the field inside the cluster can be shielded or enhanced relative to the external laser field. The enhancement is maximised when the electron density is three times the critical electron density. There is a sharp increase in the collisional heating when the electron density drops to this point. This causes a rapid jump in the electron temperature, which increases the hydrodynamic pressure and causes the cluster to explode.

The two-dimensional model of a cluster as an array of potential wells [Hu 1997b] treats the field inside the cluster as being shielded by equation 2.16, where the dielectric constant ε is calculated from that of a solid density cluster of Ar^+ ions, rather than from equation 2.15. The $3\, n_{critical}$ resonance is ignored. It is considered to have little effect on the cluster dynamics as the electron density sweeps through this point extremely fast. This is in direct contrast to the predictions of the nanoplasma model, where the explosion is driven by the enhancement of the electron heating at $3\, n_{critical}$.

As the electrons are retained within the cluster and the electron temperature is so high, the nanoplasma model predicts that the expansion is primarily due to the hydrodynamic pressure of the hot electrons rather than the Coulomb pressure of the ions. As the cluster size decreases, the scalings of Coulomb and hydrodynamic pressure with cluster size mean that Coulomb pressure will become relatively more important.

The model does not account for the lowering of the potential barriers due to the presence of neighbouring charged ions, as in the ionisation ignition model. However, the numerical results indicate that the final explosion energies are relatively insensitive to the initial ionisation rate. The electron density quickly rises to the point where the field inside the cluster is shielded from the laser and the ionisation is dominated by thermal collisional ionisation.

The model does also not include any estimate of inner shell excitation rates. Ionisation is assumed to be strictly sequential and no recombination is allowed to occur.

The nanoplasma model predicts that the irradiation of a cluster with high-intensity, femtosecond pulses will result in the production of keV electrons with a characteristic two-peaked distribution. The hot electron peak will be due to ions which leave the cluster just after the $3\ n_{critical}$ point, following a period of extremely high collisional heating in the cluster. The warm peak will be from electrons which have predominantly been ionised through tunnel and laser-driven ionisation and which leave the cluster earlier in the explosion. The ionisation ignition model also predicts that a pulse of hot electrons will be produced from collisionally ionised electrons. Extremely high ion kinetic energies (~ 10^5 eV) are predicted and the ions will be stripped to extremely high charge states. The ionisation ignition and inner-shell excitation/coherent electron motion models also predict the existence of highly charged ions. The nanoplasma model assumes a self-similar expansion of a uniform density plasma, which then means that the ion velocity will increase linearly outwards from zero at the centre of the cluster, resulting in a velocity distribution where the number of ions with velocity v is proportional to v^2. Although we expect that the nanoplasma model provides a good description of the heating mechanisms driving the cluster explosion, it is not expected to accurately model the expansion of the cluster after this point.

High-intensity laser systems

3.1 Introduction

Revolutionary advances in laser physics over the last few years mean that it is now possible to produce terawatt, femtosecond pulses from a system that fits on a table-top. The pulses produced by these systems can be focused to peak intensities of up to 10^{19} Wcm^{-2}. The key to producing these ultra-intense pulses without exceeding the damage threshold of the laser amplifiers is *chirped pulse amplification* (CPA). In this technique a short, low intensity pulse from an oscillator is stretched in time before being amplified and then compressed back down to its original pulse-length. By amplifying the stretched pulse rather than the oscillator output, high final intensities can be obtained without damaging the amplifiers. The generation of short pulses requires a laser medium with a large bandwidth and the introduction of new, broadband solid-state media, such as Titanium-doped Sapphire, has also been important in the development of these lasers.

This chapter briefly introduces the concepts of short pulse generation and amplification, especially chirped pulse amplification, and discusses the problems associated with producing and transporting short, wide-bandwidth pulses. The Blackett Laboratory Laser Consortium Ti:Sapphire CPA laser system is then described. This laser consists of a Ti:Sapphire oscillator, a pulse stretcher, a series of Ti:Sapphire amplifiers and a pulse compressor. The final output pulses are ~200 fs in duration at a wavelength of 780 nm with energies up to 45 mJ, which can be focused to intensities in excess of 2×10^{16} Wcm^{-2}. A detailed characterisation of the final output used for the experiments in this thesis is presented.

3.2 Ultrashort pulses

The bandwidth theorem states that a pulse that is short in the time domain must have a large spectrum in the frequency domain, so a laser designed to produce short pulses must have a large gain bandwidth. Transform limited pulses will always have

$$\Delta\nu\Delta\tau = k \tag{3.1}$$

where $\Delta\nu$ is the gain bandwidth, $\Delta\tau$ the pulse length and k a constant that depends on the pulse shape. k is 0.441 for Gaussian and 0.315 for sech^2 pulses. The bandwidth of a 90 fs FWHM (full width at half maximum height) sech^2 pulse, for example, is 3.5×10^{12} Hz.

The frequencies at which a laser can oscillate are determined by the mode frequencies which are covered by the gain bandwidth of the laser medium. If the laser operates in many of these modes independently, and their relative phases are random, the resulting output will be just noise (a series of identical bursts of incoherent light, spaced by the cavity round-trip time [Diels 1996]). If the cavity modes are made to oscillate with locked phases, the oscillating modes will interfere to produce a chain of evenly spaced light pulses: this is *mode-locking*. The longitudinal mode spacing, $\delta\nu_{ms}$, is determined by the cavity length, L and is

$$\delta\nu_{ms} = \frac{c}{2L}. \tag{3.2}$$

For a 1.8 m cavity, the mode spacing is 83 MHz, so there are 42,000 modes across the FWHM spectrum of a 90 fs sech^2 pulse.

The electric field amplitude of the laser pulses in time, $E(t)$, is proportional to the Fourier transform of the spectral amplitude, $E(\omega)$. If the phase difference between two consecutive modes is constant, then Fourier analysis shows that the laser pulses will be transform limited [Svelto 1989]. Pulses longer than the transform limit will be produced if the phase difference between consecutive modes is not a constant.

Figure 3.1 shows the relationship between $E(\omega)$ and $E(t)$ for a transform-limited mode-locked laser, which shows that the output is a train of pulses separated in time by $\delta t = 1/\delta\nu_{ms}$. This time δt is equal to $2L/c$ which is equivalent to the cavity round-trip time. The phase-locked modes oscillating inside the cavity can, therefore, also be considered as being an ultrashort pulse of duration $\Delta\tau$ which propagates back and forth inside the cavity.

Mode-locking not only produces pulses of very short duration but also of high peak power. A non-mode-locked laser operating on n modes has a power, $P_{non\text{-}mode\text{-}locked}$, proportional to the sum of powers in each mode,

$$P_{non-mode-locked} = \sum_{m=0}^{m=n} E_m^2 . \tag{3.3}$$

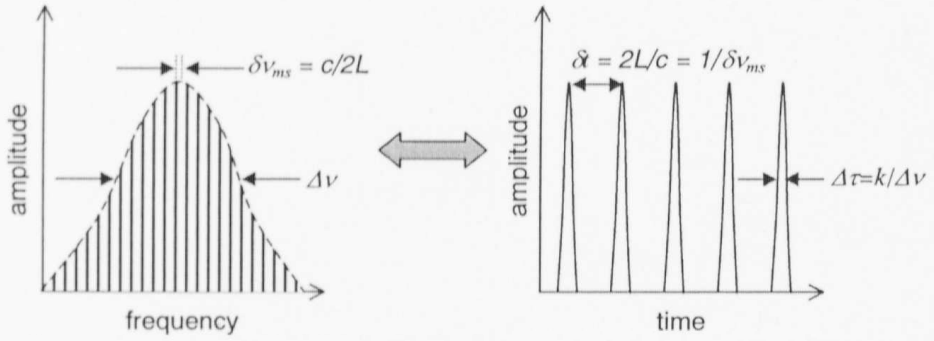


Figure 3.1. The Fourier transform of a series of modes, evenly spaced in frequency with a constant phase difference between them, is a train of pulses. The width and shape of the envelope of the series of modes determines the shape and length of the pulses. The separation of the modes determines the separation of the pulses. $\delta\nu_{ms}$ is the mode spacing, L is the cavity length, c the speed of light, $\Delta\nu$ the spectral bandwidth, $\Delta\tau$ the pulse length and δt the time between pulses.

However, for a mode-locked laser, the peak power is proportional to

$$P_{mode-locked} = \left(\sum_{m=0}^{m=n} E_m \right)^2 , \tag{3.4}$$

a factor of $\sim n$ higher than the non-mode-locked case. For example, if a laser which has an average power of 200 mW is mode-locked at the same power to produce 90 fs sech^2 pulses at a repetition rate of 83 MHz, their peak power will be 27 kW - a factor of $\sim 10^5$ higher.

A large number of mode-locking techniques have been developed, and an extensive review is given by French [1995]. The mode-locking technique used in our Ti:Sapphire oscillator is *Kerr lens mode-locking*. This relies on the nonlinear *optical Kerr effect*, which has a significant effect only at the intensities reached by the high-peak-power mode-locked pulses and not at the low average intensities of the non-mode-locked oscillator.

3.2.1 The optical Kerr effect

The refractive index of all dielectrics contains an intensity-dependent term, which is unimportant at low intensities but significant at the high intensities we are trying to access. If an electric field is applied to a dielectric a polarisation is induced. This can be written as a series expansion

$$P = \chi^{(1)}\varepsilon_0 E + \chi^{(2)}E^2 + \chi^{(3)}E^3 + \ldots \tag{3.5}$$

$\chi^{(1)}$ is very much greater than the higher-order susceptibilities, so in small electric fields a linear response is seen. The second-order term, $\chi^{(2)}E^2$, must (from symmetry arguments) be identically zero in any material that has a centrosymmetric arrangement of atoms. For certain non-centrosymmetric crystals the second order term may be dominant, and it gives rise to effects such as second harmonic generation and the Pockels effect. The third term is present in all optical materials regardless of structure. The electric displacement, $D = \varepsilon_0 E + P$, in a centrosymmetric dielectric is now given by

$$D = \varepsilon_0(1+\chi^{(1)})E + \chi^{(3)}E^3$$
$$= \varepsilon_0(1+\chi^{(1)} + \frac{1}{\varepsilon_0}\chi^{(3)}E^2)E \tag{3.6}$$

and so the refractive index, $n = D/(\varepsilon_0 E)$, becomes

$$n = (1+\chi^{(1)}) + \frac{1}{\varepsilon_0}\chi^{(3)}E^2$$
$$= n_0 + n_2 I \tag{3.7}$$

Usually, this non-linear effect is negligible. Fused silica, for example, has an n_2 of 3.2×10^{-16} cm^{2}W^{-1}. If the field is intense enough that $n_2 I$ becomes significant, two effects occur: third harmonic generation, which can usually be ignored as it is, in general, weak and not phase-matched; and a change in refractive index produced by the field itself - the *optical Kerr effect*.

3.2.2 Self-focusing and optical breakdown in dielectrics

As the intensity of a (TEM_{00}) laser beam is highest in the centre, the refractive index of the dielectric through which it passes is greater there. The dielectric acts as a graded-index positive lens and focuses the beam. This self-focusing increases as the beam propagates, until it reaches the diffraction limit or damages the dielectric (see figure 3.2a).

The accumulated phase-front distortion across the laser beam due to the nonlinear refractive index can be calculated from the breakdown integral (B-integral) [Koechner 1992],

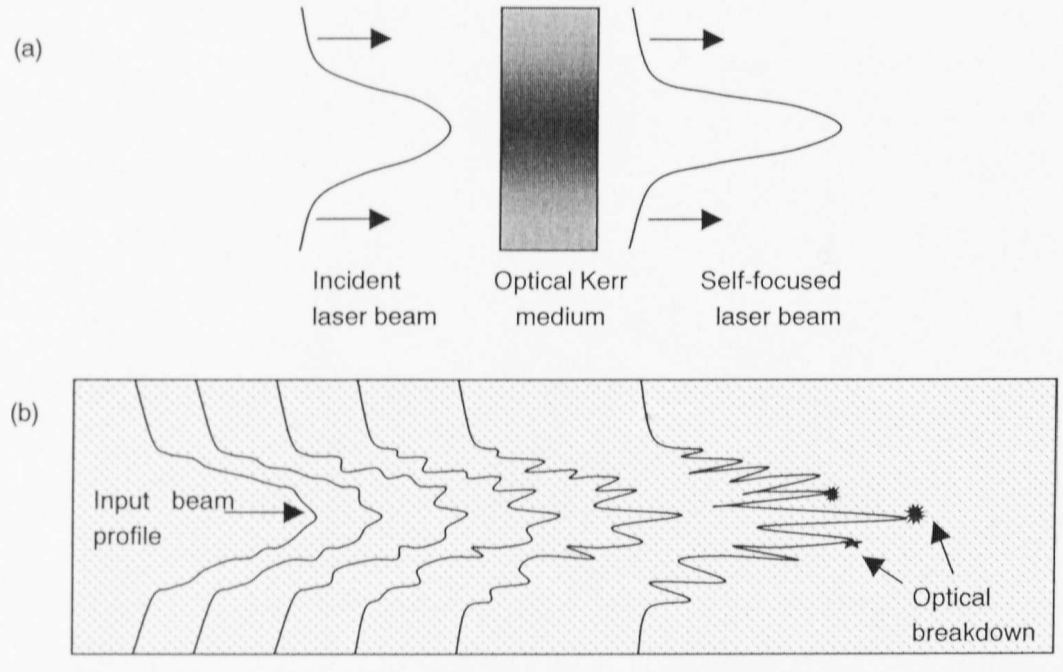


Figure 3.2 (a) Self-focusing due to the optical Kerr effect. (b) Filamentation of pulse in a Kerr medium.

$$B = \frac{2\pi}{\lambda_0} \int \frac{n_2 I}{n_0} dl \,, \tag{3.8}$$

where λ_0 is the wavelength of light in vacuum and dl is the integral along the optical path. The value of B at any position in the beam gives the phase delay (in radians) which that part of the beam has undergone compared to a low-intensity beam.

Another important consequence of the Kerr effect is small-scale self-focusing. Any initially small ripples on the beam profile grow exponentially from their original amplitude by a factor [Koechner 1992]

$$g = e^B \,, \tag{3.9}$$

where B is the B-integral (equation 3.8). The beam may then collapse into very small filaments or self-focused focal spots (figure 3.2b). The power density in these may be large enough to damage optical components or cause a breakdown.

As a general rule, the total B-integral along a laser system must be kept below 4 to maintain the optical quality of the beam.

3.2.3 Kerr lens mode-locking

The focusing due to the Kerr effect can be used to advantage to mode-lock lasers. As the highest intensity beams are focused most strongly, a laser cavity can be designed which prefers short (and therefore intense) pulses to propagate (see figure 3.3) because they see less loss. Spence *et al* [1991] were the first to observe and use this technique. They found that their Ti:Sapphire laser cavity could be made to mode-lock by slightly misaligning the end mirrors and then tapping them to introduce a noise spike. Kerr lens mode-locking (KLM) is now widely used to generate pulses of ~10 - 300 fs [Asaki 1993, Fraser 1996].

One problem with KLM is that it is, in general, not self-starting - although it is self-sustaining. The short interaction length of the solid state amplifiers typically used in KLM oscillators (~20 mm) means that they are only weakly non-linear. The initial intensity

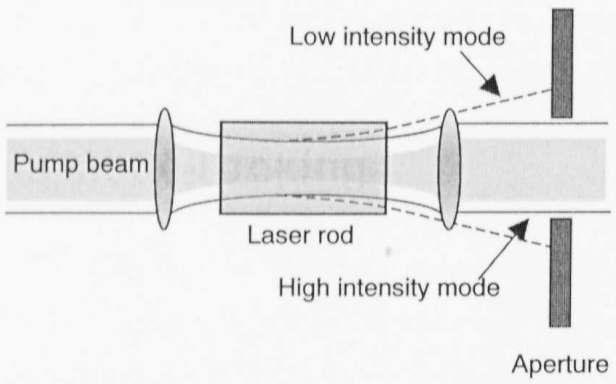


Figure 3.3 Kerr lens mode-locking. The highest intensity mode (which corresponds to short pulses) is most strongly focused by the Kerr effect in the laser rod. It is then re-collimated by the lens and passes through the aperture. Low intensity modes are only weakly focused by the Kerr effect, not re-collimated and are clipped by the aperture. The high intensity mode therefore experiences less loss.

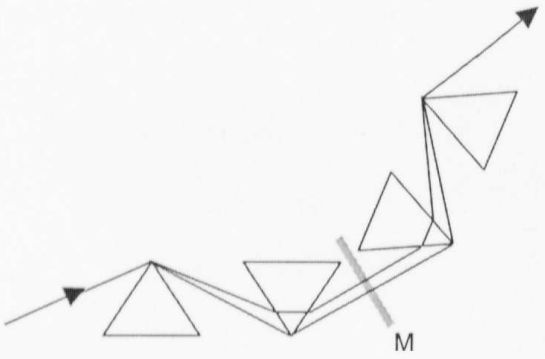


Figure 3.4 A sequence of prisms which can be adjusted to give a negative value of group velocity dispersion. The second pair of prisms can be replaced with a mirror, M.

fluctuations in a laser cavity are not usually strong enough to generate enough non-linearity to evolve into stable pulse trains. An additional mechanism is required to start the mode-locking process. Introducing a noise spike by tapping the end mirrors is a common technique, but systems involving acousto-optic modulators or saturable absorbers have also been used.

3.2.4 Group velocity dispersion

If the refractive index of a material is a function of frequency, different frequencies will propagate at different speeds. This will both chirp and broaden a pulse propagating through it, without affecting the spectral profile. This is group velocity dispersion or *GVD*. In a material with normal dispersion higher frequencies travel more slowly, giving a positive chirp.

In a laser cavity any element through which the light propagates (including air, optical components and the gain medium) will introduce dispersion. This dispersion imposes a limit on the minimum pulse duration achievable. To generate very short pulses it is necessary to control or compensate for intracavity dispersion. To do this we need to introduce a system with negative group velocity dispersion - one such system is the prism pair [Fork 1987, Martinez 1987, Treacy 1969] (see figure 3.4). The first prism provides angular dispersion due to positive GVD and the second re-collimates the components. The path between the two prisms is shorter for the higher frequencies and so introduces negative GVD. The amount of negative GVD depends on the prism separation and $(dn/d\omega)^2$, while the positive GVD component is governed by the length of the path in glass and $d^2n/d\omega^2$. The net GVD can be controlled by translating a prism along its axis of symmetry. The best remedy for dispersion in a cavity is to design the gain medium and other components such that they introduce the smallest possible amount of GVD, and then use a prism sequence just to fine-tune dispersion.

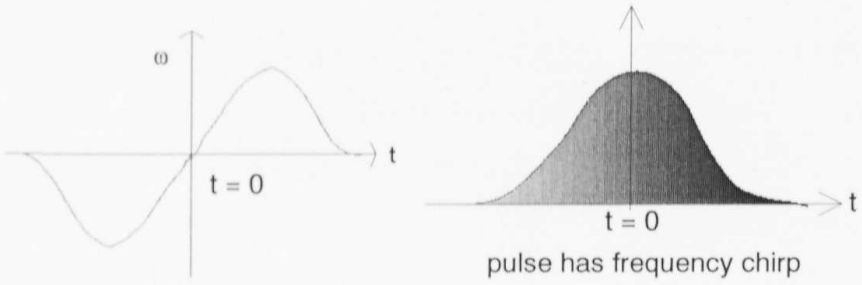


Figure 3.5 Chirped pulse. Self-phase modulation produces a frequency chirp proportional to *dI/dt* on the pulse.

3.2.5 Self-phase modulation

A laser pulse passing through a dielectric can experience the Kerr effect in the time domain. On the leading edge of the pulse, $dn/dt > 0$ and the optical frequency is lowered; on the falling edge the reverse is true and so the frequency is raised. This effect - self-phase-modulation - gives the pulse a frequency chirp (figure 3.5).

3.3 Gain media for ultrashort pulse generation

Chirped pulse amplification was first applied to Nd:glass systems [Maine 1988, Patterson 1991] but these are limited to a pulse length of ~500 fs at the TW level due to the limited bandwidth of the gain medium [Perry 1990]. To produce pulses shorter than this a laser medium with a much greater bandwidth is needed.

Although the pulses as short as 6 fs pulse have been produced from a dye laser system [Fork 1987], dye lasers have several significant disadvantages. Laser dyes (such as Rhodamine 6G) give a large gain per unit length because of their large emission cross-section, but for that reason they saturate easily. A typical saturation fluence for a dye is ~ 10^{-3} Jcm^{-2} compared to ~1 Jcm^{-2} for a solid-state laser, which means a dye-laser system capable of delivering much more than a few mJ will have an unfeasibly large aperture. Murnane and Falcone [Murnane 1988] have developed a colliding-pulse mode-locked dye laser capable of delivering 2.5 mJ in 100 fs. Dye lasers tend to suffer from problems including the photo-induced degradation of dyes, instability in jet flows and thermal effects which are difficult to control. Kerr lens mode-locking and the development of new ultra broadband solid state media mean that dye laser systems have now been superseded by solid state amplifiers, which are much more convenient to use and have greater tunability.

Titanium-doped sapphire, $Ti^{3+}Al_2O_3$, was first characterised and made to lase by Moulton [1986]. The structure of the Ti^{3+} ion is a closed shell plus single, exposed *3d* electron. It has broad absorption and emission linewidths as a consequence of the strong coupling between the vibrational energy states of the host and the electronic energy states of the active ions. Ti:Sapphire has the advantages of broad tunability (it has the widest percentage tunability of any laser), a large gain cross-section and good thermal properties compared with Nd:glass. Laser operation spanning the entire expected gain bandwidth is possible and pulses as short as 11 fs have been produced [Asaki 1993]. It exhibits very efficient (nearly quantum limited) conversion of pump energy. The main disadvantage with Ti:Sapphire is that, due to its very short upper-state lifetime of 3.2μs, it is difficult and

	Ti:Sapphire	Cr:LiSrAlF$_6$	Nd:glass	Rhodamine 6G
Tuning range (nm)	660 - 1100	750 - 950	1043 - 1063	700 - 820
Gain cross section (x 10^{-20}cm^2)	30	3.0	4.0	0.0002
Saturation fluence (Jcm^{-2})	0.8	7	4.9	0.002
Storage lifetime (μs)	3.2	67	350	0.001
n_2 (x 10^{-13})	1.3	0.5	1.5	
Thermal diffusivity (cm^{2}s^{-1})	0.15	0.019	0.003	
Maximum power (TW)	4.7	8.5	55	0.02
Shortest pulse (fs)	11	33	130	6

Table 3.1 Laser media for ultrashort pulse generation

inefficient to pump directly with flashlamps, arc lamps or laser diodes. It requires rapid pumping and so is often pumped with a frequency-doubled Nd:YAG laser.

Cr:LiSrAlF$_6$ [Payne 1989] has also been used in terawatt, femtosecond systems [Ditmire 1993]. It has a broad emission cross-section and a sufficiently long upper-state lifetime to allow flashlamp pumping. Its absorption spectrum overlaps well with the emission of xenon flashlamps; and it can also be diode pumped. It has a much lower n_2 than Ti:Sapphire, which minimises nonlinear effects during amplification.

3.4 Chirped pulse amplification

The main problem in amplifying ultrashort pulses is that the non-linear refractive index (n_2) in the gain material and other optical components at high intensities leads to beam distortions and small-scale self-focusing. The intensities in these amplified distortions often exceed the damage threshold of the material. The amplifier materials must also be chosen with care: they must have a bandwidth large enough to accommodate the full spectrum of the pulse. To extract the energy stored in the amplifier efficiently the fluence of the pulse has to be near the saturation fluence of the medium.

Chirped pulse amplification (CPA) is an idea originally adapted from radar [Klauder 1960]. Radar uses short energetic pulses - but when it was being developed no circuits could handle the required peak power. The solution was to stretch the pulse in a dispersive delay line, amplify and transmit it, and then compress the echo in a system with the opposite dispersion. In a CPA laser system an initially short pulse from a mode-locked oscillator is passed through a dispersive delay similar to that produced by a prism pair in an oscillator. It stretches the pulse and gives it a frequency chirp. The pulse can then be amplified, without reaching intensities where the Kerr effect is a problem, and then recompressed (see figure 3.6).

Treacy [1969] first pointed out that a pair of diffraction gratings with their faces and rulings parallel (figure 3.7) can be used to compress positively chirped optical pulses. The variation in phase with frequency for this system can be written as a power series expanded about the central frequency, ω_0:

$$\phi(\omega) = \phi_0 + \alpha_1(\omega - \omega_0) + \alpha_2(\omega - \omega_0)^2 + \alpha_3(\omega - \omega_0)^3 + \ldots \tag{3.10}$$

If this is then differentiated, we get the delay

$$\tau = d\phi(\omega)/d\omega = 0 + \alpha_1 + 2\alpha_2(\omega - \omega_0) + 3\alpha_3(\omega - \omega_0)^2 + \ldots \tag{3.11}$$

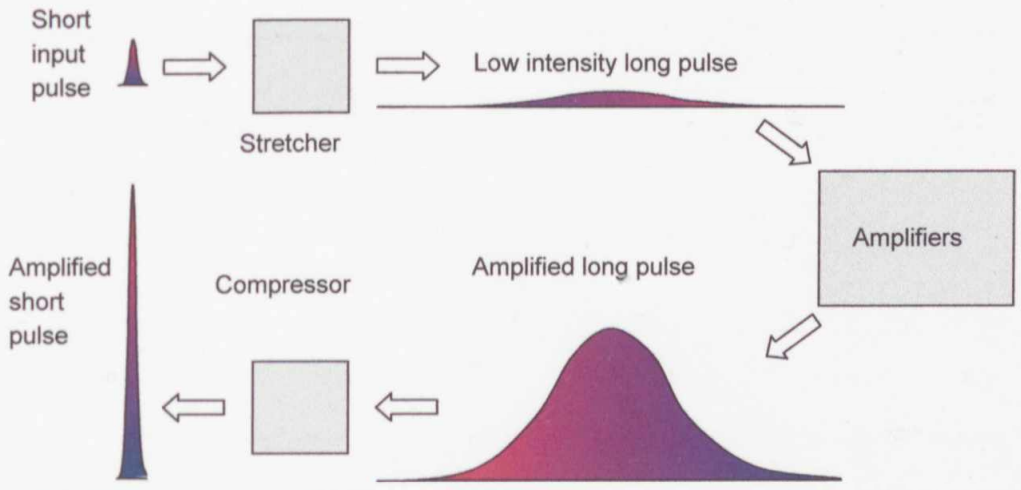


Figure 3.6. Chirped pulse amplification. An initially short pulse is stretched in time before being amplified and then recompressed

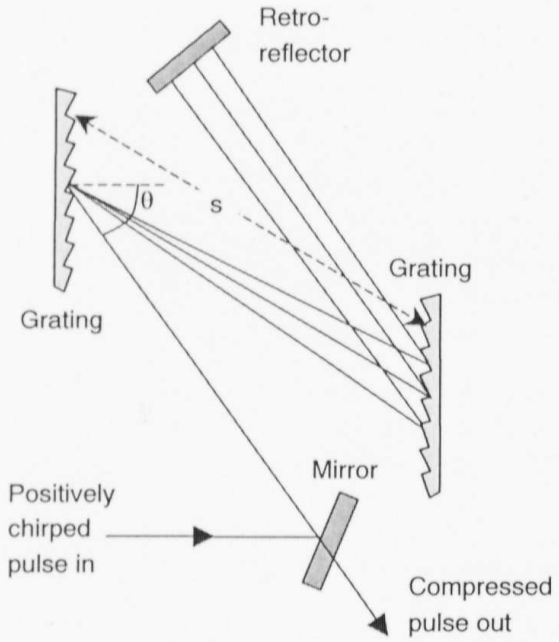


Figure 3.7 Compressor grating configuration. s is the centre wavelength separation of the compressor and θ is the input angle onto the grating from the normal.

The first non-zero term in this expression, α_1, is the group delay; the second is the linear chirp; the third, the quadratic chirp and so on. If the chirp produced by the grating pair is equal and opposite to that on the stretched pulse then the original pulse will be reproduced.

The amplification and recompression of chirped optical pulses was first demonstrated by Strickland *et al* [1985]. They stretched a 150 ps pulse to 300 ps in 1.4 km of optical fibre, amplified it and used a grating pair to compress it down to 2 ps. The interplay of self-phase-modulation and group velocity dispersion in an optical fibre both broadens the spectrum and changes the pulse shape (see figure 3.8).

The spectral broadening means that the pulse can be compressed to a fraction of its original length (to $\sim 1/\Delta\nu$). The change in pulse shape, however, puts a limit on the maximum compression ratio (defined as $\tau_{stretched}/\tau_{compressed}$) of around $\lambda/\delta\lambda$ [Perry 1994]. Attempting to compress the pulse more than this causes ripples to appear either side of the

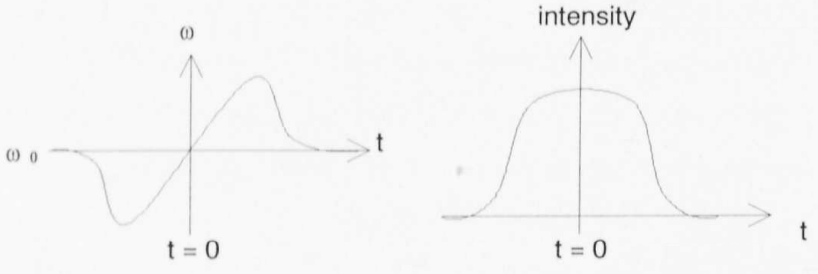


Figure 3.8 Pulse stretching in an optical fibre. Self-phase-modulation produces a frequency chirp proportional to dI/dt on the pulse. The chirp is negative on the wings of the pulse and positive near the peak. As the fibre has positive group velocity dispersion, the centre of the pulse will be stretched while the wings are sharpened. At the exit of the fibre, the pulse is rectangular.

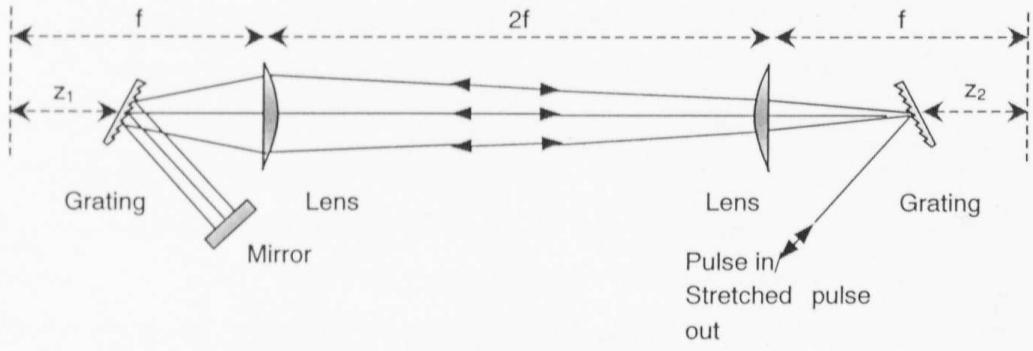


Figure 3.9 Stretcher grating configuration. The telescope inverts the angular dispersion (giving positive GVD) provided that the gratings are inside the focal planes of the lenses. The effective separation contributing to the system is then given by the sum of the distances from each grating to the adjacent focal plane, $= 2f - z_1 - z_2$.

main pulse. The stretcher and compressor are not a perfect match and dispersion can only be cancelled up to second order.

To get higher compression ratios (and so shorter pulses at higher power) the dispersion in the stretcher and compressor needs to be as closely matched as possible. Martinez [1987] showed that, by placing a telescope between the gratings in a compressor, the sign of the dispersion achieved can be inverted (see figure 3.9). The first demonstration of an all-grating system [Pessot 1987] succeeded in stretching an 83 fs pulse to 85 ps and then recompressing it to 91 fs. This is a compression ratio of 1000 - dramatically better than the maximum achievable with a fibre-grating system. The stretch factor obtained from a grating stretcher/compressor depends on the ruling of the grating and the geometry of the stretcher/compressor and is given by [Faldon 1992]

$$\tau_{stretched} = \frac{\alpha \lambda_0^2 d^2 s}{c^2 \tau_{compressed} \cos^2 \theta} \tag{3.12}$$

where $\tau_{stretched}$ and $\tau_{compressed}$ are the lengths of the stretched and compressed pulses, α is a constant that depends on the pulse-shape (0.78 for $sech^2$ pulses), d is the grating ruling density in lines/mm, s is the centre wavelength separation of the compressor, c is the speed of light and θ is the input angle on to the grating from the normal.

If the grating stretcher/compressor system is modelled paraxially and material dispersion in the lens is neglected, the stretcher produces dispersion equal and opposite to that of the compressor to all orders, provided that the grating incidence angles are the same and the compressor grating separation is equivalent to the effective grating separation in the stretcher, $2f - z_1 - z_2$ (figure 3.9).

3.4.1 Limits on the recompressed pulse duration

Transform limited recompressed pulses can be obtained if the grating stretcher/compressor gives zero net dispersion in all orders of frequency shift. In practice, however, perfect recompression is not possible - especially for very short (<30 fs) pulses with large bandwidths. There are two major factors which prevent recompression of stretched and amplified pulses back to their original length: modification of the amplitude and the phase of the spectrum. The amplitude is modified through clipping or narrowing of the spectrum, and the spectral phase is altered by the presence of higher-order phase terms which cannot be compensated for in the compressor.

3.4.1.1 Spectral clipping and narrowing

'Hard' clipping of the spectrum, where the spectrum is sharply cut-off outside a certain frequency band, has the effect of producing wings on the recompressed pulse. Hard clipping most often arises in the stretcher or compressor when the spectrum is imaged on to an optic with a finite size. Dielectric coatings on optics such as mirrors and lenses which have insufficiently broad bandwidths can also clip the spectrum.

The spectrum of the amplified pulse must be narrower than the gain bandwidth of the amplifier material. A reduction in the gain bandwidth reduces the duration of the stretched pulse, giving a longer compressed pulse [Perry 1994]. The single-pass power or intensity gain in an amplifier is given by [Siegman 1986]

$$G(\omega) = e^{2\alpha(\omega)L} \tag{3.13}$$

where $G(w)$ is the gain and $\alpha(\omega)$ the gain coefficient which is proportional to the shape of the gain bandwidth. Because $\alpha(\omega)$ appears in the exponent of the gain expression, the gain falls off rapidly with detuning. This is an important consideration in CPA systems where the overall gain can be as much as 10^{10}. For example, in a Nd:glass system Perry *et al* [1990] found that gain narrowing meant that only a ~4 nm spectrum could be maintained in the amplifier system giving a minimum compressed pulse-length of ~1 ps. The extremely high gain bandwidth of Ti:Sapphire, however, means that gain narrowing is irrelevant for pulses down to 100 fs [Le Blanc 1996].

Gain-shifting is a problem unique to CPA. When a pulse is amplified to near saturation, the lower frequencies at the front of the pulse see higher gain. This leads to a temporal (and thus spectral) reshaping of the chirped pulse - this is gain-shifting. Multi-pass amplifiers tend to produce more gain-shifting for the same total gain than do regenerative amplifiers because the pulse is amplified closer to saturation [Le Blanc 1996]. In combination with the finite bandwidth of optical elements and dielectric coatings, gain-shifting can result in narrowing of the spectrum.

3.4.1.2 High-order phase terms

In a real CPA system, there is always some dispersive mismatch between the stretcher and compressor due to material dispersion in amplifier material as well as spherical and chromatic aberrations in the stretcher telescope. Linear chirp on the pulse can be removed by adjusting the grating separation. Quadratic chirp produces pre- or post-pulses according to its sign and can be compensated for by changing the incidence angle of the beam onto the gratings. However, adjusting the compressor to eliminate linear and quadratic chirp means that it is no longer perfectly matched to the stretcher, and higher-order phase terms can no longer be perfectly cancelled. For a 20 fs system, these effects can result in pulse broadening of the order of the pulse duration [Lemoff 1993].

There are two routes to reduce the high-order phase terms: designing a system with the minimum phase distortion, and introducing extra material to cancel out the higher order phase terms. One way to reduce phase distortion is to design an 'aberration free' stretcher, as the lens in a conventional grating stretcher introduces chromatic and spherical aberration on the pulse. This approach has been taken by the group at ENSTA whose stretcher is based on the Öffner triplet [Antonetti 1997]. Their experimental results and numerical modelling by Mason [1999] have highlighted the importance of the surface quality of the stretcher optics on the contrast ratio of the compressed pulse. It is also important to reduce the material path length in the amplifiers to reduce the higher order phase distortion.

In contrast to this work, Lemoff and Barty [1993] have shown that it is possible to simultaneously eliminate GVD, third and fourth order phase by correctly choosing the separation and incidence angles of the compressor gratings and adding extra material in the amplifier path. Another approach is to introduce controlled aberrations in the stretcher which, when combined with the added GVD from the amplifier, can be compensated for in the compressor. This can be done by using an air-spaced doublet in the stretcher [White 1993] which corrects spherical and chromatic aberration. The higher order phase terms can then be controlled by adjusting the doublet spacing and position.

State of the art CPA systems such as the laser at ENSTA [Antonetti 1997] are now capable of amplifying 30 fs pulses to 0.8 J and recompressing to close to the original pulse-length with a contrast ratio of $>10^6$. Focused intensities in the region of 5×10^{19} Wcm^{-2} are now accessible.

3.5 The Blackett Laboratory Laser Consortium Ti:Sapphire CPA laser system

The laser system used for all the experiments described in this thesis was the Blackett Laboratory Laser Consortium Ti:Sapphire CPA laser system. This is a CPA laser system with a final output of ~ 40 mJ in 200 fs at 780 nm with a 10 Hz repetition rate. The focused intensities achievable exceed 10^{16} Wcm^{-2}. The system was described in its original configuration by Fraser [1996], but has since been modified. The layout of the laser, which occupies two optical tables, is shown in a block diagram (figure 3.10). It consists of a mode-locked Ti:Sapphire oscillator which produces a train of ultrashort pulses, a grating stretcher, a series of Ti:Sapphire amplifiers and a pulse compressor.

The laser has undergone two major upgrades during the course of the experiments described in this thesis. In early 1997 the stretcher and compressor were rebuilt with new,

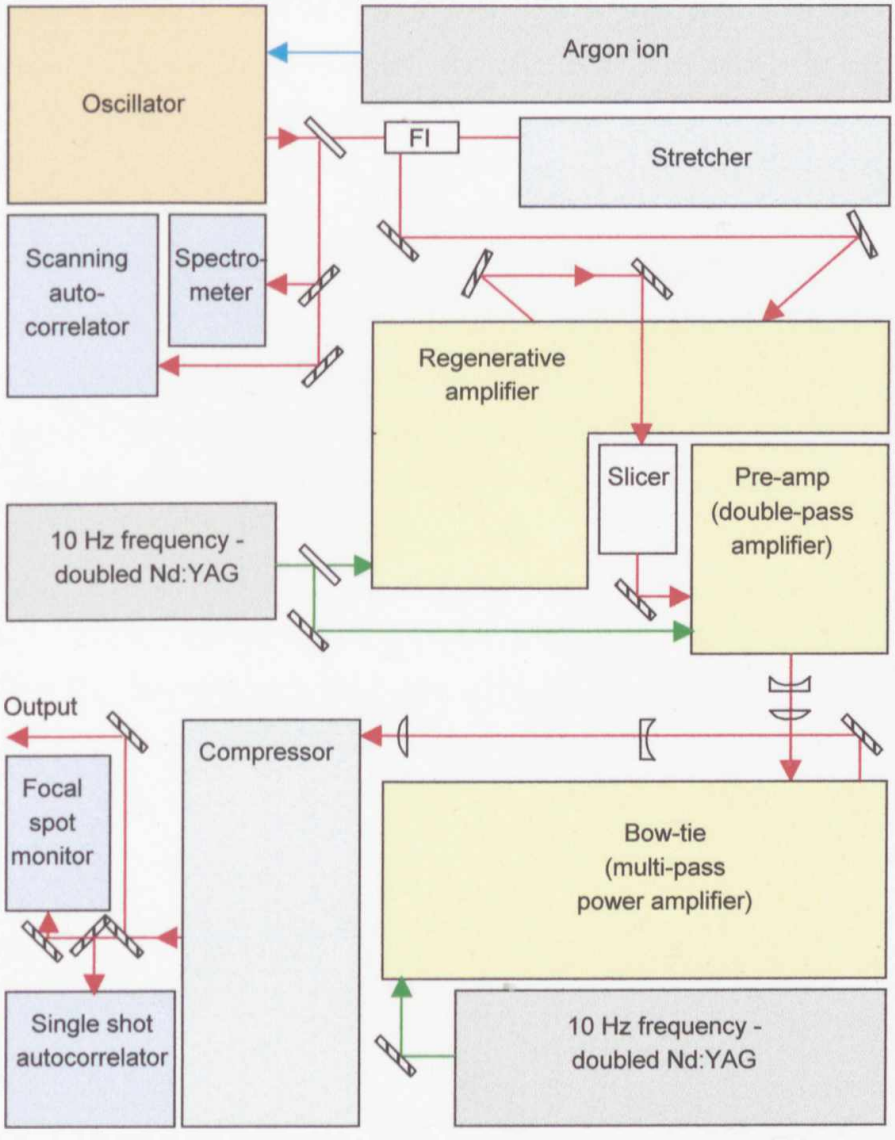


Figure 3.10. Block diagram of the Imperial College Ti:Sapphire laser system. 'FI 'is a Faraday isolator.

larger gratings to enable us to increase the diameter of the compressed output beam so that higher energy pulses could be propagated to experiments. At the same time, a single pulse isolator was added after the first stage of amplification to reduce the level of pre-pulse. In early 1998, a third amplifier stage was inserted before the final amplifier to increase the final output energy and the compressor was again rebuilt to improve the pulse contrast.

Each stage of the laser system will be described in turn, and the output of the laser in each of the three configurations used for experiments in 1996, 1997 and 1998 will be detailed.

3.5.1 The Oscillator

The source of ultrashort pulses is a Kerr lens mode-locked Ti:Sapphire oscillator (figure 3.11). The oscillator consists of a 1.8 m folded cavity, containing a 20 mm Ti:Sapphire crystal (0.05% doping). The crystal is pumped through the back of one of the curved cavity mirrors by 5.5 - 6 W from a CW argon-ion laser (Coherent Innova 100) operating on all lines in the blue-green. The cavity also contains a hard aperture to help sustain mode-locking and a prism pair to compensate for intra-cavity dispersion. An adjustable slit after the prism pair, where the spectrum is spatially dispersed, enables wavelength tuning. The oscillator is, in principle tuneable over ~50nm, but is always used at 780 nm. Mode-locking is achieved by tapping on a cavity mirror. A water-cooled copper jacket on the Ti:Sapphire crystal stabilises its temperature, and the oscillator is enclosed in a box to prevent air currents from disrupting mode-locking.

The oscillator output is monitored by a photo-diode which looks at the pulse-train, a spectrometer with a linear CCD array, and a second-order scanning auto-correlator which uses an LED as the non-linear medium [Reid 1998].

The oscillator produces 90 fs pulses (assuming a sech^2 pulse-shape) centred at 780 nm with an 80 MHz repetition rate. The average output power varies from 200 - 400 mW, equivalent to 2.5 - 5 nJ per pulse. The bandwidth is approximately 8 - 10 nm, giving a time-bandwidth product $\Delta\nu\Delta\tau$ of 0.36 - 0.44 (~1.25 × the transform limit for sech^2 pulses).

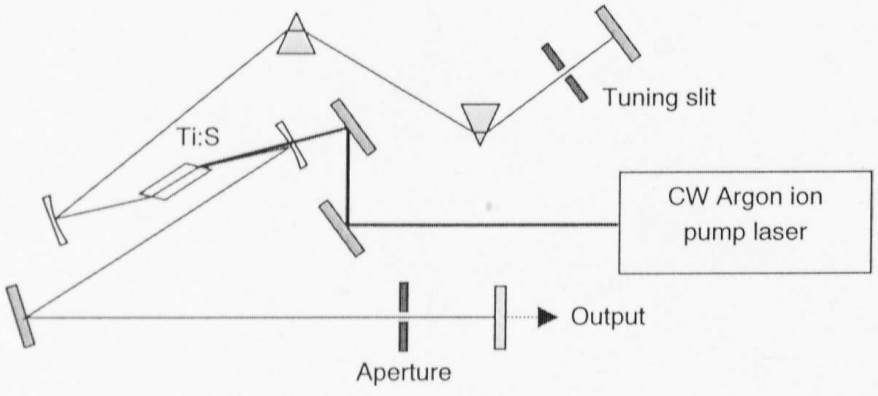


Figure 3.11 Kerr lens mode-locked Ti:sapphire oscillator.

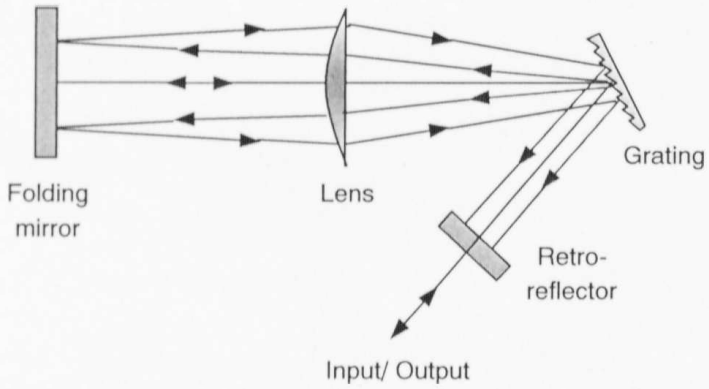


Figure 3.12. The stretcher. The retro-reflector ensures that the output beam is offset vertically from the input beam.

3.5.2 The stretcher

The oscillator pulses are then stretched in a grating stretcher (figure 3.12) by a factor of ~2500 to 250 ps (figure 3.13). The stretcher contains a single gold-coated grating which is passed four times by the beam. The beam is sent in at a slight upwards angle to ensure that the input and output beams are vertically separated from the retro-reflector. The output beam travels back along the path of the input beam until it reaches the Faraday isolator, from where it is sent to the amplifiers. Losses in the stretcher mean the pulse energy here is ~1 nJ. The single-grating stretcher is effectively the same as the two-grating stretcher illustrated in figure 3.9, but the mirror ensures that both passes of the grating have the same angle of incidence. With two-grating stretchers angular mismatch can be a problem.

A 2000 line/mm grating and a 750 mm focal-length lens were originally used in the stretcher - these were replaced in 1997 by an 1800 line/mm grating and a 1 m focal-length lens. The compressor gratings were replaced by larger ones at the same time. The aim of this change was to increase the diameter of the final pulse so that higher energies could be propagated to the experiments.

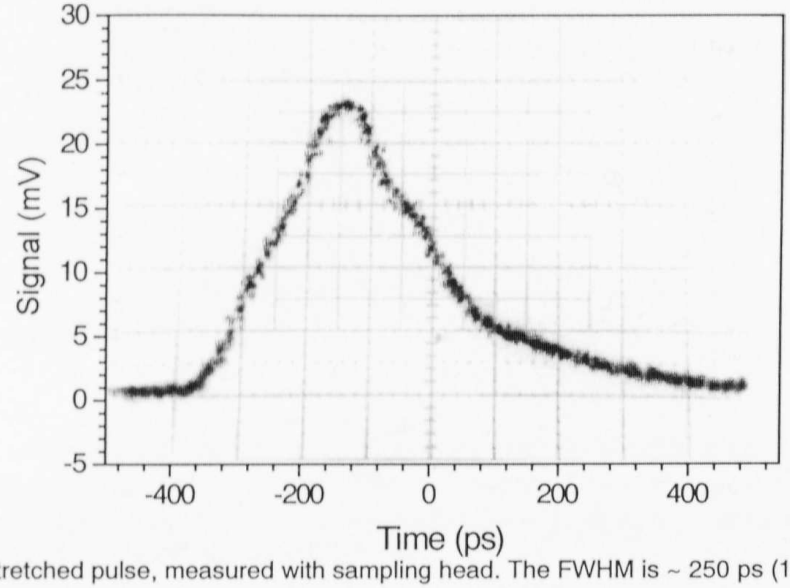


Figure 3.13. Stretched pulse, measured with sampling head. The FWHM is ~ 250 ps (1997).

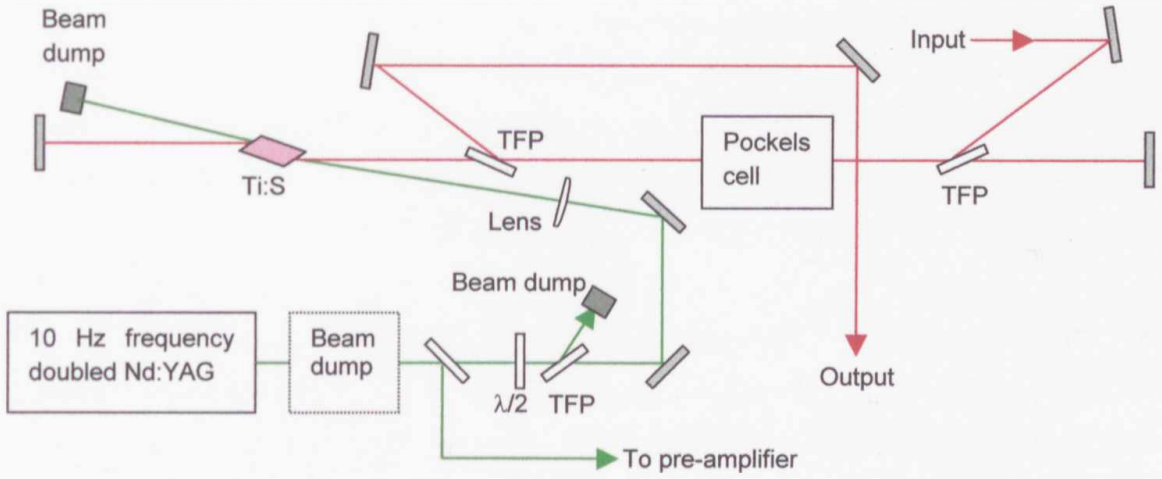


Figure 3.14. Ti:sapphire regenerative amplifier.

3.5.3 The regenerative amplifier

The first stage of amplification is a regenerative amplifier (figure 3.14) which consists of a 20 mm Ti:Sapphire crystal (0.1% wt doping) between two dielectric mirrors. The mirrors are 3 m concave and 4 m convex and the cavity length is 1.75 m, forming a stable resonator. The advantage of this configuration is that the output pulse will have the same temporal characteristics as the input pulse, but the spatial characteristics of the output will be determined by the cavity - i.e. a TEM_{00} Gaussian mode.

The amplifier is pumped at 10 Hz by 90 mJ 532 nm light from a frequency-doubled Q-switched Nd:YAG laser (Continuum Surelite II). The pump laser is focused onto the crystal by a 50 cm lens approximately 25 cm from the crystal, giving a pump fluence of ~1 Jcm^{-2}.

The cavity also contains a Pockels cell between two thin-film polarisers. The vertically polarised input pulse is injected into the cavity by reflection off one of the

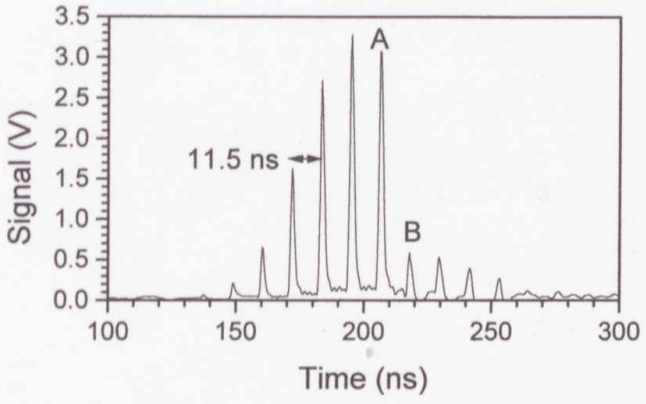


Figure 3.15. Build-up of the IR pulse in the regenerative amplifier. The timing of the switch-out is optimised (to maximise the energy and minimise the amount of pre- and post-pulse) by looking for the sharpest cut-off between the last trip in the cavity (A) and the next pulse (B). The successive pulses are separated by the cavity round-trip time of 11.5 ns.

polarisers. A 6 kV electrical signal drives the Pockels cell to the 780 nm half-wave voltage, trapping a single pulse (which is now horizontally polarised) in the cavity. The electrical pulse now travels down a delay line before returning to the Pockels cell to switch out the laser pulse after 20 cavity round-trips. The laser pulse is vertically polarised and has been amplified until close to saturation. At this stage it has been amplified by a factor of $>2 \times 10^6$ to ~2 mJ.

The build-up of the pulse in the cavity is monitored by a photodiode looking at the leakage through the back of one of the cavity mirrors (figure 3.15). A second photodiode looks at the pulse directly after the exit of the amplifier. This photodiode is used as the optical trigger for experiments as the height of the pulse remains approximately constant (independent of the final pulse energy, which is controlled later in the system) and changes only when the alignment or timing moves away from optimum. In this way, if the Pockels cell timing drifts and two lower energy pulses (separated by the round-trip time of 11.6 ns) are switched out, the data acquisition electronics stop triggering.

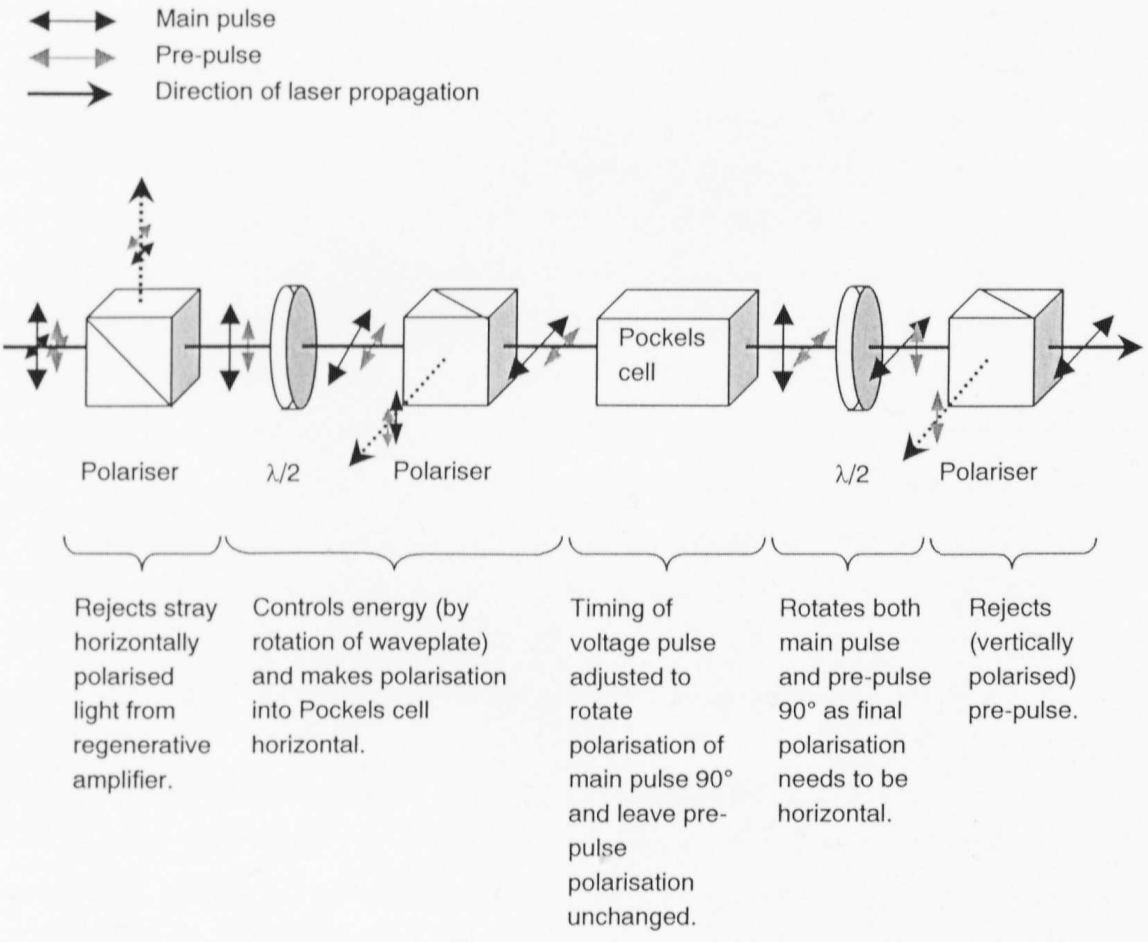


Figure 3.16 The single pulse isolator. The solid arrows show the direction of laser polarisation and the size of the arrow reflects the pulse energy. The pre-pulse is shown in grey and the main pulse in black.

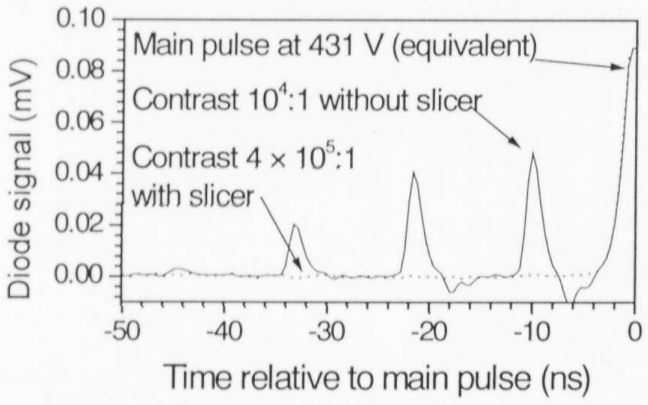


Figure 3.17. Pre-pulse level with and without the single pulse isolator ('slicer').

3.5.4 The single pulse isolator

It is important to ensure that the final laser pulse has no significant pre-pulse associated with it as this will interact with and modify the experimental target before the main laser pulse is incident on it. With final laser intensities ~10^{16} - 10^{17} Wcm^{-2}, a pre-pulse at the 10^{-4} level can cause ionisation. In order to remove any pre-pulse present on a nanosecond time-scale, a single pulse isolator (figure 3.16) was built at the output of the regenerative amplifier in early 1997. The isolator is essentially a Pockels cell followed by a polariser. The additional components associated with our isolator serve to reject any residual horizontally polarised light from the regenerative amplifier, control the laser energy and ensure the final polarisation is correct before the next stage of amplification. When the Pockels cell is driven to its half-wave voltage a laser pulse can pass through the isolator, otherwise it will be strongly attenuated. The timing of the high-voltage pulse is set to be as near as possible to the front of the main pulse without attenuating it at all. The polarisation of any pre-pulse is unchanged on passing through the Pockels cell and is rejected by the final polariser, while the polarisation of the main pulse is rotated 90° and passes straight through.

The laser pulse with and without the isolator is shown in figure 3.17. Without the isolator the pre-pulse is ~10^{-4} of the main pulse, using the isolator has reduced it to ~2.5 × 10^{-6}. The maximum final intensity of the pre-pulse is then only ~10^{11} Wcm^{-2}, which will not significantly ionise the gaseous targets typically used in experiments with this laser.

3.5.5 The multi-pass power amplifiers

After the pre-pulse is removed by the single pulse isolator, the laser pulse is amplified by a series of two multi-pass power amplifiers. The first amplifier is a double-pass pre-amplifier (figure 3.18), pumped by 180 mJ from the Continuum Surelite Nd:YAG laser which also pumps the regenerative amplifier. The pump pulse is focused by a 1 m focal length lens to a fluence of 2 Jcm^{-2} onto the 7.5 mm long, Brewster cut Ti:Sapphire crystal.

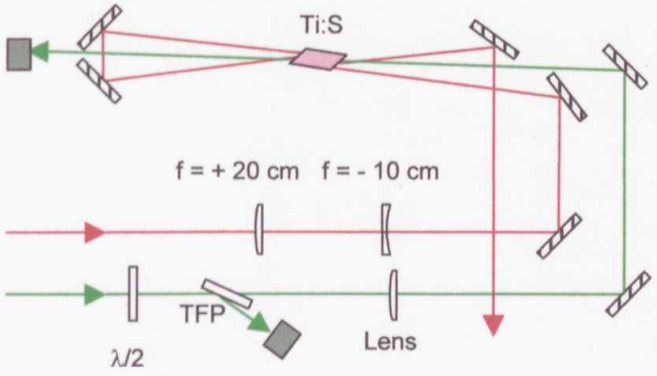


Figure 3.18. Ti:sapphire double-pass pre-amplifier.

The laser pulse is down-collimated to a diameter of 2 mm, before making two passes of the Ti:Sapphire crystal where it is amplified to 12 mJ, a gain of 6. The pulse is then magnified and collimated to a diameter of 6 mm and sent to the final stage of amplification. Prior to the addition of this amplifier stage (in January 1998), the laser pulse passed directly from the regenerative amplifier or single pulse isolator to the final amplifier. It entered the final stage of amplification with an energy of 2 mJ and a diameter of 6 mm.

The final amplifier is a multi-pass Ti:Sapphire power amplifier (figure 3.19). This amplifier uses angular multiplexing, whereby successive passes of the amplifier are at different angles and the beam follows a 'bow-tie' path. This ensures that the passes are spatially separated, but the overlap with the pump volume remains good. The laser pulse makes a total of five passes of the crystal. The crystal is 1 cm^3 of Ti:Sapphire, AR coated at both 780 nm and 532 nm and water-cooled. The crystal is pumped from both sides by 532 nm light from a frequency-doubled Q-switched Nd:YAG laser (BMI 503). The field distribution at the doubling crystal is imaged by a lens system onto the crystal. This provides spatially uniform 'top-hat' pump beams of about 7.5 mm diameter. The pump energy is ~200 mJ on each side of the crystal. Without the pre-amplifier, the laser energy is 60 mJ at the output (a gain of 30). With the pre-amplifier, the output energy is 100 mJ, a gain of 8.

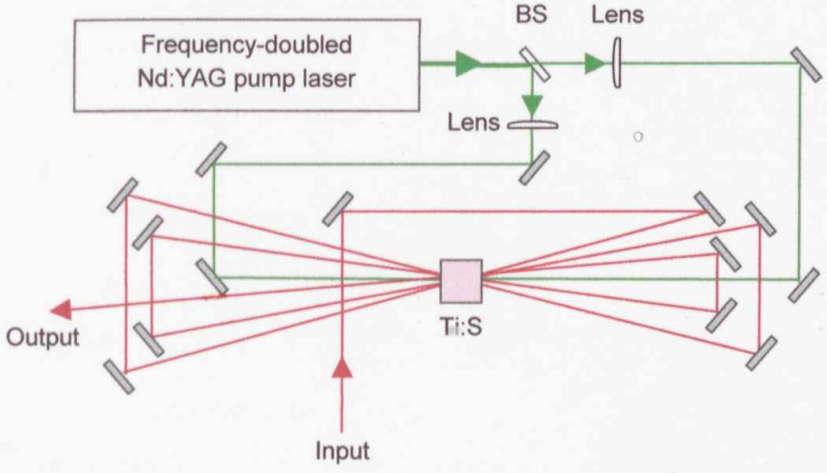


Figure 3.19 Ti:sapphire multi-pass amplifier.

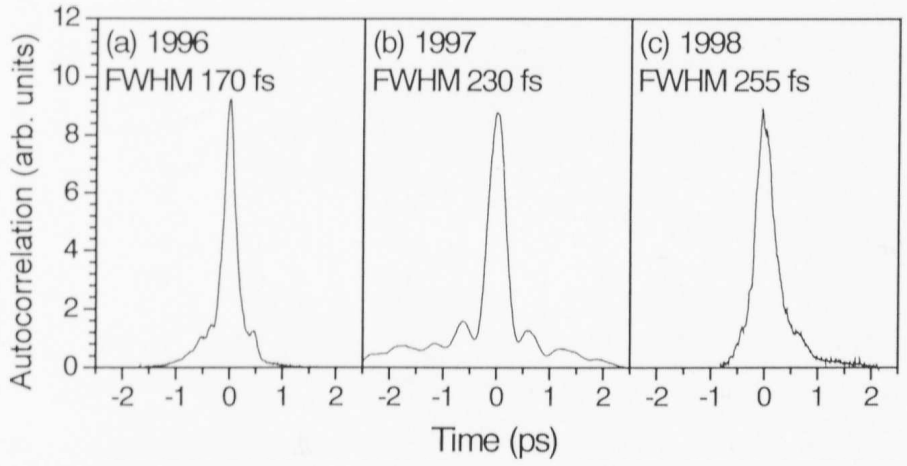


Figure 3.20. Autocorrelations of the amplified pulse at the exit of the laser for the three major sets of laser configurations. (a) 1996, (b) 1997, when the stretcher and compressor gratings were changed, and (c) 1998, when the compressor was completely re-aligned.

3.5.6 The compressor

After amplification, the beam is up-collimated and sent to the compressor, which consists of a pair of parallel gratings, as in figure 3.7. The compressor diagnostics are a single-shot auto-correlator to optimise the pulse shape and duration, and a far-field monitor which uses a microscope objective to image the focal spot.

The compressor was upgraded in early 1997. In the original configuration, the gratings were 11 × 4 cm, 2000 line/mm gold-coated holographic gratings, with a separation of ~75 cm. The grating size limited the $1/e^2$ beam diameter to 17 mm. A typical auto-correlation of the compressed pulse is shown in figure 3.20a. The pulse duration is 170 fs

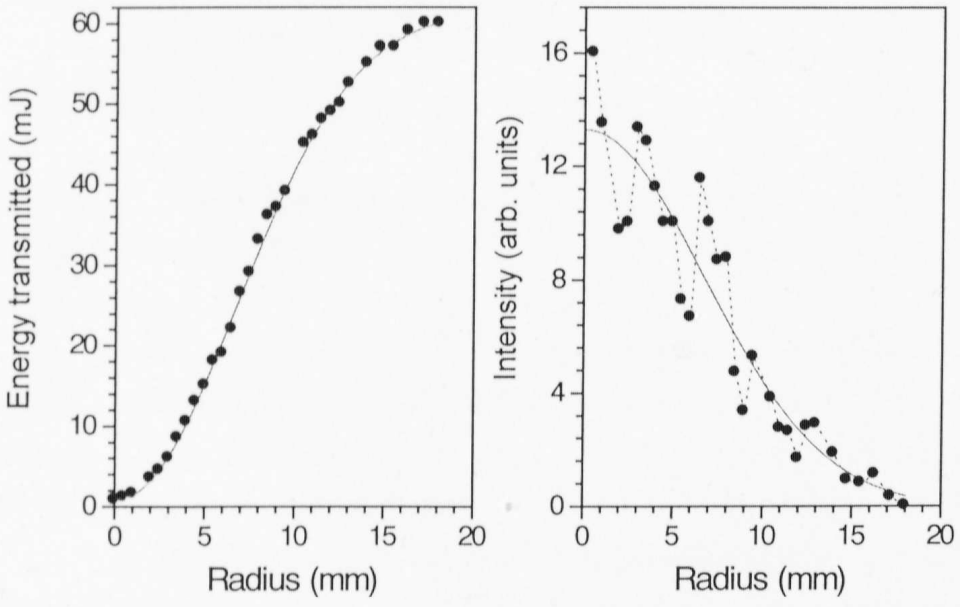


Figure 3.21. Beam profile at the entrance to the compressor, obtained through measurement of the energy transmitted through a variable radius aperture. The solid lines are Gaussian fits to the data. The $1/e^2$ radius is 13.4 ± 0.1 mm.(1997).

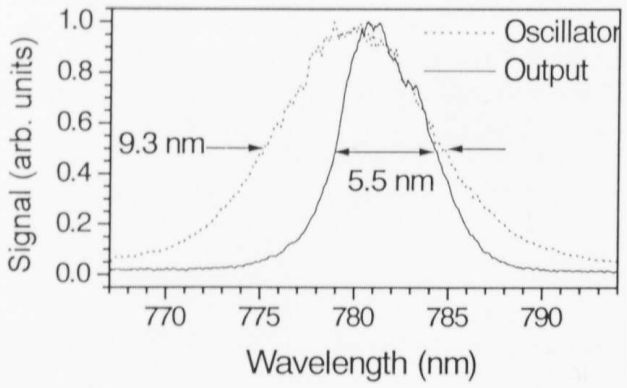


Figure 3.22. Laser spectrum measured after the oscillator, where the FWHM is 9.3 nm, and at the output of the system where the spectrum has narrowed to a 5.5 nm FWHM. (1998).

(assuming a $sech^2$ pulse-shape). This is longer than the original pulse due to higher-order phase terms picked up by the pulse on propagation through optics and amplifier crystals, and bandwidth-limiting elements such as dielectric coatings.

The gratings were replaced by 14 cm diameter, 1800 line/mm gratings, with a separation of ~120 cm. The telescope into the compressor was changed to give a ($1/e^2$) beam diameter of 26 mm (figure 3.21). Auto-correlations of the final pulse are shown in figure 3.20 b and c. The pulse duration is considerably longer with the new stretcher and compressor (up to 255 fs), due to aberrations in the stretcher which cause the spectrum to narrow in the regenerative amplifier. As a consequence, the central wavelength also shifts to 782 nm. This can be seen in figure 3.22, which compares the spectrum of the compressed pulse from the new stretcher-compressor with the oscillator spectrum. The compressor was completely realigned in early 1998, and the pedestal and wings visible on the 1997 auto-correlation were dramatically reduced.

The throughput of the compressor is ~50% for p-polarised pulses. The maximum pulse energy obtained is 30 mJ without and 45 mJ with the pre-amplifier.

3.5.7 Final output and focused intensity

The final output of the laser system in the three configurations used for the experiments described in this thesis is tabulated in Table 3.1.

The focused intensity achievable with the Ti:Sapphire laser system has been measured by examining ionisation rates in xenon or helium (figure 3.23a). The laser pulse was focused down into a vacuum chamber containing a static fill of the gas to a pressure of 10^{-6} mbar. The laser intensity is calculated from the over-the-barrier appearance intensities [Augst 1991] of the charge states. The error on the intensity obtained in this way is approximately a factor of two – smaller than the error in estimating the intensity from pulse shape and focal spot size.

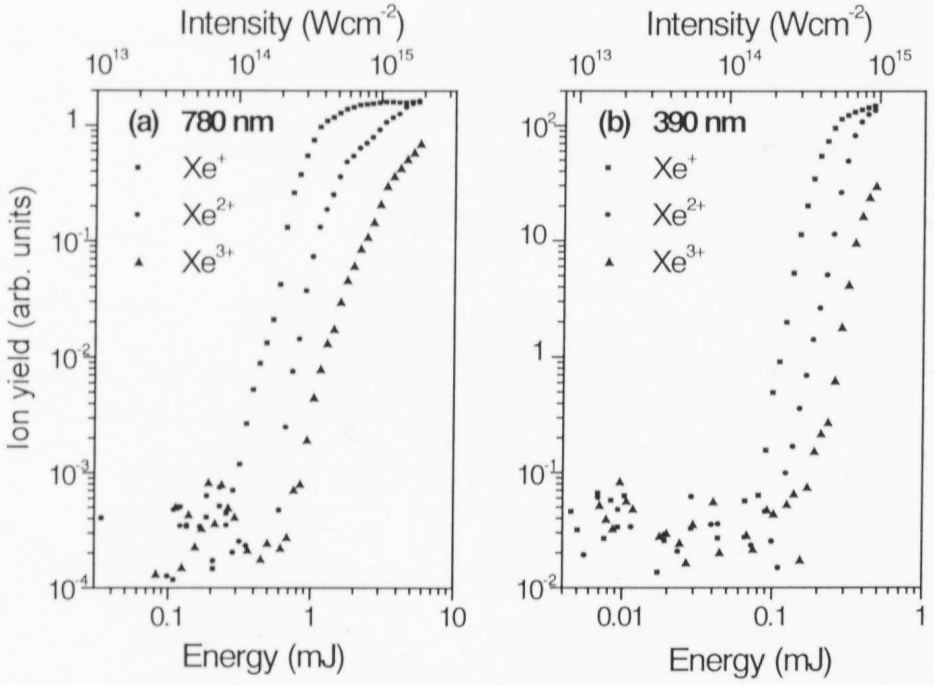


Figure 3.23. Measured ion yield of Xe^+, Xe^{2+} and Xe^{3+} as a function of laser energy at 780 nm (a) and 390 nm (b). The laser intensity calculated from over-the-barrier appearance intensities is shown on the top axis. (1998)

A 3 mm thick type 1 KDP crystal is used to frequency double the 780 nm laser pulse to 390 nm (blue). The highest conversion efficiency we measured was 6 mJ blue from 30 mJ IR, an efficiency of 20%. This conversion efficiency is lower than would be expected from an estimate based on the intensity we propagate and the pulse-length. This may be due to phase modulation of the fundamental from residual chirp on the pulse after compression, which can strongly reduce the conversion efficiency [Krylov 1995]. The focused intensity obtained in the blue has again been measured from ionisation rates (figure 3.23b).

A typical focal spot in the IR with a 19.3 cm focal length lens is shown in figure 3.24. The spot size is 12 × 18 μm, which is 3× times diffraction limited in the x-direction, and 5× diffraction limited along the y-axis.

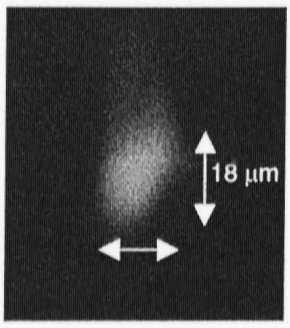


Figure 3.24. Typical IR focal spot with f = 19.3 cm lens (1997).

	1996	1997	1998
Stretcher/compressor grating ruling (lines/mm)	2000	1800	1800
Pre-amplifier	No	No	Yes
Single pulse isolator	No	Yes	Yes
Pulse-length (FWHM)	170 fs	230 fs	255 fs
Bandwidth (FWHM)	6.0 nm	5.5 nm	5.5 nm
Maximum energy	30 mJ	30 mJ	45 mJ
Shot-to-shot stability	±2 mJ at 12 mJ	±2 mJ at 12 mJ	±1.4 mJ at 45 mJ
Contrast (on a ns timescale)	10^{-4}	2.5×10^{-6}	2.5×10^{-6}
Pre-pulse	~0.1 at ± 450 fs	~0.2 at ± 600 fs	< 0.01
Pedestal	< 0.01	~0.1 over ~ 1 ps	< 0.01
Beam diameter ($1/e^2$)	17 mm	26.8 ± 0.2 mm	26.8 ± 0.2 mm
IR Focal spot ($1/e^2$)	10 μm × 9 μm (20 cm lens)	13 μm × 18 μm (19.3 cm lens)	65 μm × 12 μm (on target with 33.5 cm lens)
Focused intensity per mJ IR	6.7×10^{14} Wcm^{-2}	5.6×10^{14} Wcm^{-2}	3.3×10^{14} Wcm^{-2}
Max blue energy	6 mJ	3 mJ	3 mJ
Blue focal spot ($1/e^2$)	6 μm × 8 μm (20 cm lens)	(Not measured)	76 μm × 13 μm (on target with 32.3 cm lens)
Focused intensity per mJ blue	(Not measured) ~8×10^{15} Wcm^{-2}	6.3×10^{15} Wcm^{-2}	2.0×10^{15} Wcm^{-2}
Max focused intensity with 20 cm lens - IR	2×10^{16} Wcm^{-2}	1.7×10^{16} Wcm^{-2}	1.5×10^{16} Wcm^{-2} with 33.5 cm lens
Max focused intensity with 20 cm lens - blue	~5×10^{16} Wcm^{-2}	2×10^{16} Wcm^{-2}	6×10^{15} Wcm^{-2} with 32.3 cm lens

Table 3.2. Laser parameters in the three major sets of laser configurations.

The intensity calibrations obtained through measurements of over-the-barrier appearance energies in general agrees to within a factor of 2 – 3 with those obtained from the measurements of focal spot sizes and pulse lengths. The exception is the blue calibration from 1998, which is greater than a factor of 10 different. This may be explained by the second harmonic having a peculiar pulse-shape, as we had a surprisingly low second harmonic conversion efficiency at the time.

3.6 Conclusions

The use of chirped pulse amplification has been fundamental to the production of high power, ultrashort pulse laser systems. CPA was developed in response to the problems associated with amplifying high peak-power pulses - the main problem being self-focusing and optical breakdown caused by the optical Kerr effect. It is somehow appropriate that one of the most successful methods of generating ultrashort pulses, namely Kerr lens mode-locking, should rely on this same effect.

Terawatt, femtosecond laser systems have enabled major advances in the field of high-intensity laser-matter interactions. The phenomenally high intensities achieved by these systems have opened up a whole new regime for study. Both the development of systems capable of delivering even shorter pulses and even higher power and the study of the interactions of these pulses provide major theoretical and experimental challenges.

The Blackett Laboratory Laser Consortium Ti:Sapphire CPA laser system delivers 780 nm pulses at 10 Hz with energies up to 45 mJ and pulse-lengths in the region of 200 fs. The maximum power is ~0.2 TW and the laser can be focused to intensities in excess of 10^{16} Wcm^{-2}. The laser has been used extensively in studies of high-harmonic generation and molecular dissociation as well as for the cluster fragmentation studies described in this thesis.

Experimental apparatus and techniques

The mechanism of cluster formation in gas-jets is discussed in this chapter, together with Rayleigh scattering measurements which have allowed us to determine the mean cluster size in the interaction region. The experimental techniques and apparatus (in particular the time-of-flight spectrometer) and data analysis algorithms are introduced.

4.1 Cluster formation in gas-jets

In the experiments described in this thesis, clusters were formed during the adiabatic expansion of high-pressure gas from a pulsed gas-jet into a vacuum. The gas cools as it expands and atoms and molecules are able to form van der Waals bonded clusters. The degree of clustering in the gas-jet is a function of the gas species, the initial gas pressure and temperature and the geometry of the gas-jet nozzle. The mean sizes of Xe, Kr and Ar clusters formed in the gas-jet have been measured using Rayleigh scattering. The dependence of mean cluster size on gas-jet backing pressure, initial gas temperature and gas species has been examined. These studies have enabled us to more fully characterise the medium with which the laser interacts.

4.1.1 Determination of cluster size

It is extremely difficult to accurately measure or control the distribution of cluster sizes in a cluster beam. The non-availability of reliable techniques for selecting the sizes of large clusters means that almost all experiments on them (including those described in this thesis) rely on manipulating the average size of the distribution by changing the gas-jet backing pressure and temperature.

Time-of flight mass spectrometry has been used to measure cluster sizes [Hagena 1972], but the distributions obtained using this method can be strongly distorted, especially

for small clusters which tend to disintegrate before detection. Large clusters of more than ~ 10^3 atoms undergo multiple ionisation, but distortion of the size distribution due to fragmentation may be relatively minor [Gspann 1973, Karnbach 1993]. High-energy electron diffraction [Farges 1986] suffers because the diffraction peaks are smeared out by the broad distribution of cluster sizes. The cluster sizes have to be obtained by determining the cluster structure from the diffraction pattern and comparing these with calculated cluster structures. Several methods have been developed which involve crossing the cluster beam with a second molecular beam, or passing the cluster beam through a buffer gas, and measuring the angular scattering [Buck 1996, DeMartino 1993, Lewerenz 1993] or change in cluster velocity [Cuvellier 1991]. All of these techniques involve specialised equipment and complicated analysis, so we turn to Rayleigh scattering [Bell 1993] as a simple method that can be carried out without major additions to our experimental apparatus. Mie scattering techniques are not applicable here as the clusters we are interested in have a radius of only a few tens of angstroms, much smaller then the wavelength of light.

4.1.1.1 Hagena parameter

The extent of atomic clustering in a gas-jet can be estimated using the principle of 'corresponding jets' [Hagena 1972]. This states that expansions which have the same value of an empirical scaling parameter Γ^* (the 'Hagena parameter') are expected to exhibit the same degree of clustering, i.e. have the same fraction of atoms condensed into clusters and the same mean cluster size. The Hagena parameter is given by,

$$\Gamma^* = k \frac{(d/\tan\alpha)^{0.85} p_o}{T_o^{2.29}}, \tag{4.1}$$

where d is the diameter of the nozzle (in μm), α the jet expansion half-angle, p_o the gas-jet backing pressure (in mbar), T_o the initial gas temperature (in K) and k the condensation parameter (an empirical constant that depends on the gas). The value of k is 5554 for Xe, 2980 for Kr, 1646 for Ar and 185 for Ne [Karnbach 1993].

Published scalings of cluster size with Hagena parameter indicate that when $\Gamma^* <$ 300, there is almost no clustering in the gas-jet, with less than ~ 2% of atoms having condensed into small clusters (predominantly dimers and trimers) [Wormer 1989, Karnbach 1993]. In the region where $300 < \Gamma^* < 1800$, the cluster size scales as with mean number of atoms per cluster, N_C, as [Buck 1996, Karnbach 1993]

$$N_C \sim \Gamma^{*(1.64 \text{ or } 1.85)}. \tag{4.2}$$

The fraction of clusters that have condensed into atoms rapidly increases from 5% to 30% as Γ^* goes from 400 to 600, and then rises steadily until nearly all the atoms have condensed into clusters at $\Gamma^* \sim 1800$ [Wormer 1989]. When $\Gamma^* > 1800$, we are in the regime

of "massive condensation" in the gas-jet, where nearly all the atoms have condensed into large clusters and the mean cluster size is > 100 atoms per cluster. In the massive condensation regime, the cluster size scaling varies more steeply with Γ^* as [Farges 1986, Hagena 1991, Karnbach 1993]

$$N_C \sim \Gamma^{*(1.95,\,2.35\text{ or }2.93)}. \tag{4.3}$$

Three independent sets of measurements all point to the mean cluster size being ~ 100 when $\Gamma^* \sim 1800$ [Hagena 1991, Karnbach 1993 and Buck 1996].

Measurements of the size distribution of large noble gas [Lewerenz 1993 and Karnbach 1993] and nitrogen [Gspann 1982] clusters suggest that the cluster sizes exhibit a log-normal distribution with a full-width at half maximum approximately equal to the mean cluster size.

4.1.2 Rayleigh scattering

We can estimate the size of the clusters produced in the expansion by measuring the Rayleigh scattered signal at 90°. The cross section for classical Rayleigh scattering is given by [Kerker 1969]

$$\frac{d\sigma}{d\Omega} = 2\pi \frac{R_C^6}{\lambda^4}\left(\frac{n^2-1}{n^2+2}\right), \tag{4.4}$$

where σ is the cross-section, Ω the solid angle that the light is scattered into, R_C the cluster radius, λ the wavelength of the scattered light and n the refractive index of the medium. This expression is valid only when the radius of the scatterers is $< 0.05\,\lambda$, which corresponds to a cluster of ~ 10^6 xenon atoms with 532 nm light.

The scattered signal, S_{RS}, is proportional to the product of the Rayleigh scattering cross-section of the cluster and the density of clusters, n_C. The cross-section at a given wavelength scales as

$$S_{RS} \sim n_C R_C^6 . \tag{4.5}$$

The total number density of monomers n_0 is given by

$$n_0 = \sum_{\text{all cluster sizes}} n_C N_C \tag{4.6}$$

where N_C is the number of atoms per cluster. For self-similar distributions (where the width of the distribution is proportional to the mean cluster size) it can be shown that

$$S_{RS} \sim n_0 \tilde{R}_C^3 \sim n_0 \tilde{N}_C \tag{4.7}$$

where $\tilde{R}_C$ is the mean cluster radius. This can be demonstrated analytically for the delta-function distribution. If we assume that all the atoms have condensed into clusters of the

same size, it then follows that the number density of clusters will be given by the monomer density before clustering divided by the number of atoms per cluster so

$$n_C \sim n_0 / N_C \,, \tag{4.8}$$

Substituting Eq. (4.8) into Eq. (4.5)and using the fact that $R_C \sim (N_C)^{1/3}$ we again obtain Eq. (4.7). The fact that the scatter signal depends only on mean cluster size and number of monomers for a self-similar distribution implies that we can obtain no information about the width or shape of a self-similar cluster size distribution using this technique. We are also unable to distinguish a change in mean cluster size from a change in condensed fraction, so this technique is only valid in regions of parameter space where the condensed fraction is constant.

If the monomer density before clustering is proportional to p_0/T_0, we can scale the Rayleigh scatter signal by this factor to account for the change in the number of monomers ejected by the gas-jet and get

$$\tilde{N}_C \sim \frac{T_0}{p_0} S_{RS} \,. \tag{4.9}$$

Recent work on the characterisation of cryogenically cooled gas-jets of the type used in this experiment has indicated that the scaling of the number of monomers ejected by the gas-jet with temperature deviates from $1/T_0$ at high backing pressures as the initial gas temperature drops towards the liquefaction point [Smith 1998] and a few extremely large droplets are formed in the jet. The signature of this is a sudden and very rapid increase in the Rayleigh scatter signal.

We expect that when large clusters are present in the gas-jet, the scaling of scatter signal with backing pressure and temperature will vary as (from eqs. (4.3) and (4.9))

$$S_{RS} \sim \frac{p_0^{2.95-3.93}}{T_0^{5.47-7.71}} \,. \tag{4.10}$$

Observation of a sudden change in scaling of the scatter signal corresponding to the onset of massive condensation in the cluster beam (where the mean cluster size is ~100 atoms/cluster) can establish a fixed point in the cluster size scaling. Non-observation of this change in scaling at least allows us to fix a minimum size for the clusters produced.

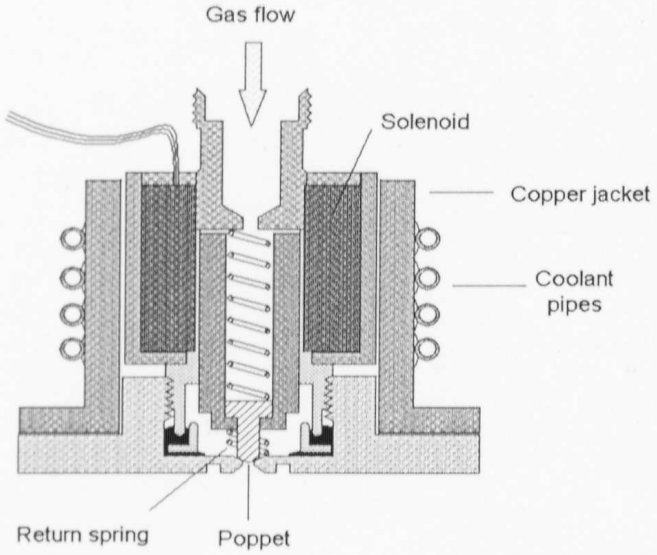


Figure 4.1. Gas-jet used to produce clusters. The jet body is a General valve series 99 solenoid pulsed valve with a 500 μm diameter sonic nozzle. It has been modified for use at cryogenic temperatures by the addition of a copper jacket, round which pass coolant pipes. (RAS).

4.1.3 Experimental apparatus

The gas-jet used to produce the clusters in this experiment was a General Valve Series 99 solenoid pulsed valve sonic gas-jet with a 500 μm diameter nozzle and jet expansion half-angle of 45° (figure 4.1). The gas-jet was modified to allow its operation down to ~ 80 K by wrapping the reservoir in a copper jacket around which passed cooling pipes [Smith 1998]. Nitrogen gas was forced under pressure through a separate heat-exchanger cooled with liquid nitrogen and then through the cooling pipes. By varying the flow-rate we were able to control the temperature of the gas in the reservoir to a precision of ~ ± 2 K. The gas-jet was run with an opening time of 400 μs and a repetition rate which varied from 10 Hz to 0.2 Hz. The repetition rate was determined by the need to ensure that the gas in the reservoir cooled to the jacket temperature and that the vacuum returned to better than ~10^{-3} mbar between shots.

Vertically polarised 532 nm light from a frequency-doubled Nd:YAG laser (86 μJ in a 10 ns pulse) was focused by a 30 cm focal length (*f*/30) lens into the vacuum chamber 1.5 mm below the gas-jet nozzle (Fig. 4.2). The 90° scattered light from this region was imaged by an f = 10 cm lens and detected by a photo-multiplier. The photo-multiplier was fitted with a narrow-band, 532 nm interference filter and a small aperture to ensure that only scattered light from the interaction region was detected. The scattered light was found to be highly vertically polarised, consistent with Rayleigh scattering. The interaction region was also imaged by a CCD camera to monitor the position of the interaction region relative to the gas-jet nozzle and ensure that there was no laser-induced breakdown of the gas. The relative timing of the laser pulse and gas-jet trigger was adjusted to optimise the scatter signal. The

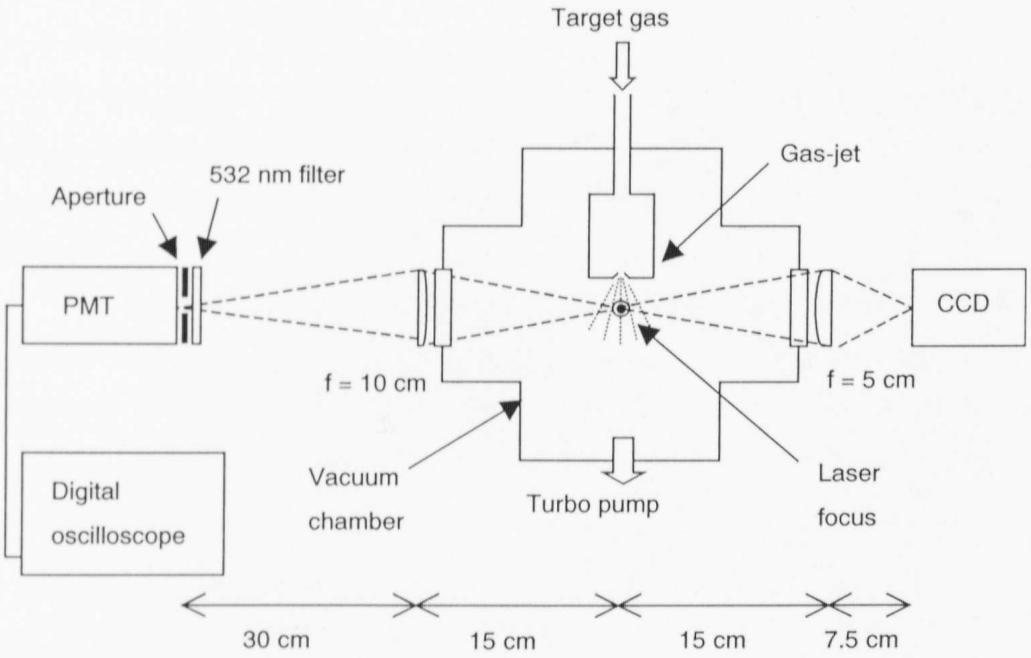


Figure 4.2. Experimental set-up to observe 90° scatter. The laser pulse (86 μJ in 10 ns at 532 nm) is focused into the vacuum chamber ~ 1.5 mm below the nozzle of the gas-jet. The direction of laser propagation is out of the page. A photomultiplier tube (PMT) connected to a digital oscilloscope and a CCD camera image the interaction region.

background level was obtained by subtracting the signal when the gas-jet was fired with no gas in it. Neutral density filters placed in front of the photo-multiplier allowed us to extend our dynamic range for linear detection to ~ 3 orders of magnitude.

4.1.4 Results

We have examined the scaling of the Rayleigh scatter signal with gas temperature and gas-jet backing pressure in xenon, krypton and helium (fig. 4.3). We were not able to unambiguously observe the change in scaling of the scatter signal corresponding to the onset of massive condensation.

The variation of scatter signal with gas-jet backing pressure for xenon at temperatures of 300 K, 250 K and 200 K is shown in fig. 4.3a. The scatter signal scales as p^b, where b is ~ 3.5 to 4.0, for pressures above ~ 1.0 bar at 300K, 0.8 bar at 250 K and 0.6 bar at 200K. The consistency of these pressure scalings with equation 4.10 indicates that

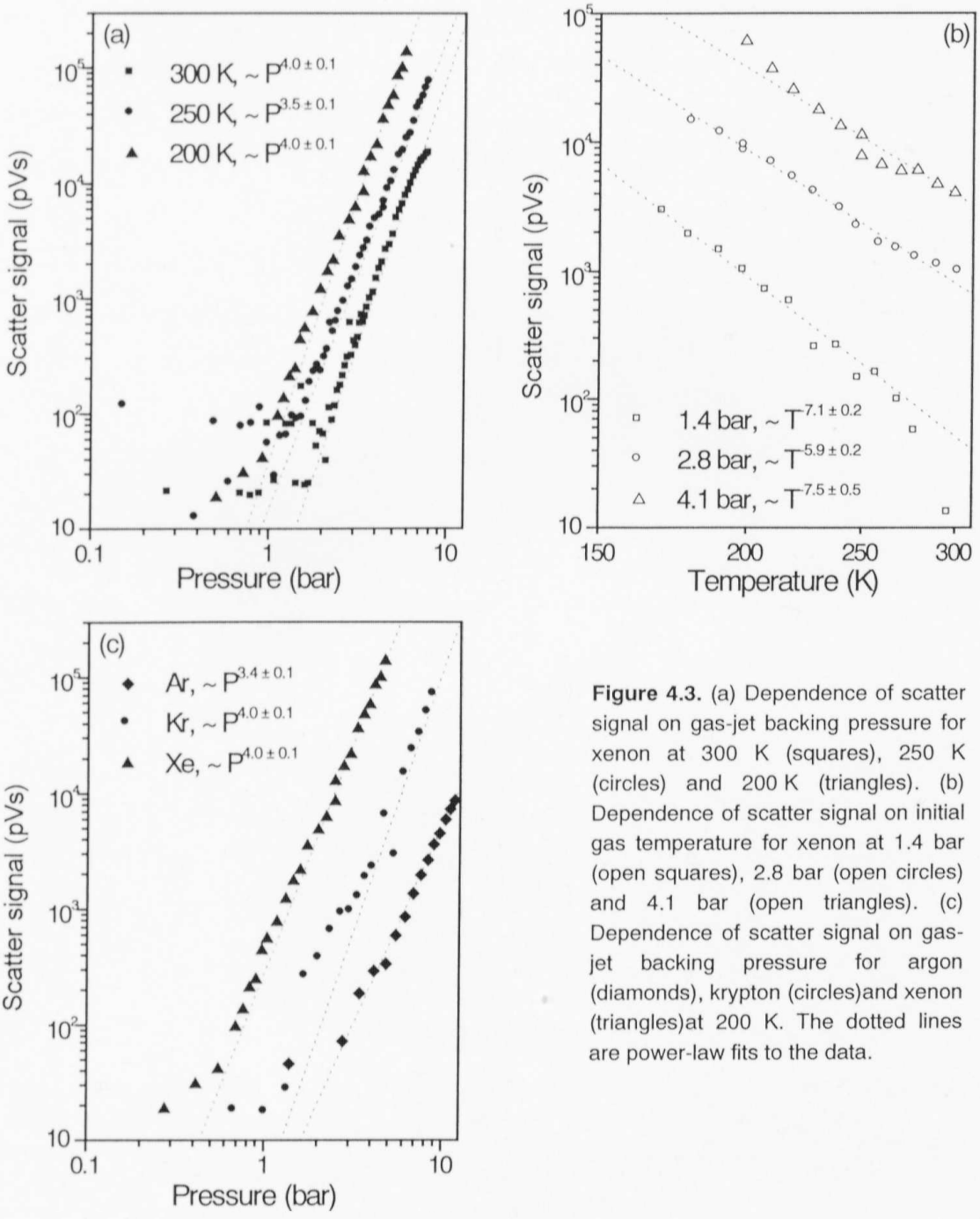


Figure 4.3. (a) Dependence of scatter signal on gas-jet backing pressure for xenon at 300 K (squares), 250 K (circles) and 200 K (triangles). (b) Dependence of scatter signal on initial gas temperature for xenon at 1.4 bar (open squares), 2.8 bar (open circles) and 4.1 bar (open triangles). (c) Dependence of scatter signal on gas-jet backing pressure for argon (diamonds), krypton (circles)and xenon (triangles)at 200 K. The dotted lines are power-law fits to the data.

large clusters of more than ~100 atoms are present in the gas-jet in the temperature and pressure ranges where the data can be fitted by a power law.

Fig. 4.3b shows the dependence of the scatter signal on initial gas temperature for xenon with gas-jet backing pressures of 1.4, 2.8 and 4.1 bar over the temperature range from 300 K to 170 K. The scatter signal varies with temperature as T^b where b is ~ –6 to –7 (again, this is consistent with eq 4.10). At 4.1 bar the scatter signal increases rapidly below ~ 220 K, as a few much larger droplets start to form in the jet.

The scalings in xenon have also been compared with other gases, and the scatter signal as a function of pressure for xenon, krypton and argon at 200 K is shown in Fig. 4.3c. Large clusters are present in the argon jet at pressures above ~ 2.8 bar and in krypton from ~ 1.7 bar. The scatter signal scales in Ar as $p^{3.4 \pm 0.1}$ and in Kr as $p^{4.0 \pm 0.1}$ (as in eq 4.10).

We can obtain scalings of N_C with Γ^* for the xenon data, as shown in Fig. 4.4. The scatter signals have been multiplied by T_0/p_0 to normalise them to the same monomer density ejected by the gas jet (Eq. 4.9). The six separate scans overlap which confirms both our assumption that the monomer density $\sim p_0/T_0$ and that the Hagena parameter is a useful way of characterising the degree of clustering in the jet. From this we obtain a scaling of cluster size with Hagena parameter of $N_C \sim \Gamma^{*2.40 \pm 0.09}$. This is consistent with previous measurements of the variation of Γ^* with mean cluster size (eq. 4.3).

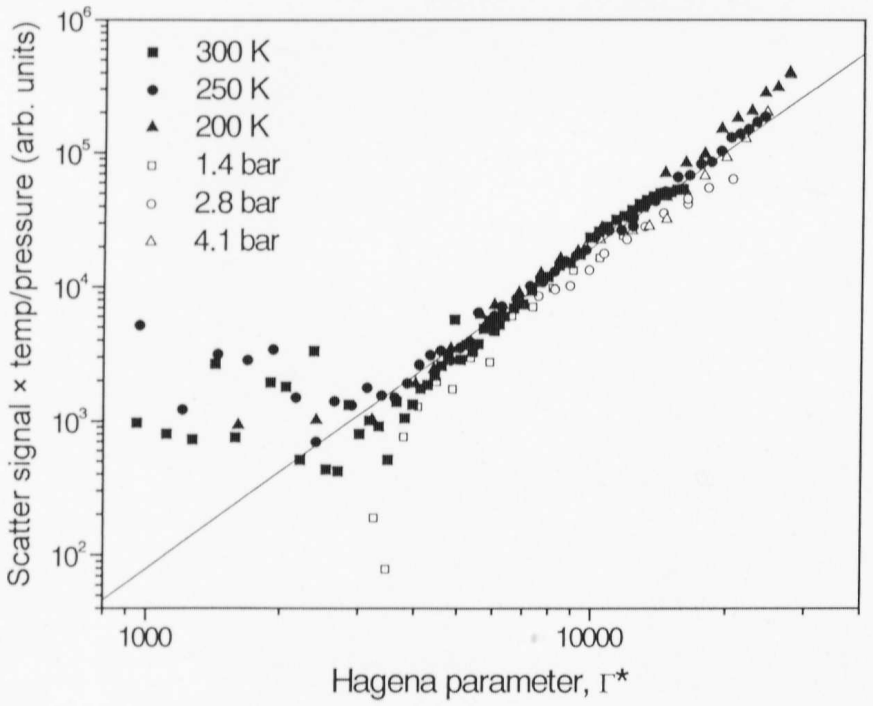


Figure 4.4. Dependence of scatter signal (multiplied by *T/p* to account for the variation in the number of monomers) on hagena parameter. The data points are taken from temperature scans at 1.4 bar (open squares), 2.8 bar (filled circles) and 4.1 bar (filled triangles) as in Fig. 4.3b and pressure scans at 300 K (filled squares), 250 K (filled circles) and 200 K (filled triangles) as in Fig. 4.3a. The line is a power-law fit to the experimental data and is proportional to $\Gamma^{*(2.40 \pm 0.09)}$.

4.1.5 Cluster sizes

The estimated cluster sizes for Xe, Kr and Ar as a function of gas-jet temperature and backing pressure are shown in table 4.1 below. The scalings of relative cluster sizes with temperature, backing pressure and gas have been calculated from the Hagena parameter assuming that $N_C \sim \Gamma^{*2.40}$. The fixed point on which these scalings are based is 100-atom clusters with a Hagena parameter of ~ 1800 (consistent with the scalings measured by Hagena [1991], Buck [1996] and Karnbach [1993]). Large clusters are observed in the gas-jet at higher values of Γ^* than this, and we observe no signal above the noise at lower values of Γ^*. This sets a lower limit on the cluster size but as we were unable to observe a change in scaling of the scatter signal corresponding to the onset of massive condensation in the jet, we cannot set a precise upper limit. Our cluster size calibration is, therefore,

$$N_C \sim 25\left(\frac{\Gamma^*}{1000}\right)^{2.40} \tag{4.11}$$

The cluster radii were calculated from the number of atoms per cluster by assuming that the clusters have the same density as the bulk solid. (Briant and Burton [1975] found that the nearest neighbour distances between atoms in argon clusters were within 1% of the bulk value for clusters larger than ~ 10 atoms.) The error on the estimate of cluster size is probably a factor of two, which corresponds to an error of ~ 25% on the radius.

Table 4.1. Estimated cluster sizes for Xe, Kr, and Ar over the range of gas-jet backing pressures and temperatures investigated, calculated from eqs 4.1 and 4. 11.

Xenon						
Temp(K)	300			200		
Pressure (bar)	Γ^*	N_C	R_C (Å)	Γ^*	N_C	R_C (Å)
0.5	1200	40	8	2900	300	17
1	2300	200	14	5900	1800	30
2	4600	1000	24	11800	9300	51
3	7000	2600	34	17600	25000	71
4	9300	5300	43	23500	49000	90
5	11600	9000	51	29400	84000	107
6	14000	14000	59	35300	130000	124
8	19000	28000	74	47000	260000	156
10	23000	47000	89	58800	440000	186
12	28000	74000	103	70600	680000	216

Krypton						
Temp(K)	300			200		
Pressure (bar)	Γ^*	N_C	R_C (Å)	Γ^*	N_C	R_C (Å)
0.5	600	8	4	1600	70	9
1	1200	40	8	3200	400	16
2	2500	200	14	6300	2100	29
3	3700	600	19	9500	5500	39
4	5000	1200	24	12600	11000	50
5	6200	2000	28	15800	18800	59
6	7500	3100	33	18900	29000	69
8	10000	6200	41	25200	57900	86
10	12000	10700	49	32000	99000	103
12	15000	17000	57	38000	150000	120

Argon						
Temp(K)	300			200		
Pressure (bar)	Γ^*	N_C	R_C (Å)	Γ^*	N_C	R_C (Å)
0.5	300	2	3	900	20	6
1	700	10	5	1700	90	10
2	1400	50	8	3500	500	17
3	2100	140	11	5200	1300	23
4	2800	300	14	7000	2600	29
5	3400	500	17	8700	4500	35
6	4100	800	19	10000	7000	41
8	5500	1500	24	14000	13900	51
10	6900	2600	29	17000	24000	61
12	8300	4000	34	21000	37000	71

4.2 Experimental techniques and apparatus

4.2.1 Time-of flight spectrometer

In our experiment (illustrated in figure 4.5), a beam of atomic clusters, produced in the expansion of a high-pressure gas into vacuum, is irradiated by a focused, high-intensity, femtosecond laser beam. The electrons and ions expelled from the clusters with velocities perpendicular to both the cluster beam and the laser beam propagated along a time-of-flight (TOF) tube and were detected by a micro-channel plate detector (MCP). The ion energies were then determined by measurement of their flight time; the electron energies were found by measuring the decrease in the MCP signal as a retarding voltage was applied to a grid placed between the focus and the MCP.

The clusters produced by the gas jet were collimated into a low density cluster beam for the time of flight experiments. A skimmer with an aperture of 0.5 mm and 50° cone located 15 cm below the gas jet was used to collimate the cluster beam and separate the chamber containing the gas-jet from the interaction region and TOF spectrometer. This produced a low density cluster beam which intercepted the laser beam at the focus. The density at the focus was estimated to be 10^{13} atoms cm^{-3} per bar of gas-jet backing pressure, so with a 20 μm diameter focal spot the laser interacts with ~ 10^4 100-atom clusters at 1 bar and ~ 10^3 7000-atom clusters at 6 bar.

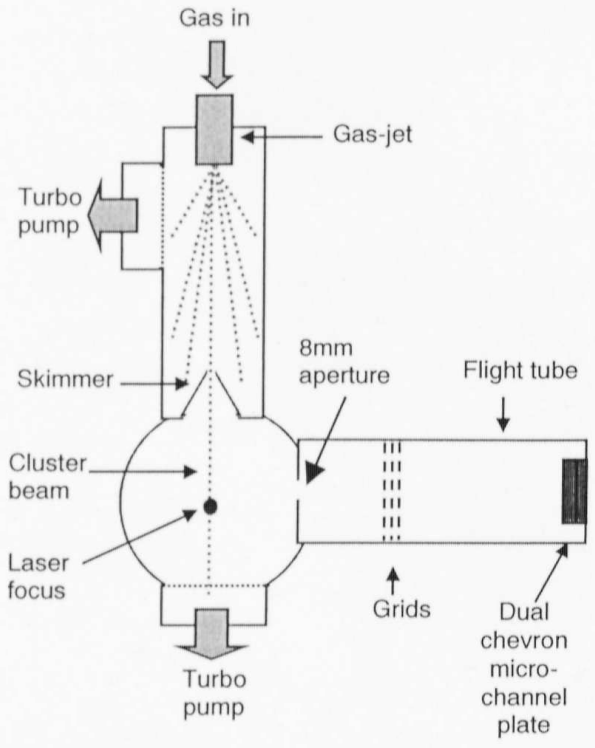


Figure 4.5. Experimental configuration for measuring ion and electron energies.

The two chambers were differentially pumped to enable cluster formation in the gas-jet while ensuring that the vacuum in the interaction region remained sufficiently low. The base pressure in the main chamber was ~ 10^{-7} mbar. The repetition rate of the gas-jet was determined by the pump-rate of the vacuum chamber, and was set to ensure the base pressure in the main chamber returned to ~ 10^{-7} mbar between shots. A repetition rate of 1 Hz when the gas-jet was backed with 6 bar was typical. The opening time of the gas-jet was set at

the minimum for which clusters were reliably produced. The opening time used varied between 400 μs and 2000 μs, as it is a sensitive function of the degree of tightening of the jet and wear on the poppet.

The timing electronics used to trigger the oscilloscope (Tektronics TDS 500 or 600 series) monitoring the MCP are shown in figure 4.6, and figure 4.7 shows the sequence of trigger events produced for a repetition rate of ~1 Hz. Both the gas-jet and the oscilloscope require a trigger at an integer multiple of the laser repetition period, and the oscilloscope trigger must be optically stable. The gas-jet needs to be fired ~1 ms before the laser pulse reaches the interaction region to ensure that the laser pulse coincides with the arrival of clusters from the gas-jet. Achieving this required a complex sequence of delays and logic triggers. The delay generator (SRS DG 535) for the experiment was triggered at T_0 from the laser master delay generator. The maximum output trigger rate was deliberately slowed by setting T_B to be roughly equal to the required interval between gas-jet shots. The delay generator was then set to produce a 40 μs wide pulse centred on the laser pulse after the trigger. The oscilloscope used a logic trigger on this pulse AND a fast optical trigger from a diode. The gas-jet timing T_A was then set by looking for electron and ion signal at the MCP, as signal was only observed when the laser pulse coincided to within ~ 0.1 ms of the centre

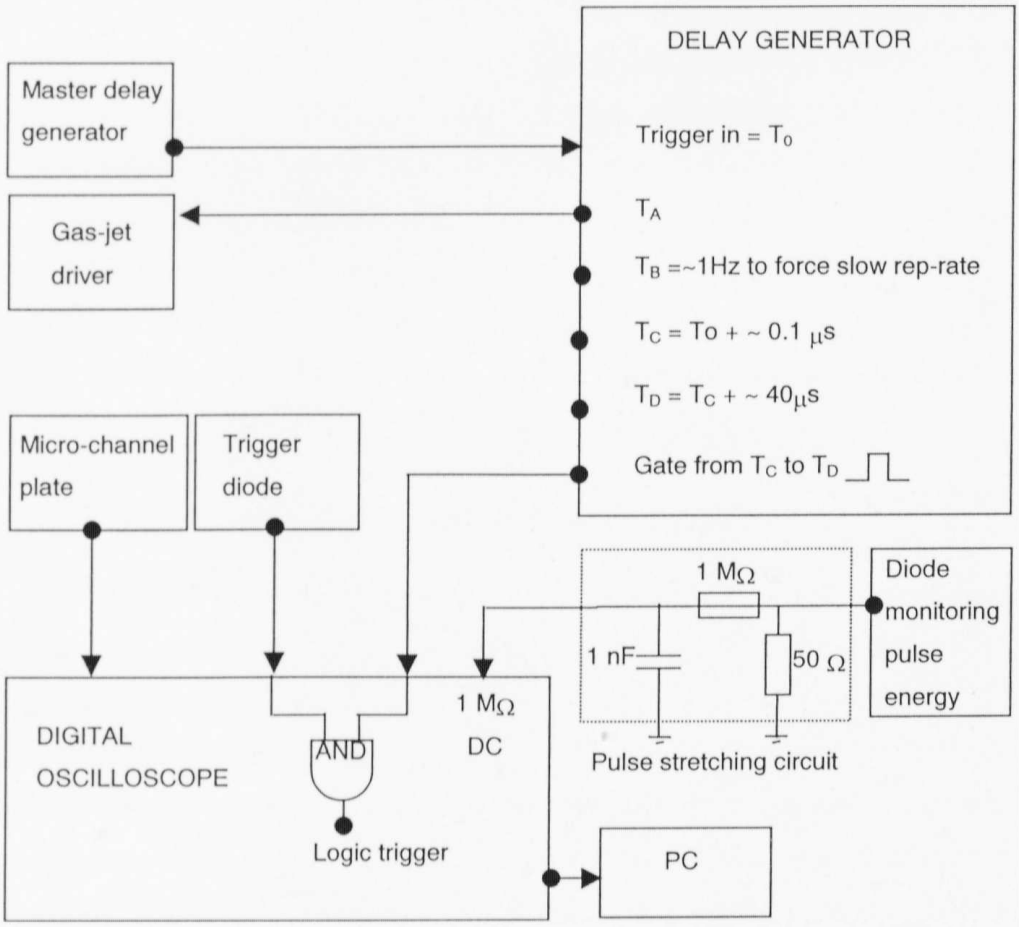


Figure 4.6. Timing and acquisition electronics.

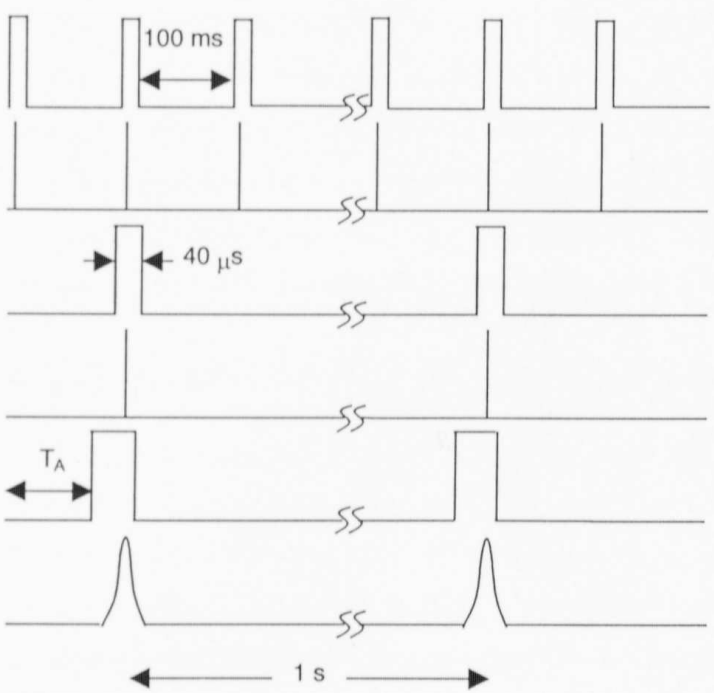


Figure 4.7. Sequence of trigger events required to ensure cluster beam is intercepted by laser pulse.

of the pulse of clusters from the gas-jet.

To measure the laser energy on each shot, we used the output of a diode at the exit of the target chamber. The diode signal was stretched with the pulse-stretching circuit shown in fig 4.6 to a width of a few μs so that it could be resolved on the same time-base as that used by the oscilloscope for the ion signal. The diode was calibrated against a power meter (Molectron EPM 1000), and the integrated signal was found to be a linear function of pulse energy over ~ 3 orders of magnitude. We rejected laser pulses with energies outside a required energy range only during electron energy measurements and studies of the intensity dependence of the interaction. Tight energy binning was not found to be critical, due to the good shot-to-shot energy stability of the laser (see table 3.2) and the very slowly varying dependence of the explosion dynamics on laser intensity (§5.3).

4.2.2 Measurement of electron energies

The electrons emitted in the interaction were detected by a two-stage chevron micro-channel plate (MCP) with a 14 mm diameter active area placed at the end of a 17 cm flight tube, oriented perpendicular to both the cluster beam and the laser beam. The area subtended by the MCP detector limited the detection cone angle to 0.021 sr. Electrons ejected outside this solid angle were not detected. This is in contrast to magnetic bottle electron spectrometers which can collect electrons emitted into 2π sr. Two grids (spaced 3 mm apart) were placed immediately behind the entrance to the flight tube. The first grid was charged to a voltage Φ and the second was grounded, introducing a potential barrier to

electrons with energy less than $e\Phi$. The front plate of the MCP was grounded and the back held at +2 kV. The total gain of the MCP was ~ 10^6. The MCP output was capacitively coupled to the digital oscilloscope and fast gated integrators, which were interfaced with a PC. The electron signal was measured as a function of retarding voltage, smoothed with a 3-point adjacent averaging routine, and differentiated to give the electron energy spectrum. Each data point is the average of 50 shots, taken within a ± 10% laser energy bin.

4.2.3 Measurement of ion energies and charge states

The ion energies were determined by measuring their flight time in the drift tube, which was extended to 38 cm or 80 cm for these measurements. The detection solid angle for these experiments was 4.3×10^{-3} sr or 1.0×10^{-3} sr respectively. The front plate of the MCP was held at –2 kV, the back plate at –100 V and the collection anode at earth. A grounded metal grid placed ~2 mm before the MCP ensured that the flight tube was field free. The signal was again processed by a digital oscilloscope (with the bandwidth limited to 20 MHz) interfaced with a PC.

A typical time-of-flight spectrum (which represents the average of ~1000 laser shots) is shown in figure 4.8. The fast peak a few nanoseconds after the trigger is due to electrons with energies above 2 keV, while the broad signal extending from ~0.5 ms is due to ions. The TOF trace yields the ion distribution function, $f(t)dt$. To retrieve the energy distribution function, $f(E)dE$, the number of ions in each time bin was divided by dE/dt (which is $m_i l^2 t^{-3}$, where m_i is the ion mass, l the length of the flight tube and t the flight time). We use the same algorithm to analyse each time-of-flight trace, from which we obtain the ion energy spectrum and the mean and maximum ion energies. The maximum ion energy E_{max} is found by integrating the time-of-flight spectrum and fitting a straight line to the noise between the electron peak and ion peak. The point where the signal starts to increase above the noise level defines the shortest ion flight time and maximum energy. The mean ion energy is defined as

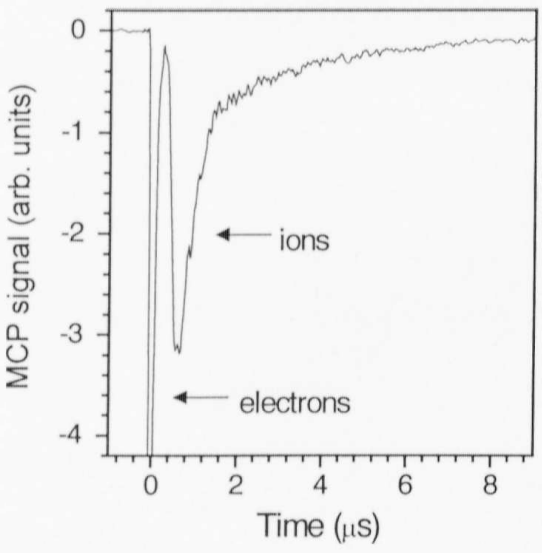


Figure 4.8. (a)Time-of-flight spectrum from 4700-atom xenon clusters (backing pressure 5 bar) irradiated by a peak intensity of 2 x 10^{16} Wcm^{-2}. The 38cm flight tube was field-free, but electrons with energy <2 keV are not detected as the front plate of the MCP is charged to +2 kV.

$$\overline{E} = \frac{\int_{E_{min}}^{E_{max}} Ef(E)dE}{\int_{E_{min}}^{E_{max}} f(E)dE} \tag{4.12}$$

where E_{min} is set to be 1 keV (we cannot set E_{min} to be 0 keV as this would require an infinitely long flight-time). Using this value of E_{min} results in an overestimate of the mean ion energy by ~ 15% (estimated by calculating $\overline{E}$ as a function of E_{min} and extrapolating to $E_{min} = 0$).

We were able to measure the charge state distribution of the ions as a function of their kinetic energy by varying the voltage on three metal grids, spaced ~3 mm apart, placed along the flight tube roughly one-third of the distance from the laser focus. Charging the middle grid to a potential Φ while keeping the front and back grids at earth introduced a barrier to ions with energy less than $Ze\Phi$ (where Z is the charge on the ion) without significantly altering the flight time of higher energy ions. The number of ions of a given energy, $E \pm \Delta E$ ($\Delta E = 20\%$), was calculated for each value of the retarding potential, Φ. This gives the number of ions with charge Z greater than $(E \pm \Delta E)/\Phi$. This was smoothed with a three-point adjacent averaging routine and then differentiated to give the number of ions in each charge state with energy $E \pm \Delta E$.

4.2.4 Microchannel plate response

We have measured the response of the microchannel plate as a function of ion arrival time by analysing the pulse height distributions as a function of arrival time. Fig 4.9 shows the ion time-of-flight trace from a single laser shot. The sharp peaks are individual ion hits. The inset graph is an enlarged section of the trace, showing that the individual ion

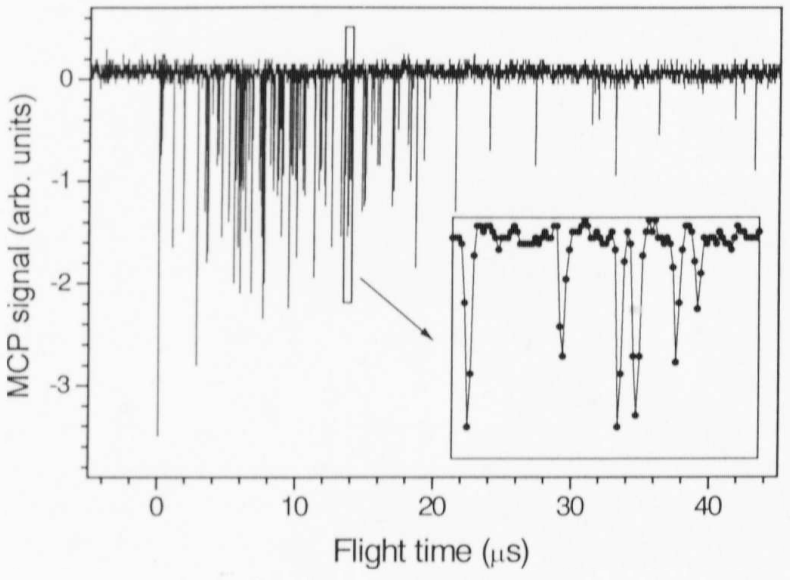


Figure 4.9. Single shot of a time-of-flight trace used to compile data for pulse height analysis. The inset graph is enlarged to show that there are several samples in every ion hit.

hits are resolvable. The distribution of pulse heights from ~ 2500 laser shots, together with the mean pulse height, is shown in figure 4.10 as a function of ion arrival time. The algorithm used to analyse the data searches for peaks by finding the maximum height of the signal each time it rises above a fixed noise level. The noise level was set by examining the distribution of noise peaks in the signal-free region of the oscilloscope trace before the trigger. For this dataset, it was fixed at 6 units. Over most of the energy spectrum the MCP response is reasonably flat, varying from 20 units for flight times longer than 25 μs (150 eV) up to 40 units at 1 μs (100 keV). The response appears to drop sharply from its peak at ~ 1μs down to only 10 units at 300 ns (1 MeV) but there are very few ion hits in this energy region and the noise level may be slightly higher here too, so it is possibly an artefact of our pulse-height analysis routine. The routine could be improved by using traces recorded with no gas-jet to set the noise levels. To enable us to quantify the effect of the variation of MCP response with flight time, we have compared the ion time-of-flight spectra (fig 4.11a) and energy spectra (fig 4.11b) obtained by simply averaging over the time-of-flight traces (blue lines) and by counting the number of ion hits within a 100 ns time bin (red lines). The spectra obtained using the two methods look very similar. The mean energies calculated in each case were 8.2 keV from averaging and 7.7 keV from pulse-counting – so ignoring the variation in MCP response results in an overestimate of the mean energy of only 6%.

Because we use a grounded metal grid ~ 2 mm in front of the MCP, the front of which is charged to –2 kV, the ions experience some charge-dependent acceleration and gain an additional energy of $2Z$ keV before reaching the detector. Their flight times are not

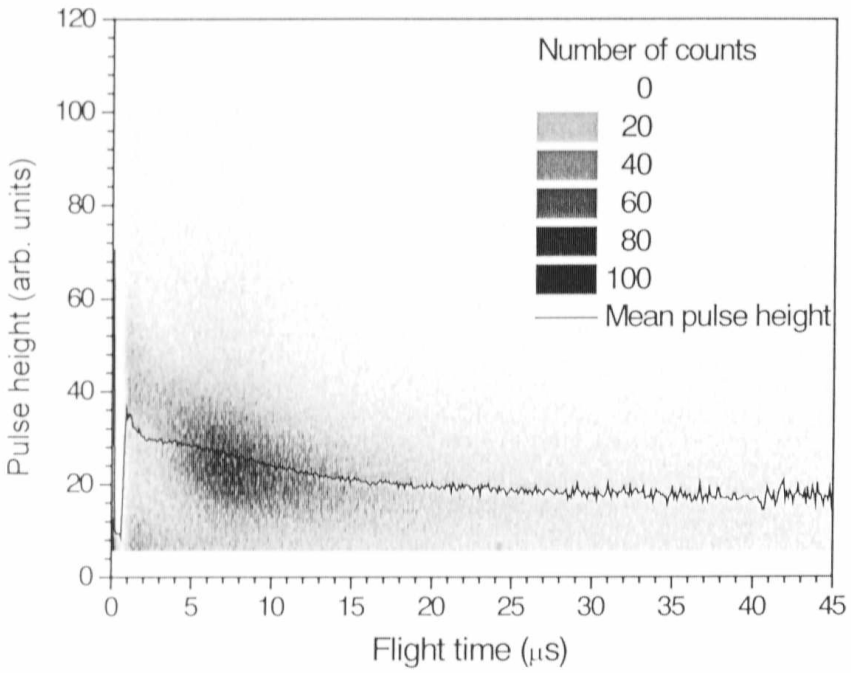


Figure 4.10. Pulse height distribution obtained from 2500 shots of 14000-atom Xe clusters irradiated at an intensity of 1.5×10^{16} Wcm^{-2}. The number of ion hits at each height is shown for each flight time, together with the mean pulse height. The threshold level for pulse counting was set at 6 units.(NH)

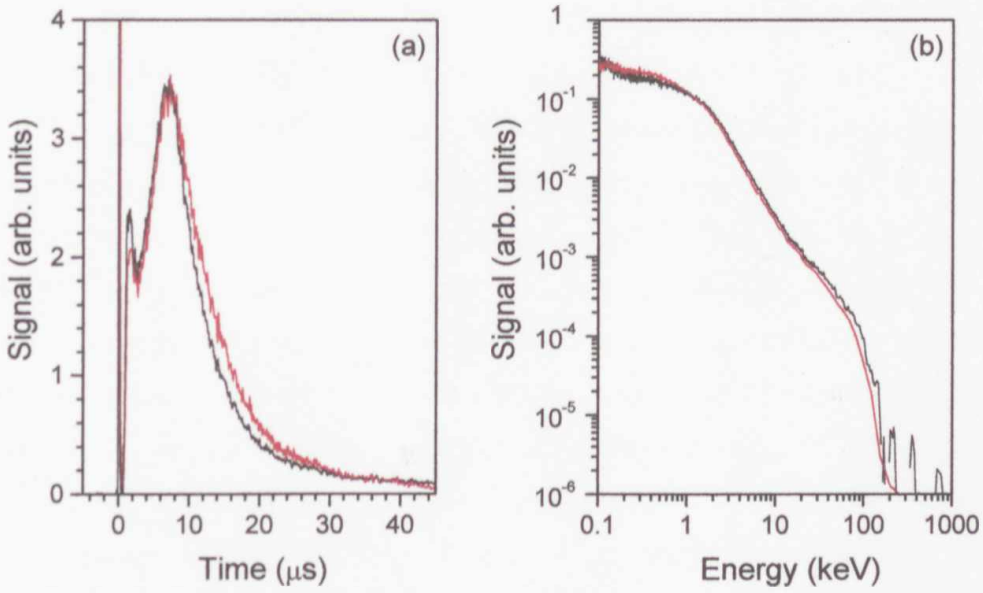


Figure 4.11. Comparison of (a) the time-of-flight traces and (b) ion energy spectra obtained by analysing the data through pulse counting (red lines) and averaging (black lines). The mean ion energies calculated in each case were 8.2 keV from averaging and 7.7keV from pulse counting.

significantly altered by this extra region of acceleration. For example, a 100 keV ion with a charge of 25+ has a flight time ~ 0.5 ns faster than a singly charged 100 keV ion on a total flight time of ~ 1 μs.

The MCP response at time T is a function of the arrival energy, which is the initial ion kinetic energy plus that gained over the final 2 mm of flight, and so depends on ion charge as well as initial kinetic energy. This means that we cannot simply correct every (averaged) ion time-of-flight spectrum by dividing by the MCP response curve in fig 4.10, as the ion charge state distribution for a given ion kinetic energy is expected to depend on the experimental parameters (such as laser intensity, cluster size and cluster medium).

The major error on the measurement of ion energies due to the uncertainty in the measurement of T_0. The time-step used on the oscilloscope varied between 1 ns and 40 ns per point. The worst case error on energy measurement is for a 1 MeV ion (which has a flight time of 314 ns) and 40 ns timestep where the error on the energy is $2\times(40/314) \sim 25\%$. For 100 keV ions, the error is less than 10%.

4.3 Conclusions

Rayleigh scattering has been used to characterise the mean size of clusters produced by a pulsed gas-jet. We have established a scaling of mean cluster size with gas-jet backing pressure, temperature and gas species which is consistent both with our measurements and with previously published scalings. We are able to produce clusters of from ~10^2 to 10^5 atoms, with radii in the region of 10 to 100 Å. Our characterisation of the mean cluster sizes could be improved by carrying out time-of-flight studies on cluster ions, after they have been singly ionised by a low intensity laser or by electron attachment.

Ions and electrons produced in the interaction of intense laser pulses with these atomic clusters can be detected and their energy spectra obtained from time-of-flight measurements. We have shown that, although our experimental techniques could be improved by implementing a pulse-counting algorithm, our current technique of averaging over many laser shots and assuming the MCP response to be flat still provides a sufficiently accurate measure of the ion energy spectrum.

Clusters irradiated by a single high-intensity, femtosecond laser pulse

5.1 Introduction

This chapter presents studies of the interaction of clusters with high-intensity, femtosecond laser pulses. The work described here concerns the first measurements of ion and electron energies from the cluster explosion. Earlier studies of the laser-cluster interaction at high intensities [McPherson 1993, 1994ab, Ditmire 1995] had concentrated on spectroscopy of the x-rays produced. These studies indicated that the interaction was extremely energetic, as x-ray emission from very highly stripped ions was observed. Studies of the time history of the radiation [Ditmire 1995] showed that it was consistent with emission from the hot, underdense bulk plasma after the clusters had expanded. The ion and electron energies were not directly measured.

We have studied the interaction of a gas of clusters with short, intense laser pulses and used time-of-flight spectrometry to measure directly the ion and electron energies. The average density of the clustered gas was much lower (10^{14} atoms cm^{-3} compared to 10^{19} cm^{-3}) than in the earlier studies of x-ray production, allowing us to isolate the laser interaction with individual clusters from the properties of the bulk plasma formed after the clusters expand. We have obtained an electron energy spectrum [Shao 1996] from the laser-cluster interaction and examined the scaling of the ion energy distribution with cluster size and cluster medium, laser intensity and laser wavelength [Ditmire 1997ab, 1998a]. These results are compared with the predictions of the nanoplasma model [Ditmire 1996], detailed in Chapter 2.

5.1.1 Anomalous x-ray emission from clusters

Studies of the interaction of atomic clusters with intense laser fields were triggered by McPherson and co-workers [McPherson 1993] when they realised that some earlier measurements of x-rays from noble gas targets had produced anomalous results due to the presence of clusters in the target gas-jets. Further investigations confirmed that the x-rays observed from clusters corresponded to transitions in Xe, Kr and Ar ions stripped to higher charge states than would be attained from single atoms irradiated at the same intensity [McPherson 1994ab]. The authors also observed x-rays identified as resulting from inner shell transitions. Atoms with inner-shell vacancies could provide a possible route for making an x-ray laser [McPherson 1994a].

Evidence that the irradiation of large clusters with intense pulses results in a hot plasma was provided by experiments carried out on mixed gas expansions [Ditmire 1996, McPherson 1996]. McPherson *et al* [1996] compared the x-ray spectra obtained from pure Xe clusters and from a Xe/Ne mixture which contained Xe clusters and monatomic Xe. The spectra observed in each case were virtually identical, indicating that the x-rays were from clusters rather from monatomic gas. Ditmire and co-workers [1996] mixed helium with a small fraction of a gas known to cluster and passed it through the gas-jet. Helium does not itself cluster, but is known to enhance the formation of clusters of heavier gases. By observing the *Ly-*α line in He^+, bulk plasma rather than intracluster effects could be studied. The intensity of the *Ly-*α line was a factor of ~100 higher with He/Ar, He/Kr or He/N_2 mixtures where large clusters were present, compared to He/Ne or pure He expansions when there is no clustering. With no clustering the line was found to decay fast, consistent with the cold plasmas produced in ATI. When clusters were present the line decayed much more slowly, consistent with a hot (>100 eV) plasma cooling by hydrodynamic expansion.

The time history of the x-ray emission from ~ 100Å noble gas clusters was then studied [Ditmire 1995, 1996]. A short-lived initial spike in the x-ray emission was observed, and this was attributed to emission from the dense cluster nanoplasmas immediately after heating by the laser, followed by lower-intensity emission on a nanosecond time-scale after the clusters had expanded. The lifetime of the lower-intensity x-ray emission was found to be consistent with the emission from the hot, underdense bulk plasma resulting after the clusters had expanded to form a uniform plasma. The short-lived spike was found to contain less than 1% of the total x-ray signal. This is in contrast to the results of McPherson *et al* [1993, 1994b] who claimed that the x-ray emission was prompt.

Again, x-rays from much higher charge states than would be expected from tunnel ionisation of atoms were observed. For example, x-rays corresponding to transitions in Kr^{10+} to Kr^{13+} was observed at a laser intensity of 1.5×10^{16} Wcm^{-2}, when an intensity in excess of

3×10^{17} Wcm^{-2} would be required to achieve these ionisation stages in monatomic krypton. Typically, 2-5% of the incident energy was converted into 250-400 eV photons, a yield comparable with that from solid targets. The authors developed the nanoplasma model [Ditmire 1996] to interpret their results (§2.4).

5.1.2 Comparison of measurements with predictions of nanoplasma model

In this chapter we present experimental measurements of the energy spectra from electrons (§5.2) and ions (§5.3) which are compared with the predictions of the nanoplasma model, which was discussed in detail in Chapter 2.

The model results obtained are from a single cluster, the size of which is the mean of the distribution as calculated in Chapter 4, table 4.1. The model laser pulses used were Gaussians with the same FWHM as the pulse-length calculated from auto-correlations (table 3.1). The FWHM of the second harmonic pulse is assumed to be $\sqrt{1/2}$ of the fundamental pulse-length, as the doubling crystal was not near saturation. The peak intensity of the laser pulse in the model is the same as the peak intensity used in the experiment. The model results are not averaged over the focal volume, or over the cluster size distribution, as the goal of this section is to gain some useful insights into the cluster explosion mechanism and its scaling with various cluster and laser parameters, rather than to attempt to reproduce the absolute values of the experimental results.

5.2 Electron energy spectra

The measured energy spectrum of electrons emitted along the direction of the laser polarisation during the irradiation of clusters of ~ 7000 xenon atoms by a 170 fs, 780 nm pulse with a peak intensity of 1.3×10^{16} Wcm^{-2} is shown in figure 5.1(a). The experimental apparatus and measurement technique are described in §4.2.1 and §4.2.2. The electron energy spectrum has a distinctive double-peaked character. The first, broad peak consists of 'warm electrons' with energies ranging from 0.1 to 1 keV. A second, sharper peak (referred to as the 'hot electrons' throughout this thesis) appears at 2.5 keV. Both peaks were only present when the laser interacts with clusters. When the interaction region contained only monatomic gas (in a static fill), we detected no electrons with energy above 100eV.

The electron kinetic energies are remarkably high. Measurements of ATI spectra from single atoms at this intensity and pulse duration have indicated that the vast majority of electrons produced have energies below 100 eV and that only a very small fraction (typically

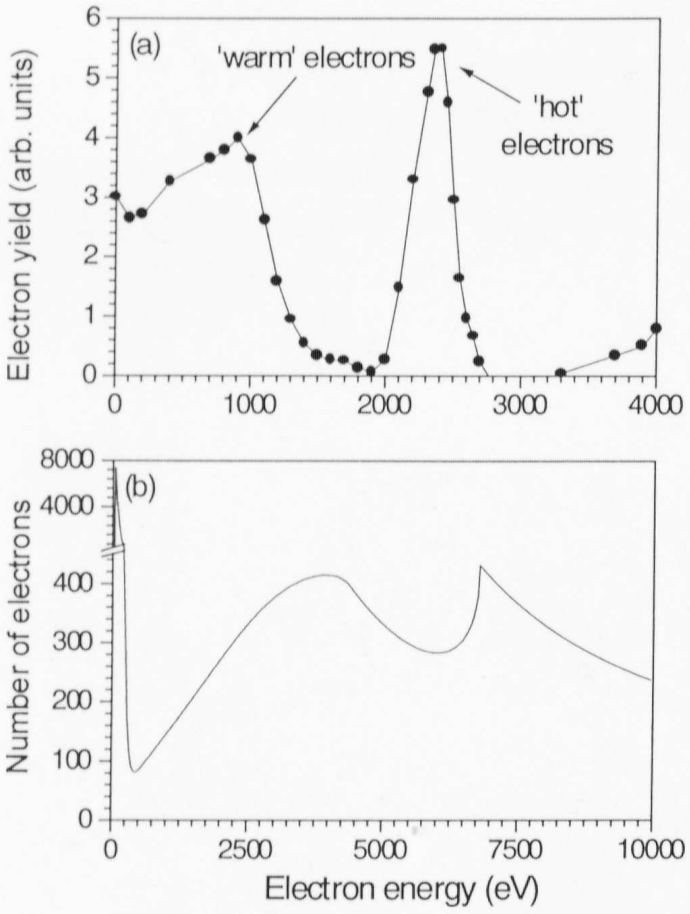


Figure 5.1. (a) Measured electron energy distribution from xenon clusters for a peak intensity of 1.3×10^{16} Wcm^{-2}. The gas-jet backing pressure was 4.5 bar, corresponding to an average cluster radius of 47 Å or 7000 atoms. (b) Calculated electron energy spectrum from a cluster of 7000 Xe atoms irradiated by a 170 fs, 780 nm pulse with a peak intensity of 1.3×10^{16} Wcm^{-2}.

10^{-2} to 10^{-3}) have energies above 200 eV [Walker 1994, Mohideen 1993]. Photoelectrons from small molecules have energies comparable to those from atoms. Zavriyev *et al* [1990] measured electrons with energies up to 100 eV from H_2. The spectrum observed from Xe clusters shows that there is a much greater coupling of laser energy to electrons than during the irradiation of single atoms or small molecules. The laser-cluster interaction may even produce hotter electrons than a laser-solid interaction at this intensity and pulse-length. Electron temperatures of 100 – 500 eV were measured from solid Al targets irradiated with fs pulses [Shepherd 1994, Guethlein 1996], and a plasma temperature of 230 eV resulted from the irradiation of Si targets with 160 fs pulses at 10^{16} Wcm^{-2} [Murnane 1989]. 2 – 10 keV electrons were reported with 1 ps pulses incident on layered Si/Al targets at an intensity of 2×10^{16} Wcm^{-2} [Meyerhofer 1993]. Much hotter electrons, with temperatures ~ 10^2 – 10^3 keV, have been measured from solid targets irradiated by long laser pulses of ~ 10 ps – 100 ns [Gitomer 1986].

Varying the gas-jet backing pressure enables us to study the effect of cluster size on electron yield. Figure 5.2 shows the variation of hot electron production with gas-jet backing pressure, obtained by integrating the MCP signal over time. Hot electron production has a sharp onset with a gas-jet backing pressure of ~ 1.2 bar, corresponding to a cluster size of approximately 300 atoms. No hot electrons are observed at lower backing pressures and smaller cluster sizes than this. Only the irradiation of large clusters of more than ~ 300 atoms results in a measurable hot electron signal.

The calculated electron energy distribution from a cluster of 7000 xenon atoms

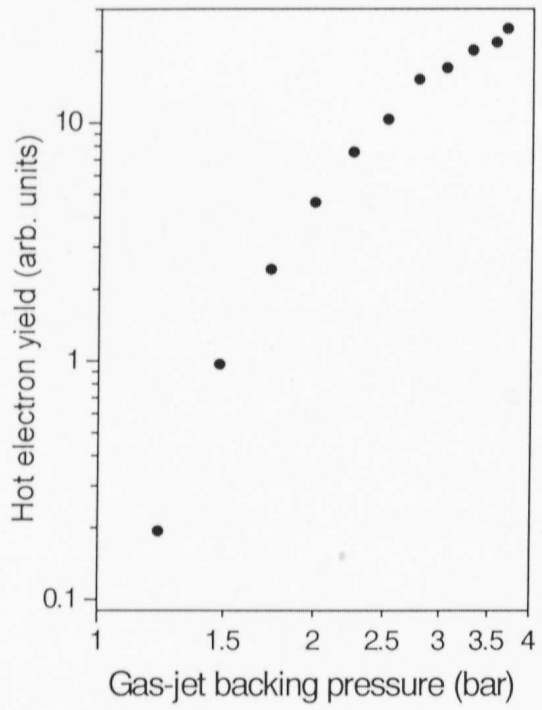


Figure 5.2. Measured yield of hot electrons as a function of xenon backing pressure. The peak laser intensity was 1.3×10^{16} Wcm^{-2}.

irradiated by a 170 fs, 780 nm pulse with a peak intensity of 1.3×10^{16} Wcm^{-2} is shown in figure 5.1b. The spectrum was calculated by summing the energy distributions of the electrons ejected from the cluster at each step throughout the laser pulse. The energy distribution of all the electrons in the cluster at any point in time is assumed to be Maxwellian. The electrons that leave the cluster have energy greater than the escape energy of the cluster (and are also within one mean free path of the surface heading out of the cluster) and so are in the hot tail of the Maxwellian.

If the calculated electron energy distribution is compared to the experimentally measured spectrum (figure 5.1a), taken with nominally the same cluster size and laser pulse parameters, it can be seen that the model does successfully reproduce the two-peaked character of the electron spectrum. The calculated distribution has a sharp hot electron peak at 7 keV, a broader warm electron peak from ~ 1–5 keV, and a large number (approximately 15% of the total) of low-energy electrons with energies below 100 eV. The low energy electrons would not have been detected experimentally as their long flight times would have fallen outside the time-gate we integrated over.

The model indicates that the sharp hot electron peak consists of electrons ejected at the point in the expansion where the electron density in the cluster drops to 3 times the critical electron density. At this point the mean electron energy rises sharply to > 20 keV and the escape energy increases to 7 keV, so a large number of high energy electrons leave the cluster. The broad tail of the hot electron peak arises because the electron energy distribution is assumed to be Maxwellian. In reality, the distribution will not have time to thermalise fully, and the high-energy tail of the electron energy distribution will not be fully populated. The model over-estimates the energy of the hot electron peak (the calculated peak is at 7 keV, whereas the measured peak was at 2.5 keV).

The warm electron peak consists of electrons which leave the cluster earlier on in the laser pulse, before the sharp peak in the collisional heating, when the escape energy and mean electron temperature are much lower.

The majority of the low energy electrons are those which were still inside the cluster at the end of the explosion (after the cluster expansion velocity has stopped increasing).

The model predicts that the temperature of the hot electron peak is a sensitive function of the cluster size (it is, in fact, linearly related to the maximum ion energy). Integrating the electron energy distributions over a typical log-normal distribution of cluster sizes broadens the hot electron peak significantly. It is not clear why we observed such a sharp hot electron peak, and this is a crucial question for further work. It is possible that the cluster size distribution is narrower than we expect. Experiments are currently in progress to measure the cluster size distribution from our jet. More data on the electron spectra is also

needed to establish whether the hot electron peak shifts in energy under different laser and cluster conditions, as predicted by the model.

5.2.1 Angular distribution of electrons

The presence of two distinct peaks in the electron energy spectrum suggests that these two groups may be produced under different conditions at different times in the cluster expansion. This assumption is supported by examining the angular dependence of the electron emission with respect to the laser polarisation (Figure 5.3). The angle between the direction of polarisation and the detector was varied with a $\lambda/2$ plate placed before the entrance to the vacuum chamber. The measured angular distribution of warm electrons is shown in figure 5.3a, and that of the hot electrons in figure 5.3b.

The angular distributions of the two groups of electrons are markedly different. The hot electron emission is completely isotropic while warm electron emission is peaked along the laser polarisation. The warm electron peak has a full-width at half-maximum of about

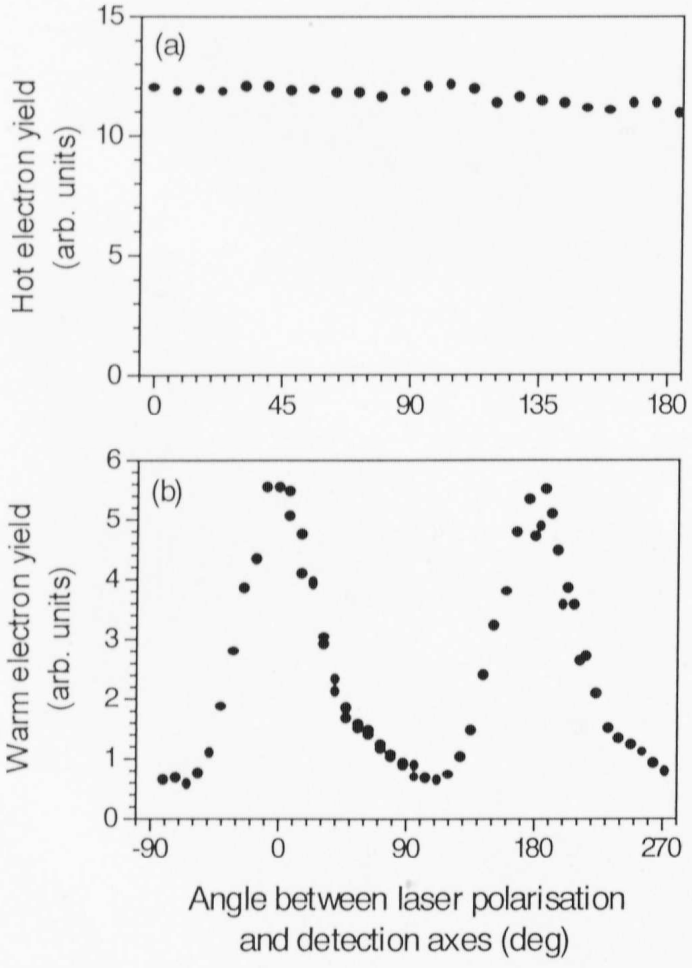


Figure 5.3. (a) Angular distribution of 'hot electrons' with energies ranging from 2 to 3 keV. (b) Angular distribution of 'warm electrons' with energies ranging from 0.3 to 1 keV. Emission along the direction of laser electric field polarisation is defined as being at 0° and 180°. The average cluster size was 5300 atoms and the laser intensity was 1.3×10^{16} Wcm^{-2}.

60°. Both these distributions are significantly different from the angular distributions associated with single atoms. The electrons from high-order ATI are expected to have a much narrower angular distribution. A width of 15-20°, peaked along the laser polarisation, was reported by Mohideen *et al* [1993]. In high field tunnelling ionisation, the narrow angular distribution stems from the much higher tunnelling rate in the direction of the laser field. The electrons observed in our experiment cannot, therefore, be interpreted as simply resulting from the tunnel ionisation of individual atoms. Some re-scattering of the electrons by ions in the cluster is necessary to explain the broadening observed in the warm electron distribution. The isotropic distribution of the hot electrons indicates that these electrons have undergone many electron-ion collisions in the laser field, completely randomising their velocity distribution.

The different angular distributions of the two groups of electrons are consistent with the nanoplasma model which predicts that the warm electrons leave the cluster before the collisional heating peak at $3\ n_{critical}$, and that the hot electrons leave after this peak having undergone many collisions.

5.3 Ion energy spectra

The remarkably high energies of the electrons produced in the intense laser-cluster interaction suggest that highly charged ions with large kinetic energies may also be ejected from the cluster. Hot ions are indeed observed, as the TOF trace in figure 5.4 illustrates. The measurement of ion energies is described in detail in §4.2.3. The spike near zero time is due to electrons with energies above 2 keV, while the lobe extending out from ~300 ns is due to ions. With xenon in a 38 cm drift tube, 1 MeV ions have a flight time of 300 ns, and 100 keV ions have a 1 μs flight-time.

The energy spectrum of ions resulting from the interaction of ~ 9000-atom Xe clusters with a laser pulse of intensity ~ 1.5×10^{16} Wcm^{-2} is shown in figure 5.5a (obtained from the TOF trace in figure 5.4). Nearly 0.5% of the ions have energies of more than 1 MeV. This energy is four orders of magnitude higher than has previously been observed in the Coulomb explosion of molecules [Cornaggia 1994] and about 1000 times higher than the energy of Ar ions ejected in the disintegration of small clusters of up to six argon atoms irradiated at 10^{15} Wcm^{-2} reported by Purnell *et al* [1994]. The average ion energy of this distribution is 91 ± 5 keV. We find that the mean ion energy is typically ~ 10% of the maximum.

Figure 5.5b compares the ion energy distribution with a Maxwellian with the same mean energy and with the distribution expected from the isotropic expansion of a uniform sphere. With a uniform isotropic expansion, the ion energy increases linearly from zero with the cluster radius, so the number of ions at each velocity, v, will be proportional to v^2. The measured energy spectrum is totally different from both of these models. This indicates that

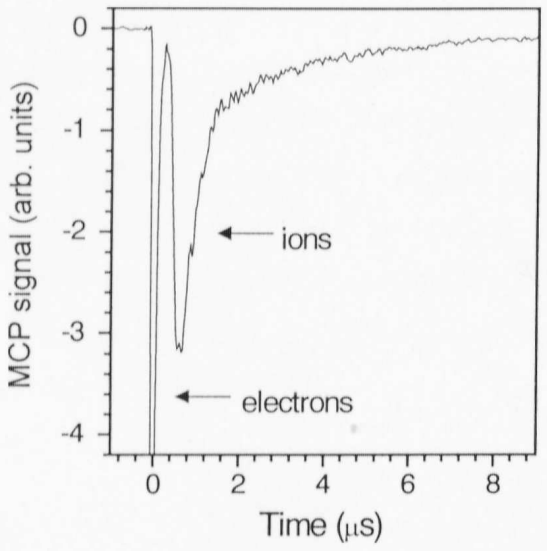


Figure 5.4. Time-of-flight spectrum from 9000-atom xenon clusters (backing pressure 5 bar) irradiated by a peak intensity of 2×10^{16} Wcm^{-2}. The 38cm flight tube was field-free, but electrons with energy <2 keV are not detected as the front plate of the MCP is charged to +2 kV.

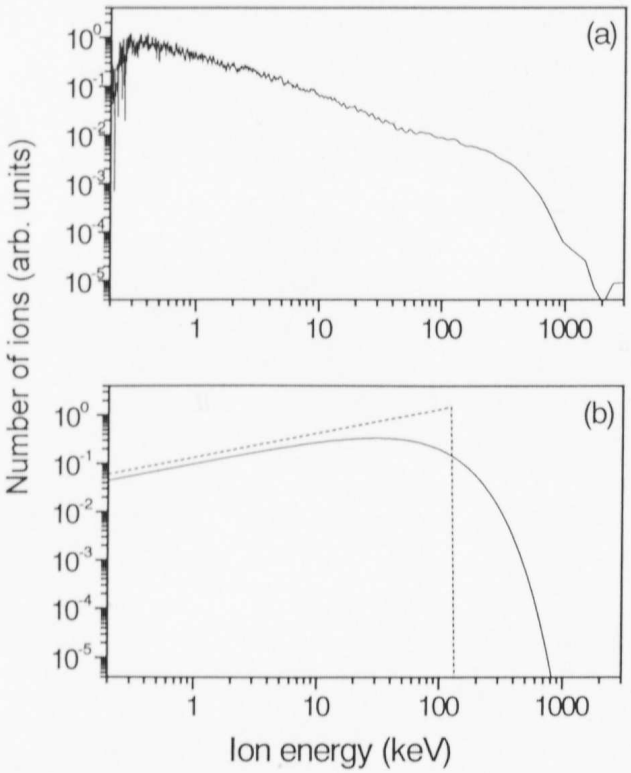


Figure 5.5. (a) Ion energy spectrum from clusters of 9000 Xe atoms irradiated by a peak intensity of 1.5×10^{16} Wcm^{-2}, derived from the time-of-flight trace shown in figure 5.4. The mean ion energy is 91 keV. (b) Solid line: Maxwellian with a mean energy of 91 keV. Dotted line: Uniform isotropic expansion with a mean energy of 91 keV.

the nanoplasma model is inadequate for modelling the expansion of the cluster plasma after it is heated.

5.3.1 Angular distribution of ions

Figure 5.6a shows the raw time-of-flight signal from 5300-atom clusters as a function of angle with respect to the direction of laser polarisation. The polarisation was rotated by placing a $\lambda/2$ plate in the beam path just before the vacuum chamber. The time-of-flight distribution appears to be isotropic with respect to the direction of laser polarisation, but calculation of the mean ion energy as a function of laser polarisation (figure 5.6b) reveals that the mean ion energy is ~ 15% higher along the direction of laser polarisation than perpendicular to it. Some anisotropy of the exploding ions would be expected as the warm electrons are also emitted anisotropically, with a peak along the direction of the laser polarisation (as shown in figure 5.3).

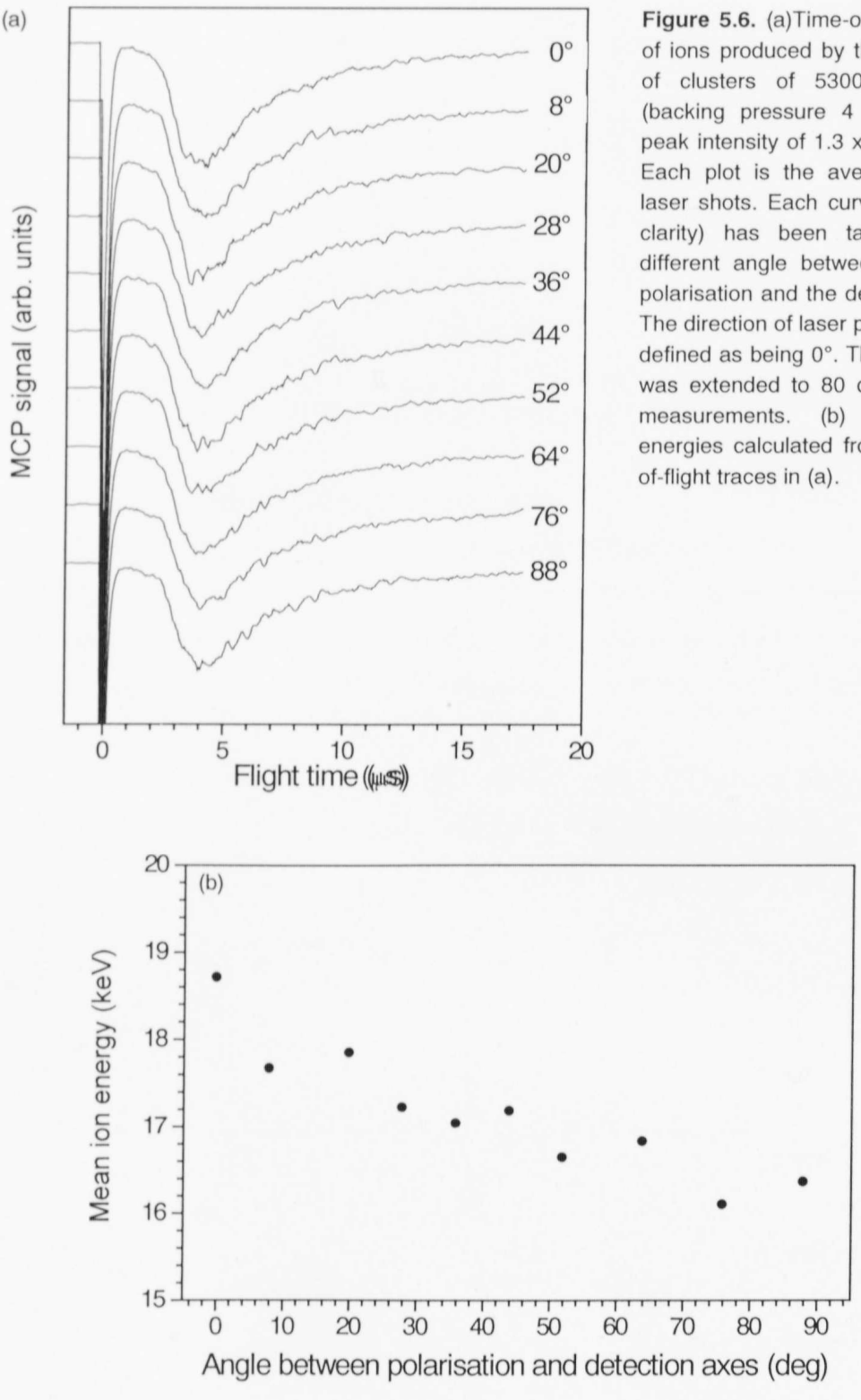


Figure 5.6. (a)Time-of-flight traces of ions produced by the irradiation of clusters of 5300 Xe atoms (backing pressure 4 bar) with a peak intensity of 1.3×10^{16} Wcm^{-2}. Each plot is the average of 500 laser shots. Each curve (offset for clarity) has been taken with a different angle between the laser polarisation and the detection axis. The direction of laser polarisation is defined as being 0°. The flight tube was extended to 80 cm for these measurements. (b) Mean ion energies calculated from the time-of-flight traces in (a).

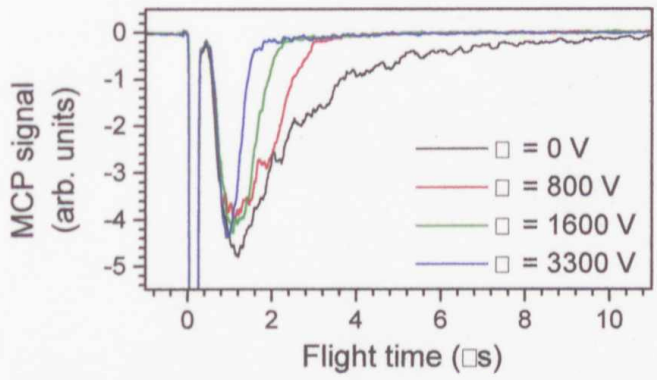


Figure 5.7. Ion TOF traces with 38 cm flight tube of 9000-atom Xe clusters irradiated with a peak intensity of 1.3 x 10^{16} Wcm^{-2} at retarding voltages of 0, 800, 1600 and 3300 V.

5.3.2 Charge state distributions

Another striking feature of the ions produced from the cluster explosion is ionisation to very high charge states. X-rays from highly stripped Xe and Kr ions have been observed by McPherson *et al* [1994ab]and Ditmire *et al* [1995]. Both these papers reported charge states significantly higher than would be expected from simple field ionisation at the intensities used.

Figure 5.7 shows the time-of-flight spectra from ~4700-atom xenon clusters irradiated by 1.3 × 10^{16} Wcm^{-2} as the retarding voltage, Φ, is varied from 0 to 3.3 kV. The

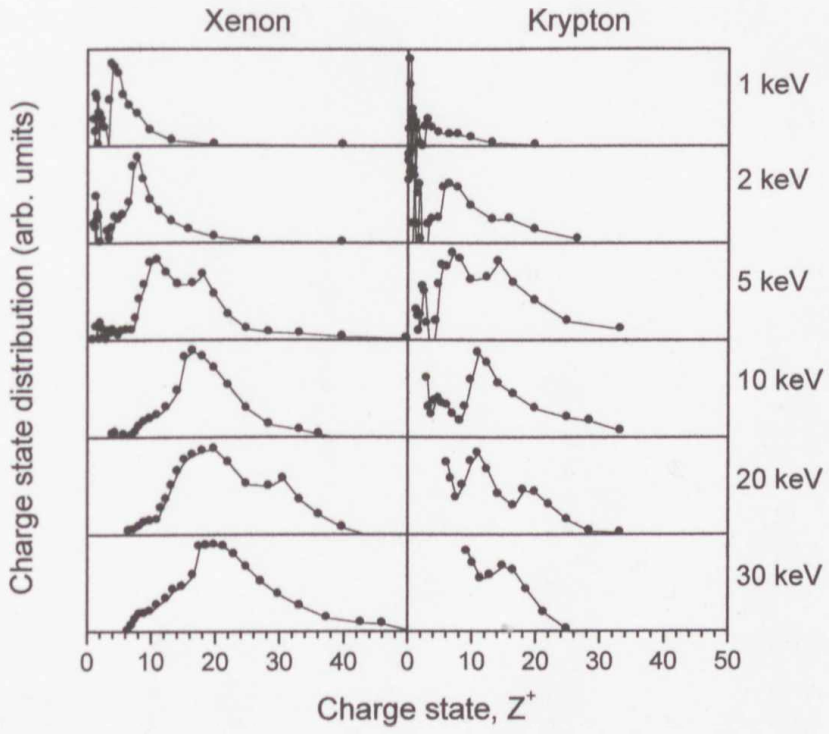


Figure 5.8. Measured charge state distribution of clusters of 9000 Xe atoms (backing pressure 5 bar) and 3100 Kr atoms (6 bar) irradiated with a peak intensity of 1.3 x 10^{16} Wcm^{-2} for ion kinetic energies of 1, 2, 5, 10, 20 and 30 keV.(JT)

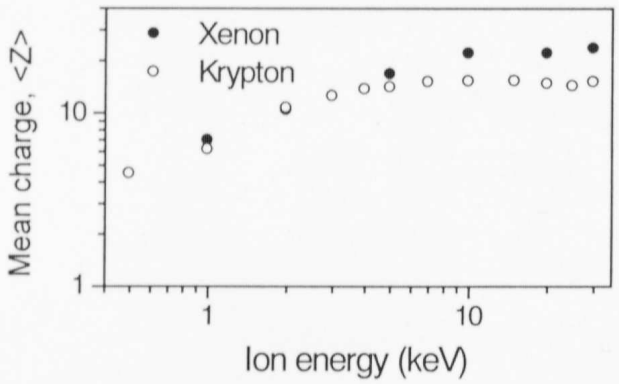


Figure 5.9. Mean charge state as a function of ion kinetic energy for Xe (solid circles) and Kr (open circles), calculated from the ion charge state distributions in figure 5.8.

retarding voltage introduces a potential barrier to ions with energies less than $Ze\Phi$, without significantly altering the flight-times of higher energy ions. The charge state distributions calculated from these spectra (as detailed in §4.2.3) are shown in figure 5.8 for kinetic energies from 1 to 30 keV. For high-energy Xe ions, the peak is at Z = 18^+ to 25^+, with some ions having charge states as high as 40^+. These are much higher charge states than those expected from field ionisation of single atoms at these intensities. We would expect to see charge states out to 8^+ in xenon at an intensity of 1.3×10^{16} Wcm^{-2} [Augst 1991]. Over-the-barrier ionisation to Xe^{36+} would require an intensity of nearly 5×10^{18} Wcm^{-2} [Augst 1991] if the ionisation were due to this alone.

Figure 5.8 also shows the ion charge state distributions from ~ 3100-atom krypton clusters at the same intensity. The shapes of the charge state distribution for a given ion energy are very similar in the two species, but the charge states attained are lower in Kr than Xe. The peak for high energy krypton ions is at 12^+ to 17^+ (as against 18^+ to 25^+ in xenon) with the highest charge state present being around Z = 25^+. At an intensity of 1.3×10^{16} Wcm^{-2}, over-the-barrier ionisation of atomic krypton would be expected to produce charge states out to 7^+; ionisation to 25^+ would require 10^{19} Wcm^{-2}.

The mean charge state attained depends only weakly on the ion kinetic energy (figure 5.9). The mean charge increases with ion energy up to an energy of ~4 keV, before levelling off at ~20^+ in xenon and ~14^+ in krypton. The nanoplasma model assumes that all the ions in the cluster have the same charge, irrespective of their energy, so this result confirms that it is a sensible approximation.

The calculated charge state distribution from clusters of 10^4 xenon, krypton or argon atoms are shown in figure 5.10. The model predicts that the charge states attained are from 12^+ to 17^+ in xenon clusters, from 10^+ to 15^+ in krypton and from 7^+ to 10^+ in argon. If the ionisation was due to field ionisation alone, the intensities required would be ~ 1 - 4 $\times 10^{17}$ Wcm^{-2} for Xe, $2 \times 10^{17} - 1 \times 10^{18}$ Wcm^{-2} in Kr and $2 \times 10^{17} - 2 \times 10^{18}$ Wcm^{-2} in Ar. The model assumes that the charge state distribution is not a function of the ion

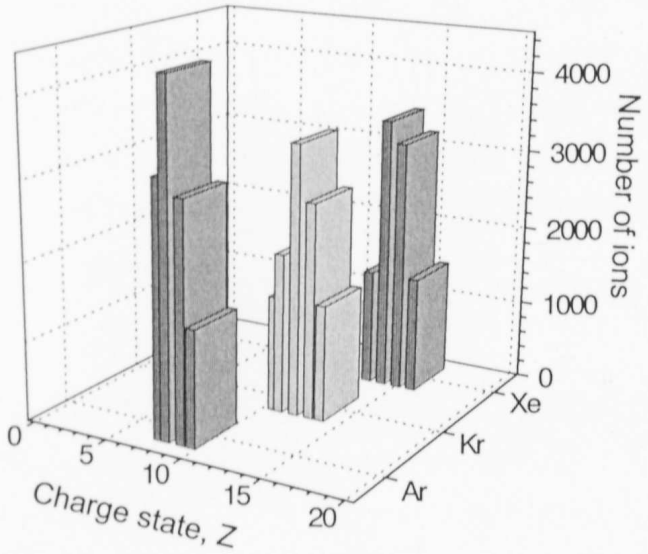


Figure 5.10. Calculated charge state distributions from clusters of 10^4 Xe, Kr or Ar atoms irradiated by a 170 fs, 780 nm pulse with a peak intensity of 1.3×10^{16} Wcm^{-2}.

energy. These charge state distributions are much narrower than the experimentally measured distributions in figure 5.8, but the charge states attained are comparable to those measured for 10 keV Xe and Kr ions. Both experiment and model agree that charge states much higher than those produced from atoms irradiated at the same intensity are produced. Thermal collisional ionisation in the cluster, which occurs primarily while the cluster is shielded from the external laser field, strips the ions to higher charge states.

Numerical calculations for a variety of cluster targets (figure 5.11), with 6000 atoms per cluster, show that the maximum ion energy achieved in the explosion depends on the

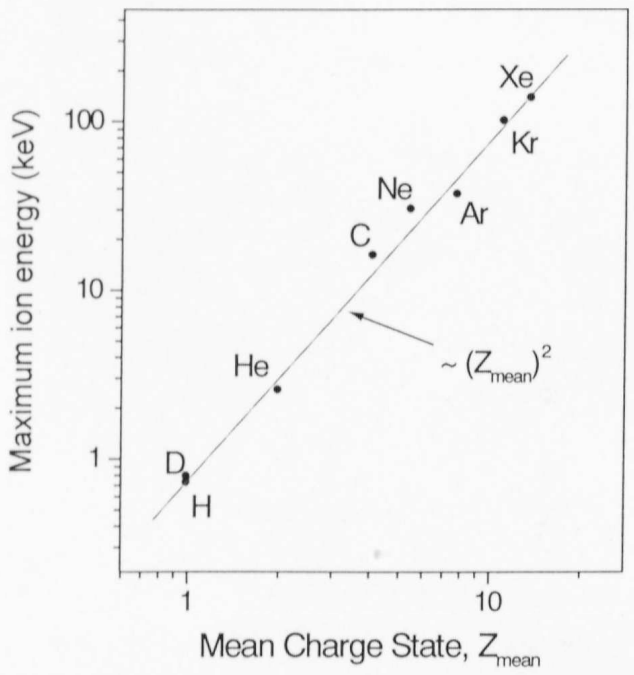


Figure 5.11. Calculated maximum ion energy as a function of mean charge state obtained in the explosion for eight different atomic species. The cluster size was 6000 atoms and the laser pulse was 780 nm. 260 fs, 2×10^{16} Wcm^{-2}.

square of the mean charge of the target atom. (There is no dependence on the atomic mass in this scaling, the same scaling is found if the calculations are performed for xenon with the ionisation potentials raised to 1 keV to clamp the ionisation at a given charge state). This Z^2 scaling of the ion energy is typical of Coulomb explosions, but in the nanoplasma model the hydrodynamic pressure of the hot electrons exceeds the Coulomb pressure by at least a factor of ~10 throughout the explosion.

5.3.3 Scaling with cluster size

Our ability to control the cluster size by changing the backing pressure of the gas-jet enables us to examine the scaling of the ion energies with cluster size. Figure 5.12 shows the time-of-flight spectra obtained from the interaction of clusters of 200 to 74000 atoms with a laser pulse of 3×10^{15} Wcm^{-2}. The time-of-flight signal has been scaled by the backing pressure to account for the numbers of atoms in the interaction region. The ion energy spectra are shown in figure 5.13 and the maximum ion energies of these distributions are shown in figure 5.14.

Hot ions (with energies above 1 keV) are first observed in the time-of-flight signal at a backing pressure of 1 to 1.3 bar. This pressure corresponds to the onset of hot electron production from the exploding clusters (figure 5.2). The time-of-flight spectra also show that electrons with energies above 2 keV (they must have an energy greater than this to reach the MCP) are only detected when hot ions are produced. This points to a change in the dynamics

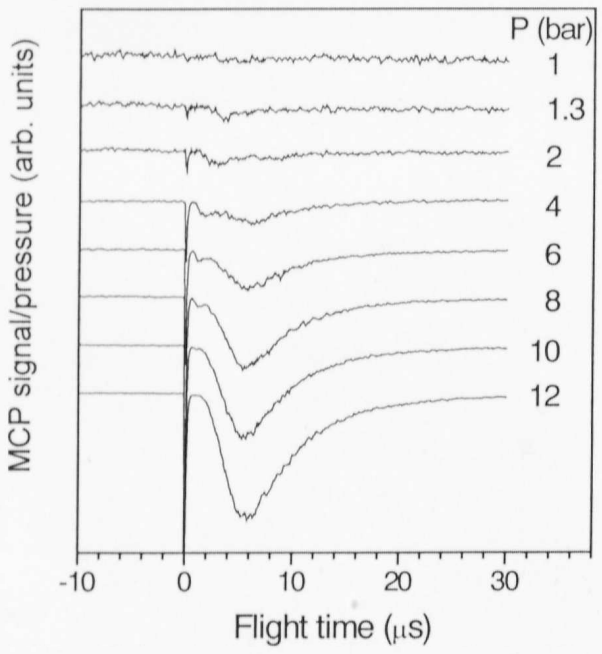


Figure 5.12. Ion time-of-flight spectra from clusters of 200, 400, 1000, 5300, 14000, 28000, 47000 and 74000 xenon atoms (backing pressures 1, 1.3, 2, 4, 6, 8, 10 and 12 bar respectively) irradiated by a 230 fs pulse with a peak intensity of 2.8×10^{15} Wcm^{-2}. The 38 cm flight tube was field-free. The curves are offset for clarity. The signal has been scaled to account for the number of monomers ejected by the gas-jet.

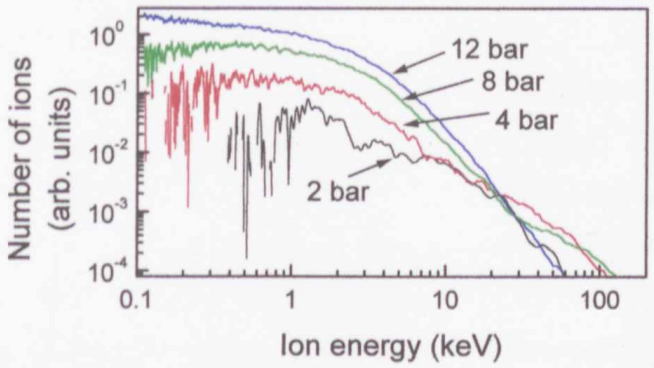


Figure 5.13. Ion energy spectra obtained from the time-of-flight spectra in figure 5.12.from clusters of 1000, 5300, 28000 and 74000 xenon atoms (backing pressure 2, 4, 8 and 12 bar respectively) irradiated by a peak intensity of 2.8×10^{15} Wcm^{-2}. The signal has been scaled to account for the number of monomers ejected by the gas-jet.

of the cluster expansion once the cluster size increases to above ~ 200-400 atoms.

The time-of-flight spectra (figure 5.12) clearly show the presence of a second, hotter ion peak at flight times < 2 μs, corresponding to energies > 25 keV, at backing pressures of 4 to 6 bar (~ 5000 to 14000 atoms). The presence of more hot ions at these backing pressures can also be seen in figure 5.13. The total number of ions detected appears to increase with backing pressure, but we only detect ions with a flight time < 30 μs which will have energies above 100 eV.

The maximum ion energy (figure 5.14a) rises from 8 keV at 1 bar (200 atoms/cluster) to 53 keV at clusters of ~ 5000 – 15000 atoms before falling to 28 keV as the

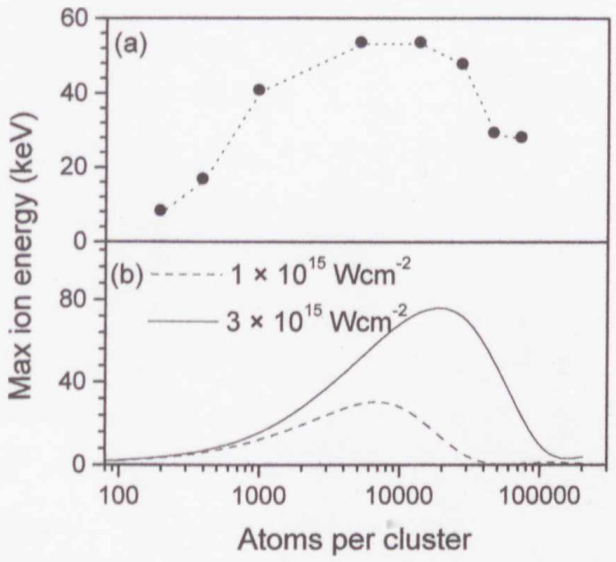


Figure 5.14. (a) Maximum ion energies obtained from the time-of-flight spectra in figure 5.12. The peak laser intensity was 2.8×10^{15} Wcm^{-2}. (b) Calculated ion energies as a function of cluster size for 230 fs, 780 nm pulses with peak intensities of 1×10^{15} Wcm^{-2} (dashed line) and 3×10^{15} Wcm^{-2} (solid line).

cluster size is increased beyond 50,000 atoms/cluster. The mean ion energies (not shown here) follow a similar trend.

Figure 5.14b shows numerical calculations from the nanoplasma model of the variation of maximum ion energy with cluster size for 230 fs, 780 nm pulses with peak intensities of 1×10^{15} Wcm^{-2} and 3×10^{15} Wcm^{-2}. The model predicts the existence of an optimum cluster size, which increases with the laser intensity. The optimum size is ~ 6000 atoms at 1×10^{15} Wcm^{-2} and 20,000 atoms at 3×10^{15} Wcm^{-2}. The predicted variation in ion energy with cluster size is in good agreement with that measured experimentally, especially as there is an uncertainty of a factor of two in the experimental intensity calibration.

The nanoplasma model suggests that the dynamics of the explosion is governed by the point in the laser pulse at which the cluster experiences the resonant heating. The highest ion temperatures are obtained when the cluster passes through the $3\, n_{critical}$ point close to the peak of the laser pulse. Small clusters expand more quickly and reach this point before the peak: larger clusters pass through $3\, n_{critical}$ well after the peak. Increasing the intensity increases the initial ionisation and expansion rates so that the $3\, n_{critical}$ point occurs earlier in the laser pulse for a given cluster size. This shifts the optimum size towards larger clusters.

The model is unable to reproduce the sharp onset of the cluster explosion at a cluster size of a few hundred atoms which was observed experimentally. The model is only constructed to study the field-enhancement mechanism and so is only valid when the ionised cluster is big enough to be approximated as a plasma. This reinforces the point that there is a dramatic change in the cluster dynamics once the clusters contain more than a few hundred atoms.

5.3.4 Intensity dependence

We have examined the scaling of the ion energy distribution with laser intensity and the resulting plots of mean and maximum ion energies are shown in 5.15. There is a sharp onset of hot ion production at an intensity of 6×10^{14} Wcm^{-2}. The mean and maximum ion energies rise steeply up to ~ 1×10^{15} Wcm^{-2}, where the mean is ~ 5 keV and the maximum is ~ 50 keV. At intensities higher than these, the mean and maximum ion energies increase only weakly with increasing intensity and the integrated ion yield increases as $\sim I^{1.4}$, consistent with the increase in focal volume (an $I^{3/2}$ scaling would be expected for a Gaussian focal spot). At 1×10^{16} Wcm^{-2}, the maximum ion energy is 90 keV and the mean is 7 keV.

The calculated intensity dependence of the mean ion energy attained in the explosion of 5300- and 14,000-atom Xe clusters irradiated by a 230 fs pulse is shown in figure 5.16. The intensity dependence is very similar for both cluster sizes. Below

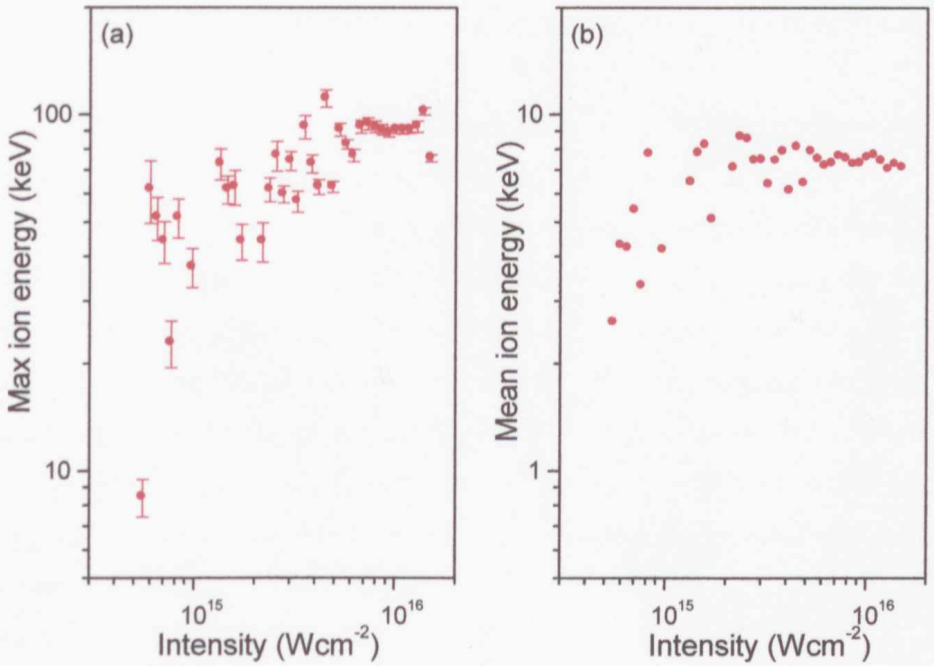


Figure 5.15. (a) Maximum and (b) mean ion energies measured as a function of laser intensity from 3×10^{14} Wcm^{-2} to 2×10^{15} Wcm^{-2}. There were 5300 Xe atoms per cluster. The 780 nm laser pulse was 230 fs long (1997).

6×10^{13} Wcm^{-2}, the clusters are not strongly ionised and do not explode (their radial velocities do not increase).

The mean ion energy increases sharply with laser intensity from 40 eV at 6×10^{13} Wcm^{-2} to 2 keV at 3×10^{14} Wcm^{-2}. In this intensity region, the amount of ionisation is sufficient that the electron density within the cluster reaches $3\ n_{critical}$, at which point the field in the cluster is enhanced with respect to the laser field and the cluster expansion velocity

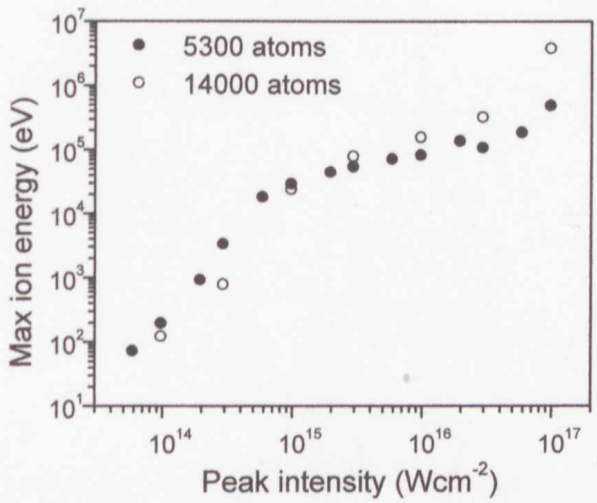


Figure 5.16. Calculated intensity dependence of the maximum ion energy for Xe clusters of 5300 (filled circles) and 14000 atoms (open circles). The laser pulse was 230 fs long and had a wavelength of 780 nm.

increases. The expansion velocity is not, however, large enough compared to the ionisation rate that the electron density in the cluster can drop to $3\ n_{critical}$ again before the laser pulse has passed.

When the laser intensity is greater than $\sim 6 \times 10^{14}$ Wcm^{-2} the cluster is ionised enough to reach $3\ n_{critical}$ fairly early on in the laser pulse. It then starts to expand and the combination of collisional ionisation and cluster expansion causes the electron density to rise and then fall through $3\ n_{critical}$ before the laser intensity drops off. As the electron density drops through $3\ n_{critical}$ for the second time, the field in the cluster is strongly enhanced and the radial acceleration increases dramatically. In this intensity regime, the ion energies increase only slowly with increasing intensity. The maximum ion energies produced under these conditions range from ~ 20 keV at 6×10^{14} Wcm^{-2} to ~ 100 keV at 10^{16} Wcm^{-2} for both cluster sizes. These numerical results are in extremely good agreement with the experimental measurements, matching both the general trends and the point where the ion energies start to level off.

5.3.5 Wavelength scaling

We have examined the wavelength scaling of the cluster explosion dynamics by carrying out a comparative study of the ion energy spectra at the laser fundamental and the second harmonic. For these experiments the laser was frequency doubled to 390 nm using a

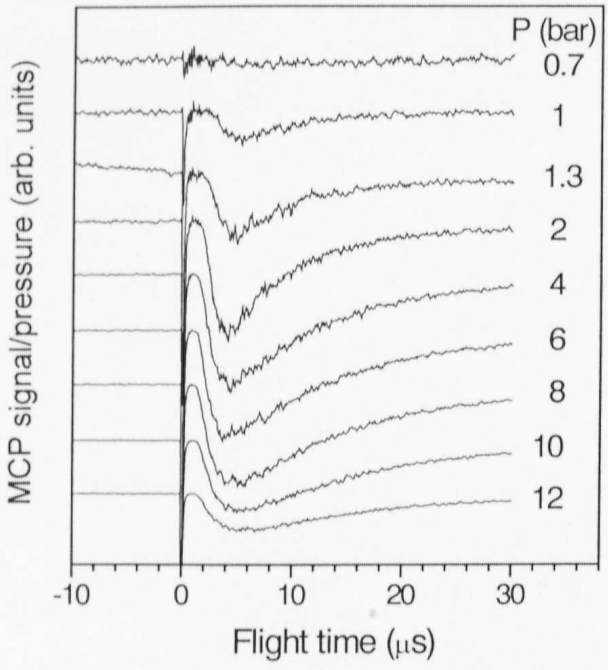


Figure 5.17. Ion time-of-flight spectra from clusters of 80, 200, 400, 1000, 5300, 14000, 28000, 47000 and 74000 xenon atoms (backing pressures 0.7, 1, 1.3, 2, 4, 6, 8, 10 and 12 bar respectively) irradiated by a 390 nm pulse with a peak intensity of 5.0×10^{15} Wcm^{-2}. The 38 cm flight tube was field-free. The curves are offset for clarity. The signal has been scaled to account for the number of monomers ejected by the gas-jet.

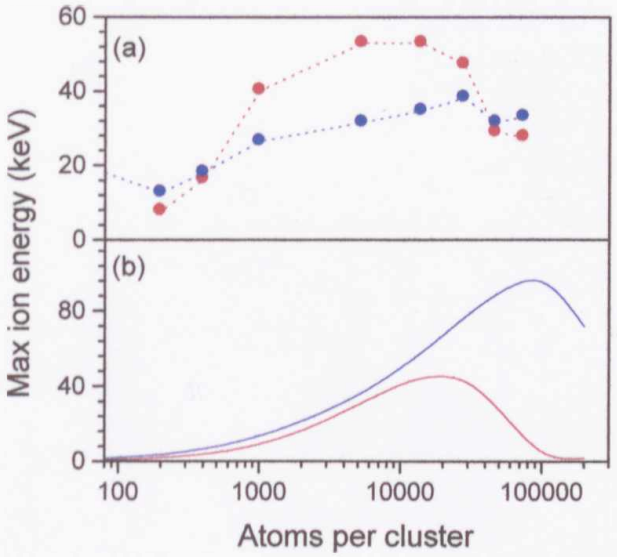


Figure 5.18. (a) Maximum ion energies measured in the interaction of xenon clusters with 780 nm (red circles) and 390 nm (blue circles) radiation. The peak intensity of the 390 nm pulses was 5.0×10^{15} Wcm^{-2} and that of the 780 nm pulses was 2.8×10^{15} Wcm^{-2}. (b) Calculated mean ion energy as a function of cluster size for Xe atoms irradiated by a 230 fs, 780 nm pulse (red) or a 160 fs, 390 nm pulse with a peak intensity of 3×10^{15} Wcm^{-2} (blue).

3 mm thick Type 1 KDP crystal. The second harmonic was vertically polarised for all these experiments which means that the electric field vector was perpendicular to the detection axis.

Similar behaviour is found in the cluster explosion with IR (780 nm) and blue (390 nm) light. As with the IR, the mean and maximum ion energies with 390 nm light are approximately 15-20% lower perpendicular to the laser polarisation than parallel to it. All measured ion energies in the blue should be scaled up by this amount for comparison with the IR.

Figure 5.17 shows time-of-flight spectra from Xe clusters varying in size from 200 to 74,000 atoms (backing pressure 1 bar to 12 bar) irradiated by 5×10^{15} Wcm^{-2} of 390 nm radiation. The maximum ion energies calculated from these spectra, together with those from clusters irradiated by 3×10^{15} Wcm^{-2} of IR (from figure 5.14) are shown in figure 5.18a.

Hot ions are only produced with backing pressures greater than one bar, when clusters of more than 200 atoms are present in the jet, as was found with IR irradiation. The mean ion energies increase sharply up to a energy of 5 keV at 2 bar (1000 atoms), and then stay roughly constant as the cluster size is increased further. The maximum ion energies follow a similar trend. The optimum cluster size is larger for the blue than the IR, at about 28,000 atoms. For large cluster sizes, the second harmonic produces higher mean and maximum ion energies than does the fundamental.

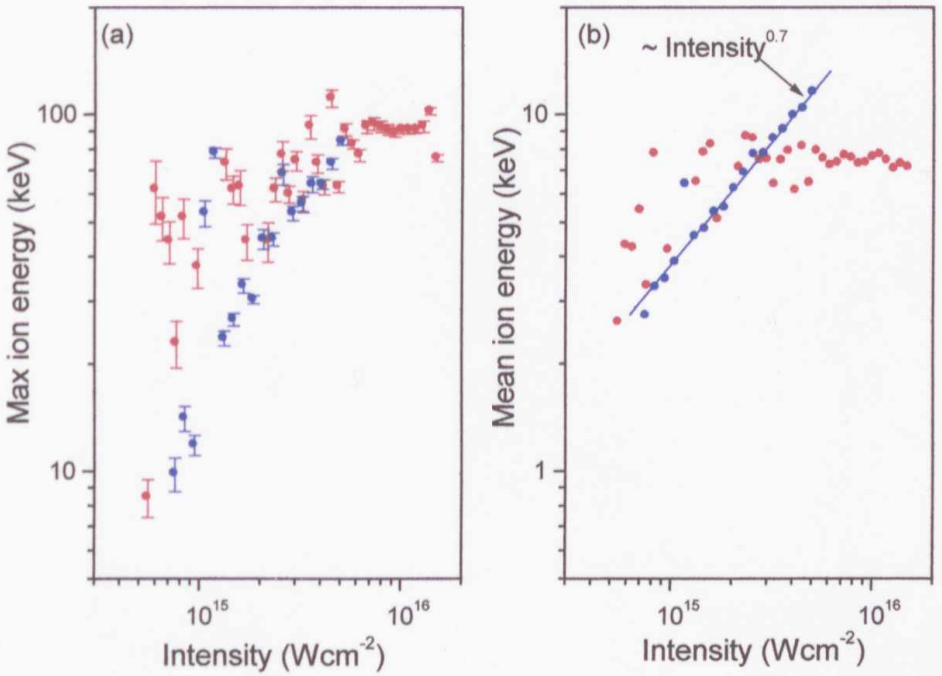


Figure 5.19. Measured intensity dependence of the maximum (a) and mean (b) ion energies from the irradiation of 5300-atom Xe clusters with 390 nm (blue circles) and 780 nm (red circles) laser pulses (1997).

Numerical calculations have been performed to compare the mean ion energy resulting from the explosion of clusters of Xe atoms irradiated by laser pulses at 780 nm and 390 nm with the same intensity over a range of cluster sizes (figure 5.18b). At low cluster sizes (<10,000 atoms), the mean energy in the blue is ~ 5 keV higher with 390 nm irradiation than with 780 nm. The optimum cluster size is ~ 20,000 atoms at 780 nm and 80,000 atoms at 390 nm. The ion energies obtained with the second harmonic are predicted to be much higher than with the fundamental for large cluster sizes. If these results are compared with figure 5.18a, it can be seen that model is in only partial agreement with the experiment. With cluster sizes below 10,000 atoms, the measured explosion energies are lower in the blue than the IR. At larger cluster sizes, the mean energies are higher in the blue, as predicted by the model. Both experiment and model agree that the optimum cluster size is bigger in the blue than the IR.

Experimental measurements of the intensity dependence of the mean and maximum ion energies in the IR and the blue for clusters of 5300 Xe atoms show that the intensity scaling is very different for the two wavelengths (figure 5.19). While the clusters irradiated with IR pulses exhibit a sharp increase in energy with laser intensity followed by a plateau, the energies of clusters irradiated with blue light increase as $\sim I^{0.7}$ over the intensity range investigated. However, the total integrated ion yield does scale as $\sim I^{1.3}$ for intensities above 7×10^{14} Wcm^{-2}, consistent with the increase in the focal volume, as was also found in the IR.

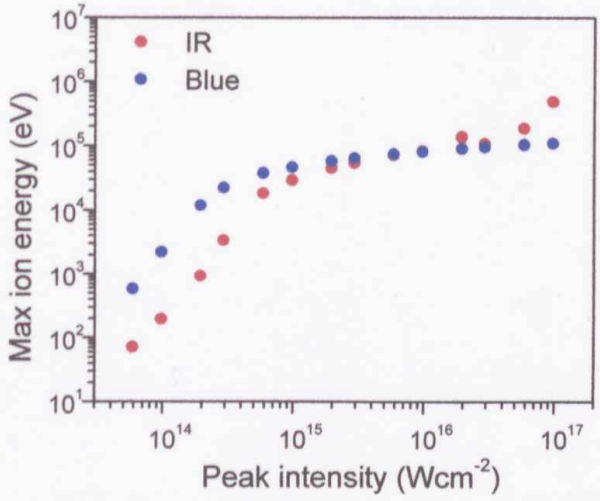


Figure 5.20. Calculated intensity dependence of the mean ion energy from clusters of 5300 Xe atoms irradiated by a 230 fs, 780 nm pulse (red) or a 160 fs, 390 nm pulse (blue) with a peak intensity between 10^{13} Wcm^{-2} and 10^{17} Wcm^{-2}.

In contrast, the nanoplasma model predicts that the scaling of mean ion energy with increasing laser intensity is very similar at both wavelengths, as shown in figure 5.20. With both wavelengths, the model predicts a sharp increase followed by a plateau where the mean ion energy is $\sim 3 \times 10^4$ eV. The onset of the plateau is at a lower intensity with the blue – at 2×10^{14} Wcm^{-2} compared to 6×10^{14} Wcm^{-2} in the IR – and the ion energies before the plateau are higher in the blue than the IR.

The wavelength scaling of the ion energies from cluster explosions are not well predicted by the nanoplasma model. It is still unclear whether this is a failure of the model or an experimental artefact. We have had considerable problems frequency-doubling the laser and have consistently found that the blue conversion efficiency is very much lower than we expect. This may mean that the width of the blue pulse is not $1/\sqrt{2}$ of the fundamental and/or that its shape does not follow the square of the fundamental as expected.

5.3.6 Dependence on cluster ion species

The nanoplasma model predicts that, for a given cluster size and laser pulse, the maximum ion energy scales as the square of the mean charge state achieved in the explosion (figure 5.11), which will depend on the species of ion in the cluster. We have examined the explosion of clusters of other rare gases to investigate how the explosion dynamics are dependent on atomic species. Our investigations have so far been confined to krypton and argon, as the lighter noble gases and hydrogen do not cluster very well.

Figure 5.21 shows ion energy spectra from Xe, Kr and Ar clusters with similar numbers of atoms per cluster (~ 1200), and from Ne with ~ 30,000 atoms per cluster. The

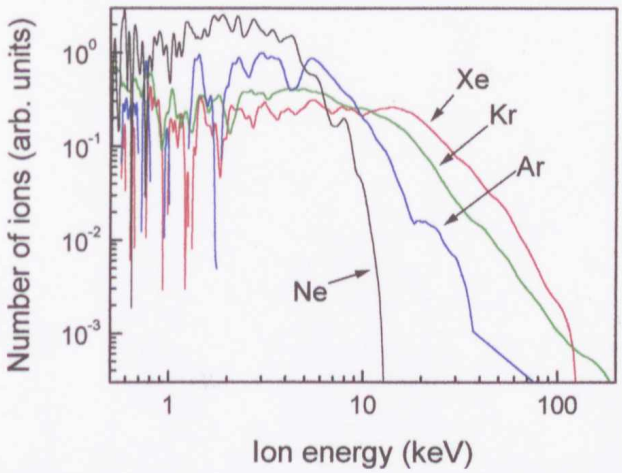


Figure 5.21. Ion energy spectra from Xe, Kr, Ar and Ne clusters. The gas-jet backing pressures and temperatures were 2 bar Xe at 300K (~1000 atoms), 4 bar Kr at 300 K (~1200 atoms) , 8 bar Ar at 300 K (~1500 atoms) and 12 bar Ne at 80 K (~ 29000 atoms). The laser intensity in each case was 1.3×10^{16} Wcm^{-2} for Xe, Kr and Ar, and 1.8×10^{16} Wcm^{-2} for Ne.

data shows that similar behaviour to that of Xe is observed in the explosion of Kr, Ar and Ne clusters, but that the explosion becomes less energetic as the atomic number is decreased. This is illustrated more quantitatively in Figure 5.22a, which shows the maximum ion energies from rare gas clusters as a function of cluster size. The mean ion energies follow a very similar trend.

The measured mean charge states (§5.3.2) were ~20+ in Xe and ~15+ in Kr for high

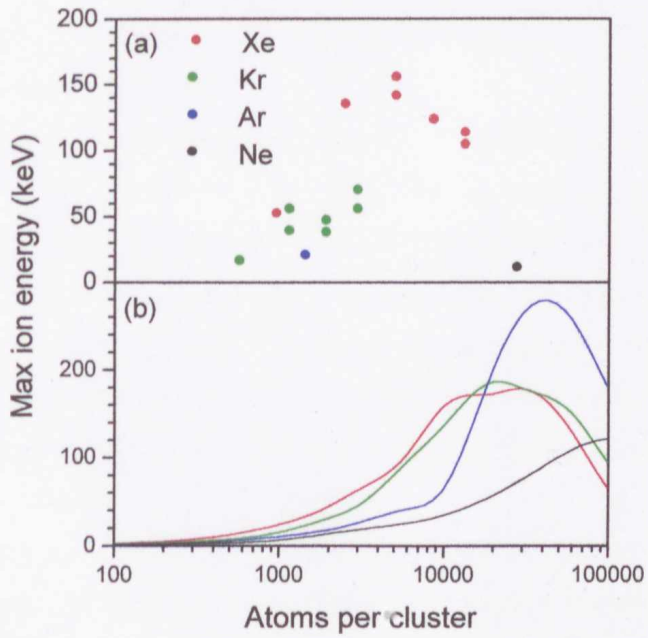


Figure 5.22. (a) Measured maximum ion energies from Xe (red), Kr (green), Ar (blue) and Ne (black) clusters with a variety of cluster sizes. The laser intensity was 1.3×10^{15} Wcm^{-2} for Xe, Kr and Ar and 1.8×10^{16} Wcm^{-2} for Ne. The Neon data was taken with gas-get LN_2 cooled to 80 K; Xe, Kr and Ar data taken at 300 K. (b) Calculated mean ion energy from clusters of Xe, Kr, and Ar and Ne atoms irradiated by a 170 fs, 780 nm pulse with a peak intensity of 1.3×10^{16} Wcm^{-2} .

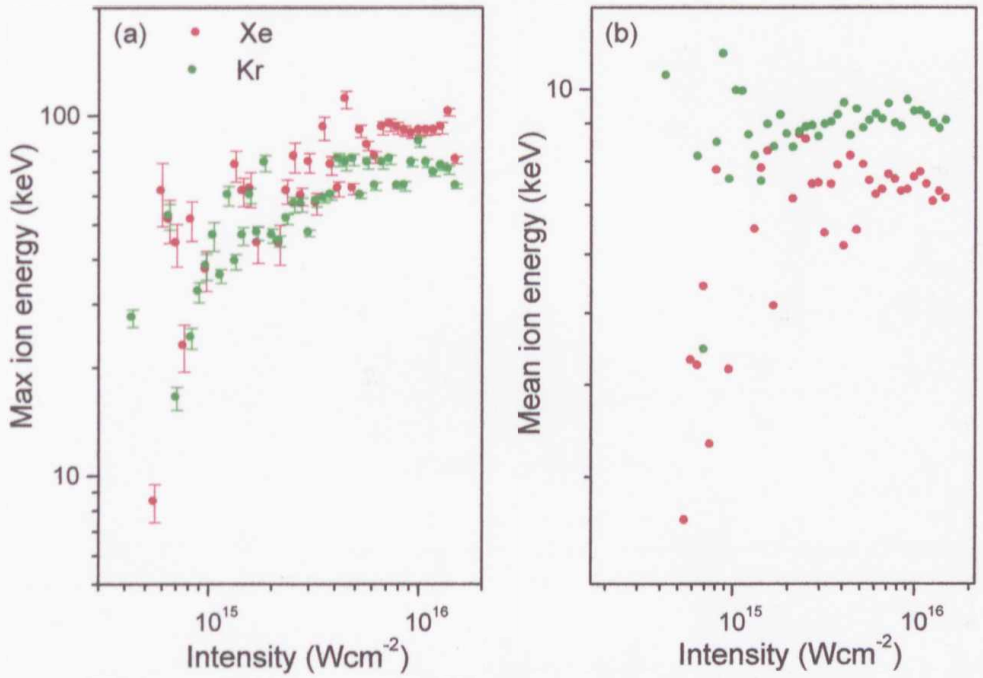


Figure 5.23. (a) Maximum and (b) mean ion energies measured as a function of laser intensity from 3×10^{14} Wcm^{-2} to 2×10^{15} Wcm^{-2} for 5300-atom Xe clusters and 6200-atom Kr clusters. The 780 nm laser pulse was 230 fs long (1997).

energy ions. The model predicts that the maximum ion energy should be proportional to the square of the mean charge state (figure 5.11), so we would expect the Xe ion energies to be $(20/15)^2 \approx 1.8$ higher than the Kr energies. At 3000 atoms/cluster, the ratio of energies is ~ 1.9:1. The measured ion energies and charge states are, therefore, roughly consistent with the Z^2 scaling predicted by the model.

Numerical calculations comparing the mean ion energy resulting from the explosion of Xe, Kr and Ar clusters irradiated by a 170 fs, 780 nm pulse with a peak intensity of 1.3×10^{16} Wcm^{-2} are presented in figure 5.22b. At low cluster sizes (<10,000 atoms) the mean ion energies from Xe clusters are ~ 5 keV higher than those from Kr clusters, and higher again than Ar clusters. It is this cluster size region that we have data for (figure 5.22a), and the trends in the data are consistent with the model. However, at much larger cluster sizes (>20,000 atoms) the model predicts that it is the Ar clusters which have the highest energy ions, followed by Kr and then Xe.

The dependence of ion energy on laser intensity of clusters of 6200 krypton atoms (41Å) has been compared with 5300-atom (43Å) xenon clusters (figure 5.23). The krypton ion energies follow a similar trend to the xenon, with a sharp increase up to a mean energy of 9 keV at 10^{15} Wcm^{-2} followed by a plateau. The maximum ion energies are lower in krypton than xenon (75 keV rather than 90 keV at 10^{16} Wcm^{-2}), but the mean energies are higher.

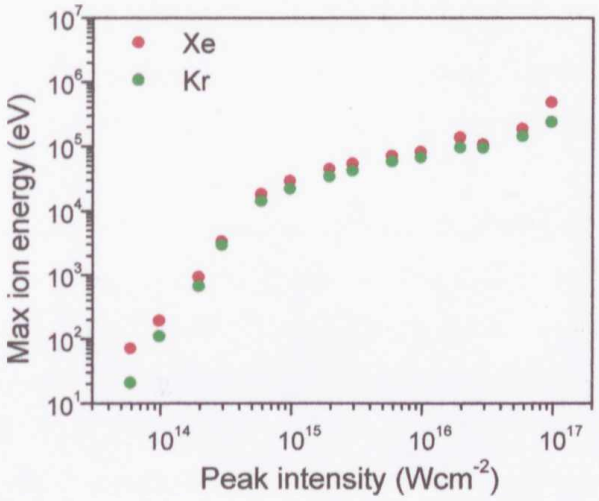


Figure 5.24. Calculated intensity dependence of the mean ion energy from clusters of 5300 Xe atoms (red) or 6200 Kr atoms (green) irradiated by a 230 fs, 780 nm pulse with a peak intensity between 10^{13} Wcm^{-2} and 10^{17} Wcm^{-2}.

The nanoplasma model (figure 5.24) predicts that xenon and krypton will exhibit very similar scalings with intensity with the laser and cluster parameters used in the experiment. The maximum ion energies from xenon are predicted to be higher than those from krypton (80 keV compared to 65 keV at 10^{16} Wcm^{-2}), consistent with the measured energies.

5.4 Discussion

The experiments described in this chapter represent the first direct measurements of the ion and electron energies from the explosion of large atomic clusters irradiated with high-intensity femtosecond laser pulses.

We found that the electron energies have a characteristic double-peaked distribution. The hot electron peak has a measured energy of up to 2.5 keV while the 'warm' electrons have energies from 100 eV to 2 keV. The nanoplasma model correctly predicts this double-peaked form of the spectrum, although the calculated temperatures are about a factor of three too high. The model suggests that the hot electrons are emitted after the electron density in the cluster has dropped below three times the critical electron density, at which point the collisional heating in the cluster is resonantly enhanced. The warm electrons are ejected before this period of collisional heating. This is consistent with our experimental findings that the hot electrons are emitted isotropically with respect to the direction of laser polarisation, while the warm electrons are preferentially emitted along the laser polarisation vector, as the velocity of the hot electrons will have been completely randomised by the collisional heating.

Several other groups have also investigated the interaction of large atomic clusters with high-intensity, femtosecond laser pulses. The x-ray yield from clusters has been measured by Dobosz *et al* [1997]. They found that the mean number of x-ray photons produced per laser shot scaled as $\sim (P - P_0)^3$ where P_0 is the pressure corresponding to onset of clustering. We found that hot electrons and hot (> 1 keV) ions (§5.3.3) were only observed when clusters of more than ~200 atoms were present in the gas-jet. X-rays, hot electrons and hot ions are then produced only when large clusters are present, indicating a change in the nature of the interaction once the cluster size reaches some critical threshold.

We have also measured ion energy spectra (§5.3) from the exploding clusters. The ion energy spectrum is very different from a Maxwellian, and also differs from the spectrum obtained directly from the nanoplasma model which assumes a uniform density, isotropic expansion. This suggests that, although the nanoplasma model may adequately describe the heating of the cluster, it is unable to describe the subsequent expansion of the plasma.

We have observed ions with energies up to 1 MeV from the explosion of 9000-atom Xe clusters. The mean ion energy was 91 keV in this case. Recently, x-ray spectroscopy of CO_2 cluster plasmas irradiated at 10^{18} Wcm^{-2} has also suggested that ions up to 1 MeV are produced [Dobosz 1998]. Hot, highly charged ions can even be produced when clusters are irradiated with long laser pulses at quite modest intensities. For example, Lezius*et al* [1997] irradiated Ar clusters with 30 ps laser pulses focused to 10^{14} Wcm^{-2} and reported Ar ions

stripped as far as 9^+ with energies of up to 5 keV – ion energies much higher than would be expected following simple Coulomb explosion of the clusters. The high energies and charge states were attributed to collisional ionisation of the cluster followed by hydrodynamic expansion.

These ion energies are much higher than those observed from the irradiation of molecules and small clusters at similar intensities. Energies of up to 55 eV have been observed in the Coulomb explosion of triatomic molecules [Cornaggia 1994], Hay and co-workers observed C^{4+} ions with energies up to 1 keV from the irradiation of C_{60} at intensities $\sim 5 \times 10^{15}$ Wcm^{-2} [Hay 1999], while Purnell [1994] observed 1 keV Ar^{8+} ions from $HIAr_n$ clusters with less than 10 Ar atoms at an intensity of 10^{15} Wcm^{-2}.

In contrast, the ion energies from the irradiation of solid targets at similar intensities and pulse-lengths are much lower as the plasma is cooled through conduction into the bulk solid, although some fast ions are blown off the target which can have energies of hundreds of keV [Meyerhofer 1993]. This suggests that energy is coupled much more efficiently into clusters than into solid targets. The energy absorption efficiency of short high intensity, laser pulses in a gas of atomic clusters can be extremely high and absorption fractions of up to 95% have been observed [Ditmire 1997d]. Absorption of greater than 90% has been measured from 'gold black', a low-average-density solid matrix of ~ 50 Å gold clusters, irradiated with 150 fs pulses at 10^{16} Wcm^{-2} [Murnane 1993]. In contrast, the absorption fraction in a (flat) solid target is much lower, in the region of 15% [Murnane 1991] to 40% [Kieffer 1989] at 10^{16} Wcm^{-2}.

Dobosz *et al* [1998] suggested that the mechanism for the generation of the MeV ions was ponderomotive acceleration of unclustered ions by standing waves set up between clusters. (They state that, under their operating conditions, only half the atoms in the expansion from the gas-jet would have condensed into clusters). However, their average ion density was 10^{19} cm^{-3} and we observed MeV ions at 10^{14} cm^{-3} (an inter-cluster spacing 50 times greater) which might suggest that the MeV ions result from the clusters themselves rather than the unclustered atoms between them.

We have also measured the ion charge states from xenon and krypton clusters (§5.3.2) and found that charge states much higher than those expected from over-the-barrier ionisation of single atoms at the same intensity were produced. Evidence for highly stripped ions had previously been found from x-ray spectroscopy of cluster plasmas [McPherson 1993, 1994ab, Ditmire 1995]. The nanoplasma model predicts the existence of high charge states through collisional ionisation in the near-solid density plasma. The ionisation ignition model (§2.2.3) predicts high charge states because of the lowering of the potential barriers due to the close presence of other charged cluster ions. The inner-shell ionisation model

(§2.2.4) also predicts that higher charge states will be observed in clusters than in monatomic gases due to collisional ionisation.

From a simple Coulomb explosion, the mean ion energy for a given charge state, $E(Z)$, scales as Z^2. Argon ions from small $HIAr_n$ clusters ($n \leq 10$) and Ar_m clusters ($m \leq 6$), which are assumed to undergo Coulomb explosion, follow the $E(Z) \sim Z^2$ pattern [Purnell 1994]. In contrast, a simple hydrodynamic expansion results in ions with energies given by $E(Z)=Zk_BT_e$. Lezius *et al* [1998] have measured ion charge states as a function of energy following the explosion of 10^5-atom Ar clusters and 10^6-atom Xe clusters, using magnetic deflection time-of-flight spectrometry. They observed that the energies of Ar and Xe ions with a charge of up to 6^+ - 8^+ scaled as Z^2. This was attributed to Coulomb explosion of the cluster. Most of the Xe ions with charges greater than 10^+ followed a hydrodynamic energy scaling with $T_e \sim 1.5$ keV, except for a high energy tail where $E(Z) \sim Z^2$. Our measurements (figure 5.9) show that the mean charge state is only a weak function of ion kinetic energy, with ions over 5 keV having a mean charge of 20^+ for Xe and 15^+ of Kr, suggesting the expansion is driven predominantly by hydrodynamic rather than Coulomb pressure.

We have also examined the scaling of ion energies with cluster size (§5.3.3). We find that the mean and maximum ion energies increase as the cluster size increases up to an optimum cluster size, from which point they drop. Zweiback *et al* [1999] have examined the relationship between cluster size and laser pulse length for optimal cluster heating. Measurements of the absorption and x-ray yield as a function of pulse width for various cluster sizes have confirmed that there is an optimum pulse-width for a given size of cluster, and that this optimum increases as the cluster size increases.

The nanoplasma model suggests that the dynamics of the cluster explosion is governed by the point in the laser pulse at which the electron density in the cluster falls through $3\ n_{critical}$, where the electron heating rate is dramatically enhanced. The highest ion temperatures are obtained when the cluster experiences this resonant heating close to the peak of the laser pulse. This explains the existence of an optimum cluster size for a given pulse length, and an optimum pulsewidth for a given cluster size. Small clusters expand more quickly and reach the $3\ n_{critical}$ point before the peak of the laser pulse, while if the clusters are too large they pass through this point well after the peak. If the pulsewidth is too short for the cluster size, $3\ n_{critical}$ is on the rising edge of the laser pulse, too long and $3\ n_{critical}$ is on the falling edge.

The existence of these optimum cluster sizes and pulselengths is an important finding in favour of the nanoplasma model. Coulomb explosion models predict that the ion energies increase monotonically as the cluster size increases [Last 1997]. Studies of the ionisation ignition mechanism indicate that the lowering of potential barriers due to the close presence of other charged ions, which leads to enhanced ionisation rates, increases as the

number of ions surrounding each ion increases [Hu 1997a]. However, for larger clusters the ionisation ignition model predicts little dependence on the degree of clustering as only the closest ions efficiently lower the ionisation potential of the ions within a cluster. The inner shell excitation and coherent electron motion models [McPherson 1993, Boyer 1994a] predict that, for a given intensity, there will be an allowed zone of cluster sizes for which x-ray emission from a given shell will occur, with the number of x-rays produced scaling as $(cluster\ size)^{4/3}$.

Snyder *et al* [1996] have studied the highly charged ions produced as atomic and molecular clusters were irradiated by femtosecond laser pulses at 10^{15} Wcm^{-2}. They observed multi-charge Kr ions only when a trace amount of HI was added to the Kr. This effect was also observed in Ar [Purnell 1994]. The authors [Snyder 1996b] attributed this effect to the presence of the iodine within the noble gas cluster lowering the barrier to ionisation in noble gas atoms and thus triggering ionisation ignition. However, highly charged ions have been observed from pure rare gas clusters by several other groups [for example, McPherson 1994a, Ditmire 1997a, Lezius 1998]. We believe that the presence of the highly polar HI molecule, which has a high condensation parameter [Tisch 1999], simply acted to enhance the degree of clustering in the gas-jet, meaning that highly charged ions were observed only from larger clusters.

A disadvantage of studying noble gas clusters is that their size and structure are not well defined. An alternative target is C_{60}, which can be regarded as a small carbon cluster. Studying C_{60} could also provides an indication of the cluster size at which the nanoplasma model becomes a valid description of the laser-cluster interaction. Wülker*et al* [1994] have observed x-ray production and lines corresponding to C^{5+} from the irradiation of C_{60} at 6×10^{15} Wcm^{-2}, findings that were attributed to collisional ionisation followed by expansion of the resulting plasma. (The over-the-barrier threshold for C^{4+} production is at 4×10^{15} Wcm^{-2}; that for C^{5+} is three orders of magnitude higher.) However, two sets of time-of-flight studies of C_{60} at similar intensities [Constantinescu 1998, Hay 1999] found no evidence of C^{5+} production. Ion energies of up to 1 keV were measured in both studies, but were found to be consistent with Coulomb explosion of C_{60} [Hay 1999], although C^{4+} was observed below the over-the-barrier threshold which suggests that electron impact ionisation may be occurring [Constantinescu 1998]. The C^{5+} discrepancy could be due to the way in which the C_{60} was produced. While the time-of-flight studies both used an oven to produce a molecular beam, Wülker *et al* used laser ablation which could produce large particles of C_{60} rather than individual molecules.

The effect of the laser intensity on the cluster explosion dynamics has also been examined (§5.3.4). We observed a sharp onset of hot ion production at a laser intensity of 6×10^{14} Wcm^{-2}. The mean and maximum ion energies increase rapidly as the laser intensity

is increased to 1×10^{15} Wcm^{-2}, from which point the ion energies increase only slowly. The integrated ion yield scales as $I^{1.4}$ for intensities above 1×10^{15} Wcm^{-2}, consistent with the increase in focal volume. This result is in good agreement with the numerical calculations of the nanoplasma model. The weak dependence of the cluster explosion dynamics on laser intensity at higher intensities has also been seen by Dobosz and co-workers [1997]. They performed x-ray spectroscopy of cluster nanoplasmas, calculated the mean number of x-ray photons emitted per laser pulse and found that it scales as $I^{3/2}$, again consistent with the increase in focal volume. For Kr clusters of 7×10^5 atoms, the explosion process was found to saturate below 4×10^{16} Wcm^{-2}.

Ditmire *et al* [1997e] measured the x-ray yields from Xe clusters as a function of laser intensity. They found that the yield of x-rays with energies above 1 keV scaled as $I^{2.4-3.0}$, and x-rays above 3 keV scaled as $I^{2.3-2.8}$ for laser intensities of $10^{16} - 10^{17}$ Wcm^{-2}. These results are only consistent with the intensity scalings found by us (§5.3.4) and Dobosz *et al* [1997] if the x-ray spectrum is shifting to shorter wavelengths as the intensity increases.

We have used the first and second harmonics of the Ti:Sapphire laser (at 780 nm and 390 nm) to examine the wavelength scaling of the cluster explosion dynamics (§5.3.5). We find that similar behaviour is found in the cluster explosion at both wavelengths. Again, there is an optimum cluster size for a given laser pulse and, as predicted by the nanoplasma model, the optimum cluster size is larger in the blue than the IR. However, we find that the intensity dependence of the ion energies at 390 nm is different to that at 780 nm, scaling as $I^{0.7}$ in the blue rather than the sharp increase followed by a levelling off as found for the IR and as predicted by the model.

The wavelength scaling of cluster dynamics has been examined by several groups. Kondo *et al* [1997] found that the x-ray yield from clusters was much lower at 800 nm than 248 nm. However, they compared results from two very different laser systems: 90 fs, 800 nm pulses at 1.4×10^{18} Wcm^{-2} from a Ti:Sapphire laser and 270 fs, 248 nm pulses from a KrF laser at 10^{19} Wcm^{-2}. Given the dependence of x-ray yield on pulse-length observed by Zweiback [1999], this is unlikely to be a fair study of the wavelength dependence. The authors claimed [Kondo 1997] that the nanoplasma model fails completely at 248 nm even if it is adequate at 800 nm. This is because collective effects (coherent electron motion) are predicted to have a dephasing time of ~1 fs (~ 1 optical cycle at 248 nm), and so will be much more important at 248 nm than at 800 nm, where an optical cycle is 2.7 fs. In contrast to these results, both Dobosz *et al* [1997] and Ditmire *et al* [1998b] found that there was no strong scaling of x-ray yield from first to second harmonic. Numerical calculations with the nanoplasma model indicate that there is no substantial change in the time history of the cluster dynamics when the wavelength of the radiation used to heat the cluster is varied from 250 nm to 1 μm.

We have studied the explosion of clusters of several different ion species and obtained similar spectra from Xe, Kr, Ar and Ne (§5.3.6). We find that, in general, the ion energies decrease as the atomic number decreases. Our numerical calculations which indicate that the maximum ion energy obtained scales roughly as the square of the mean charge state. This is consistent with our observation that the ratios of ion energies from Xe and Kr are roughly proportional to Z^2.

5.5 Conclusions

Our measurements of the ion and electron energies obtained from the explosion of clusters irradiated by intense, femtosecond laser pulses are in good agreement with the heating mechanisms of the nanoplasma model developed by Ditmire *et al* [1996]. In particular, the characteristic double-peaked electron spectrum supports the idea of sharp increase in the resonant heating at a particular electron density, and the existence of an optimum cluster size confirms the importance of the resonant heating occurring close to the peak of the laser pulse. More work is now needed to examine the variation of the electron spectrum with cluster and laser parameters. The expansion mechanism of the hot cluster plasma also needs further theoretical investigation, as the nanoplasma model is unable to calculate the shape of the ion energy spectrum.

The explosion of atomic clusters irradiated by a sequence of two high-intensity laser pulses

6.1 Introduction

In the previous chapter, we examined the interaction of clusters with single high-intensity laser pulses. We found that extremely energetic ions, with energies up to 1 MeV, and keV electrons are produced as the atomic clusters explode. The ions produced are also stripped to very high charge states. The interaction is more energetic than that with single atoms or small molecules at same intensity.

The nanoplasma model developed by Ditmire *et al* [1996], and described in detail in section 2.4, suggests that the cluster explosion is driven by an enhancement in the electron heating in the cluster. This enhancement occurs when the electron density in the cluster drops to three times the critical electron density ($3\,n_{critical}$), at which point the electric field in the cluster is greater than the vacuum electric field, there is a peak in the instantaneous electron temperature, and the cluster expansion velocity increases dramatically. The numerical model is in good qualitative agreement with our experimental results (§5.3 and [Ditmire 1998a]), successfully reproducing the trends in mean ion energy with cluster size, cluster ion species and laser intensity. The model also predicts a characteristic double-peaked electron spectrum, which has been observed experimentally (§5.2 and [Shao 1996]). The sharp 'hot electron' peak in the spectrum is due to electrons which leave the cluster at the $3\,n_{critical}$ resonance. The existence of an optimum cluster size for a given laser pulsewidth (§5.3.3) and an optimum pulsewidth for a given cluster size [Zweiback 1999] are also evidence of this resonance in heating, as the cluster size determines the time taken for the

electron density in the cluster to drop to $3n_{critical}$, and this point has to be near the peak of the laser pulse for optimal heating.

The nanoplasma model suggests that the explosion dynamics can be manipulated by irradiating the cluster with two laser pulses of different frequencies in sequence. The critical electron density is wavelength dependent, so the $3\,n_{critical}$ enhanced heating point will occur at a higher electron density for shorter wavelengths. This suggests that a cluster irradiated with two laser pulses of different frequencies will experience enhanced heating at two points in its expansion.

In this chapter, we present numerical simulations and experimental results which show a change in the cluster dynamics when the cluster is irradiated by two pulses of different frequencies in sequence. The cluster experiences two peaks in its heating and electron temperature, which leads to an increase in the energies of the ions produced in the explosion. We present experimental measurements of ion energies from Xe clusters irradiated with high-intensity femtosecond laser pulses, at the laser fundamental frequency (780 nm) and its second harmonic. The mean and maximum ion energies are found to depend on the relative delay of the two pulses but not on their relative polarisations. The mean ion energy is doubled for the optimum value of the delay between the two laser pulses [Springate 1998, 1999].

6.2 Numerical modelling of the two-colour interaction

6.2.1 Adapting the model to simulate cluster interaction with two pulses of different frequencies

The numerical model of the laser cluster interaction, described in section 2.4, has been adapted to simulate the irradiation of a cluster by two laser pulses with arbitrary frequencies, intensities and relative delays.

The tunnel and laser-driven ionisation rates (equations 2.8 and 2.11) are calculated, as in the one-colour case, from the instantaneous value of the electric field inside the cluster which is now the sum of the electric fields from the two pulses.

The heating is, as before, assumed to be through collisional heating of the electrons by the laser field (inverse Bremsstrahlung). The time-averaged energy-deposition rate (equation 2.14) in a two-colour field of frequencies ω_1 and ω_2 given by

$$E = E_1 e^{i\omega_1 t} + E_2 e^{i(\omega_2 t + \varphi)} + c.c \tag{6.1}$$

becomes

$$\frac{\partial U}{\partial t} = \frac{\omega_1}{8\pi} \mathrm{Im}[\varepsilon_1] |E_1|^2 + \frac{\omega_2}{8\pi} \mathrm{Im}[\varepsilon_2] |E_2|^2 . \tag{6.2}$$

There are no cross-terms in the time-averaged heating rate between the two fields: the total heating rate is just the sum of the heating rates due to the two individual fields. The field inside the cluster is then calculated from the external field by (from equation 2.16)

$$E = \frac{3}{|\varepsilon_1 + 2|} E_{01} + \frac{3}{|\varepsilon_2 + 2|} E_{02} . \tag{6.3}$$

The dielectric constant ε (equation 2.15) which is a function of optical frequency ω, plasma frequency ω_p and collision frequency ν is calculated for each laser wavelength. The collision frequencies (equations 2.6 and 2.18) are also treated separately for each field.

The rate of change of the ion temperatures is unchanged in a two-colour field, but the electron temperatures will now be given by (from equation 2.28)

$$\frac{\partial T_e}{\partial t} = -2\frac{T_e}{r}\frac{\partial r}{\partial t} - \frac{T_e - T_i}{\tau_{\text{equilibration}}} + \frac{2}{3n_e}\frac{\partial U_{\omega_1}}{\partial t} + \frac{2}{3n_e}\frac{\partial U_{\omega_2}}{\partial t} \tag{6.4}$$

as the electron heating rates from the two fields, $\partial U_{\omega_1}/\partial t$ and $\partial U_{\omega_2}/\partial t$, are added separately.

6.2.2 Numerical simulations of the explosion

The results of a numerical simulation of a xenon cluster irradiated by a 390 nm pulse coincident with a 780 nm pulse are shown in figures 6.1 to 6.4. As in the case of a cluster irradiated by a single laser pulse (section 2.4.8), a few free electrons are tunnel ionised early on in the laser pulse. The electron density rises through the $3\ n_{critical}$ for both frequencies, at which points the field in the cluster is enhanced and more electrons are liberated through tunnel, laser-driven and thermal ionisation. The electron density is then high enough to shield the field in the cluster from the external laser field. The tunnel and laser-driven ionisation rates fall off but electrons are still created through thermal ionisation.

The hydrodynamic pressure of the electrons causes the cluster to expand and this, combined with the free-streaming of some electrons out of the cluster, means that the electron density starts to drop. At t = -47 fs, the electron density (figure 6.1c) is

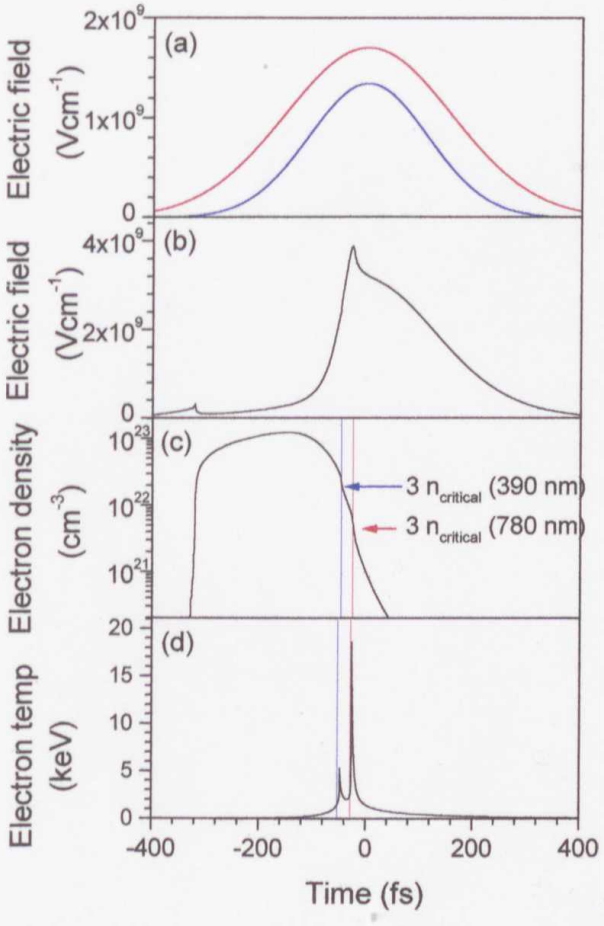


Figure 6.1. Numerical modelling of the interaction of a cluster of 14000 Xe atoms irradiated by a 185 fs, 390 nm pulse with a peak intensity of 2.5×10^{14} Wcm^{-2} and a 260 fs, 780 nm pulse with a peak intensity of 4.0×10^{15} Wcm^{-2}. The centres of the two pulses are coincident at t = 0 fs. (a) The envelope of the electric fields of the two individual pulses. (b) Electric field inside the cluster. (c) Electron density. (d) Electron temperature in the cluster. The blue and red vertical lines mark the points at which the electron density passes through $3\ n_{critical}$ for 390 nm and 780 nm respectively.

2.2×10^{22} cm^{-3}, three times the critical density for 390 nm radiation (this time is marked with a blue vertical line on all the plots). The increased heating rate at *3* $n_{critical}$ causes a peak in the electron temperature (figure 6.1d), coulomb and hydrodynamic pressures (figure 6.2a), radial acceleration (figure 6.2b) and free-streaming rate (figure 6.3b). 22 fs later, at t = - 25 fs, the electron density is *3* $n_{critical}$ for the 780 nm radiation (this time is indicated by a red line). The cluster again experiences a peak in the electron temperature, coulomb and hydrodynamic pressures, radial acceleration and free-streaming rate. The effect of the 'double kick' from the resonant heating from both fields is to increase the final ion energies to 148 keV (compared to 100 keV from just the IR pulse and 91 keV from the blue pulse alone).

The electron energy spectrum is also changed from the single-pulse case (compare figure 6.4 with figure 2.9). There are now two distinct hot electron peaks: one at 8.3 keV due

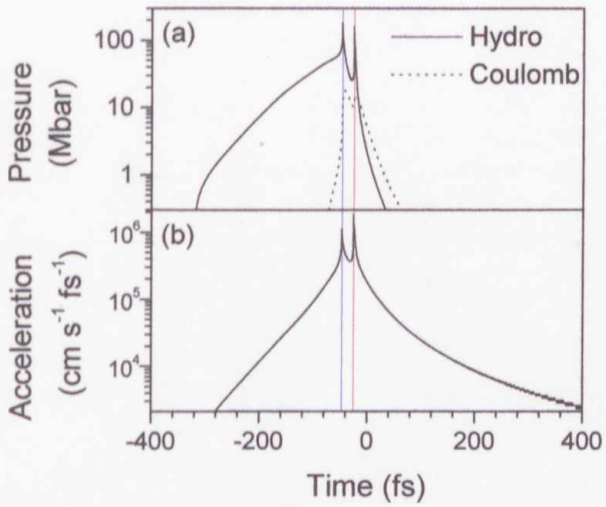


Figure 6.2. Numerical modelling of a cluster irradiated with two laser pulses with intensities and delays as in figure 6.1. (a) Hydrodynamic (solid line) and Coulomb (dotted line) pressure in the cluster. (b) Acceleration of the cluster radius.

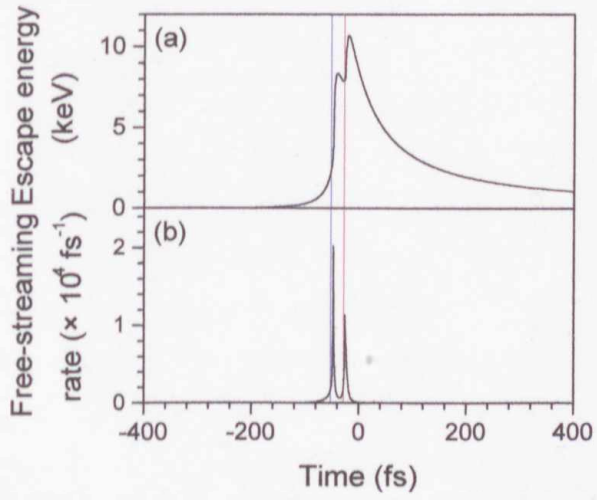


Figure 6.3. Numerical modelling of a cluster irradiated with two laser pulses with intensities and delays as in figure 6.1. The centres of the two pulses are coincident at *t* = 0 fs. (a) Escape energy. (b) Electron free-streaming rate.

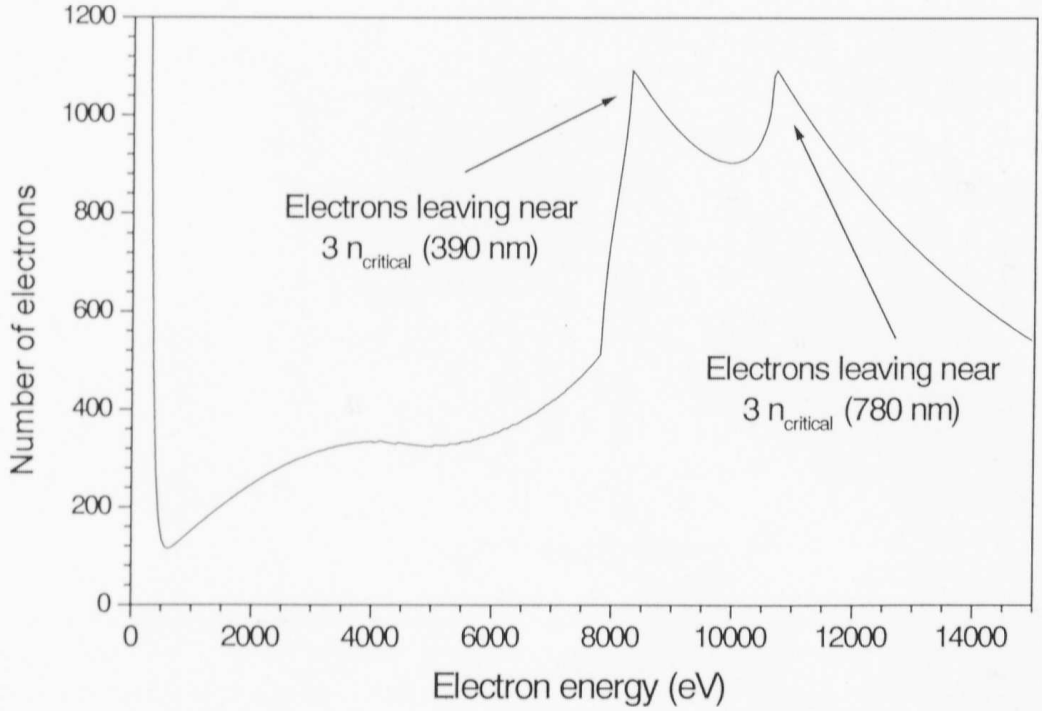


Figure 6.4. Calculated electron energy spectrum from a cluster of 14000 Xe atoms irradiated by a 185 fs, 390 nm pulse with a peak intensity of 2.5×10^{14} Wcm^{-2} and a 260 fs, 780 nm pulse with a peak intensity of 4×10^{15} Wcm^{-2} . The centres of the two pulses are coincident at t = 0 fs. The peak at 10.7 keV is due to electrons which leave the cluster near the point where the electron density passes through 3 $n_{critical}$ for 780 nm, and that at 8.3 keV is from electrons leaving near 3 $n_{critical}$ for 390 nm.

to electrons that leave the pulse at ~ –50 fs, near the $3\ n_{critical}$ point for the blue when the escape energy is up to 8.3 keV, and at 10.7 keV from electrons which leave near the – 25 fs IR $3\ n_{critical}$ point when the escape energy is up to 10.7 keV (figure 6.3a).

6.2.2.1 Relative delay of the two pulses

The effect on the electron energy spectrum of changing the relative delay between the blue and IR pulses is shown in figure 6.5. Throughout this chapter, the delay is defined as the separation between the peaks of the two pulses and $t = 0$ is at the centre of the IR pulse. A positive value of delay means that the IR pulse precedes the blue.

When the cluster is irradiated first by the blue pulse, then 1000 fs later by the IR (figure 6.5b) the explosion is essentially over by the time the IR pulse arrives, and the electron energy spectrum is very much the same as that due to the blue pulse alone (figure 6.5a). With a delay of –400 fs (figure 6.5c), a small peak appears in the spectrum at ~ 1 keV due to electrons which leave the cluster when the electron density reaches the $3\ n_{critical}$ point for the IR. At t = –200 fs (figure 6.5d), the electrons leaving at the $3\ n_{critical}$ point for both wavelengths have nearly the same amount of energy (~ 8 keV). The proportion of electrons in the hot peak also increases at this delay. The case when the two pulses are coincident (figure 6.5e) has been discussed in the previous section and is also shown in figure 6.4.

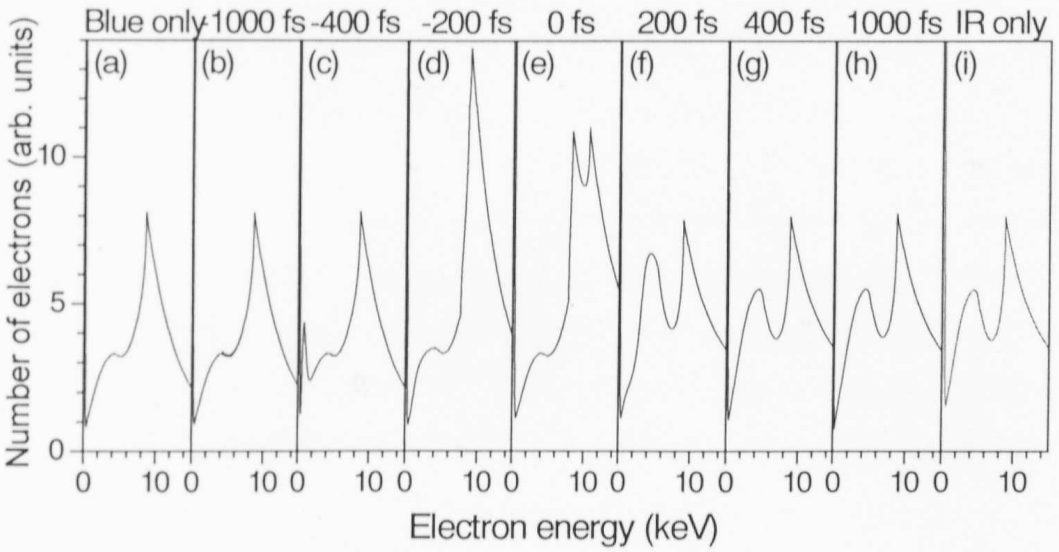


Figure 6.5. Calculated electron energy spectra from clusters of 14000 Xe atoms irradiated by a 260 fs, 780 nm pulse at 4×10^{15} Wcm^{-2} and a 185 fs, 390 nm pulse with a peak intensity of 2.5×10^{15} Wcm^{-2}. (a) shows the spectrum due to the 390 nm pulse alone, while (i) shows that from the 780 nm pulse alone. (b) to (h) show the change in electron energy spectrum as the delay between the two pulses is varied from –1 ps to +1 ps.

When the blue pulse arrives later than the IR (figure 6.5f), the change in electron energy spectrum is not so dramatic, and for delays of +400 fs or longer (figures 6.5g and h), the electron energy spectrum is essentially the same as that due to the IR pulse alone (figure 6.5i).

The final ion energies also depend on the relative delays of the two pulses (figure 6.6). In this example the maximum ion energies increase from 90 keV with the blue pulse alone and at large negative delays, or 100 keV from the IR pulse alone and at large positive

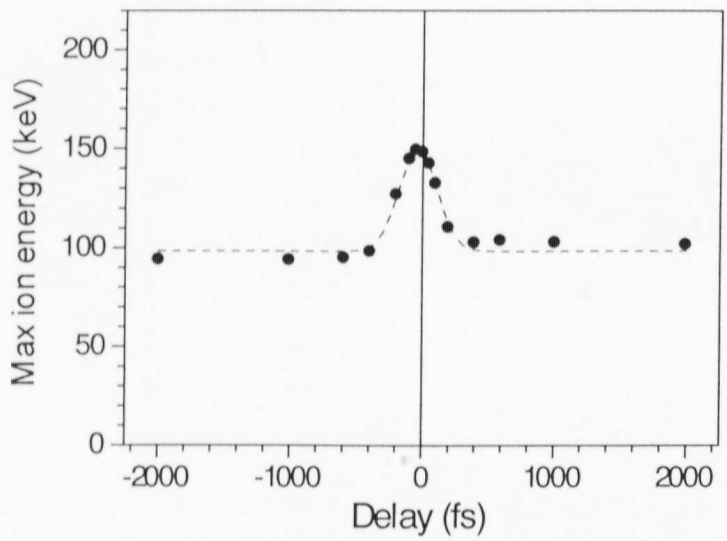


Figure 6.6. Calculated maximum ion energies from the irradiation of 14000 atom Xe clusters with one 780 nm, 260 fs, 4×10^{15} Wcm^{-2} pulse and one 390 nm, 185 fs, 2.5×10^{15} Wcm^{-2} pulse as the delay between the two pulses is varied. The maximum ion energy obtained with the 780 nm pulse alone was 100 keV. With the 390 nm pulse only, the maximum was 91 keV. The dashed line is a Gaussian fit to the points. The FWHM is 340 ± 25 fs and the centre is at –36 ± 8 fs.

delays to a maximum of 160 keV at a delay of ~ –25 fs. This is a significant enhancement of the ion energies at the optimal separation. Using only one pulse, an intensity of 1.1×10^{16} Wcm^{-2} at 780 nm or 2.5×10^{16} Wcm^{-2} at 390 nm is needed to produce 160 keV ions (figure 6.7) – a factor of nearly 3 higher in the IR and 10 times higher in the blue.

In all the sets of two-colour delay scans that have been modelled so far, the optimal delay has been found to be when the blue pulse precedes the IR by ~10 – 100 fs. Essentially, the final ion energies are optimised when the $3\ n_{critical}$ resonant heating point falls close to the peak intensity of each laser pulse. This condition is satisfied for a four times higher electron density at 390 nm than at 780 nm. As the electron density is *falling* through this resonant heating point, this means that the optimum delay is expected to be negative so that the blue pulse precedes the IR pulse.

6.2.2.2 Effect of the relative phase of the two laser pulses

These numerical calculations indicate that there is no significant variation in electron energy spectrum or final ion energy when the phase between the blue and IR pulses is varied. The relative phase of the two colours affects the initial numbers of electrons ionised through tunnel ionisation, through the change in the peak value of the electric field,

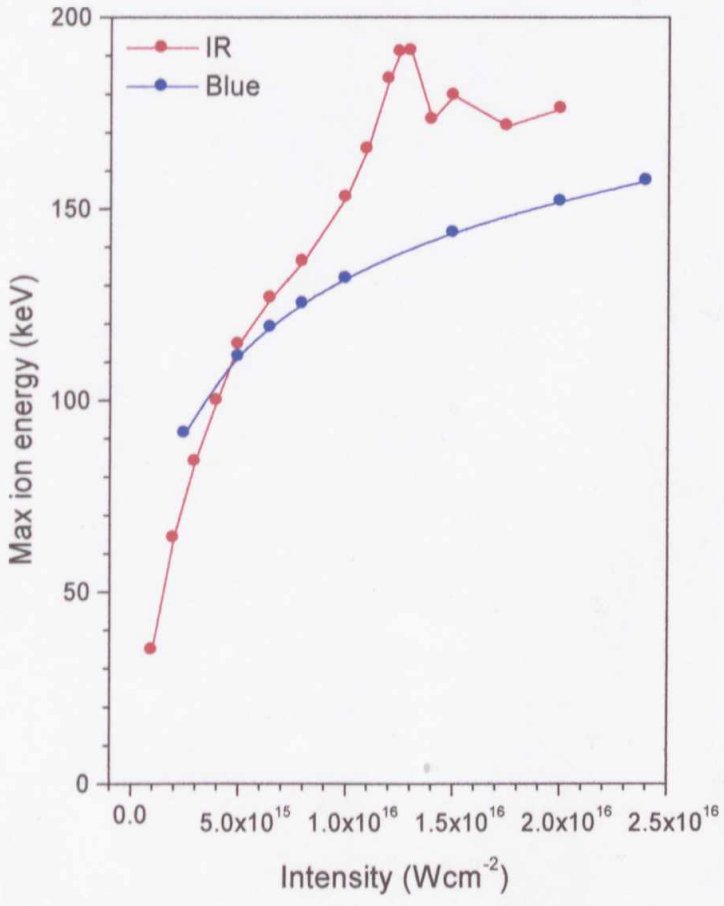


Figure 6.7. Calculated maximum ion energies from clusters of 14000 Xe atoms irradiated by a 260 fs, 780 nm pulse or a 185 fs, 390 nm pulse as the peak laser intensity is varied from 1×10^{15} Wcm^{-2} to 2.5×10^{16} Wcm^{-2}.

but this does not have a large effect on the explosion dynamics. There may, however, be changes in the angular dependence (relative to the laser polarisation) of the explosion as the total electric field is asymmetric, but the model is unable to predict this.

It would be extremely difficult to detect any phase effects in practice, due to the phase shift through the focus. Coherent control experiments examining phase effects rely on the extremely nonlinear character of the interaction studied, which means that particles produced at the highest intensity part of the focus form the dominant number of those detected [Muller 1990]. We cannot rely on this effect when studying cluster explosions, as the intensity dependence is much weaker (§5.3.4 and figure 6.7).

6.3 Experiment

6.3.1 Method

We have examined the ions produced in the interaction of Xe clusters with a sequence of two high-intensity, femtosecond laser pulses of different frequencies – the laser fundamental and its second harmonic. The laser pulses were focused down into a low-density beam of clusters and the energies of the ions produced in the interaction were determined from measurement of their flight time in a field-free drift tube (Chapter 4).

6.3.1.1 The two-colour delay line

The experimental set-up used to vary the relative delays, intensities and polarisations is shown in figure 6.8. The second harmonic was produced by frequency doubling in a 3 mm type 1 KDP crystal. The two beams were then separated by a dichroic beamsplitter and sent round separate paths before being recombined in the TOF spectrometer.

The conversion efficiency to second harmonic was extremely low (less than 5%) so we expected no significant change in the shape of the fundamental pulse after doubling [Krylov 1995]. The blue energy was controlled simply by varying the incident energy on the KDP crystal, and the IR energy was varied using a half-wave plate/polariser in the IR arm. The IR arm contained a translation stage which could be moved in steps of 5 μm (changing the path length by 10 μm) allowing a time resolution of 33 fs. The polarisations of the blue

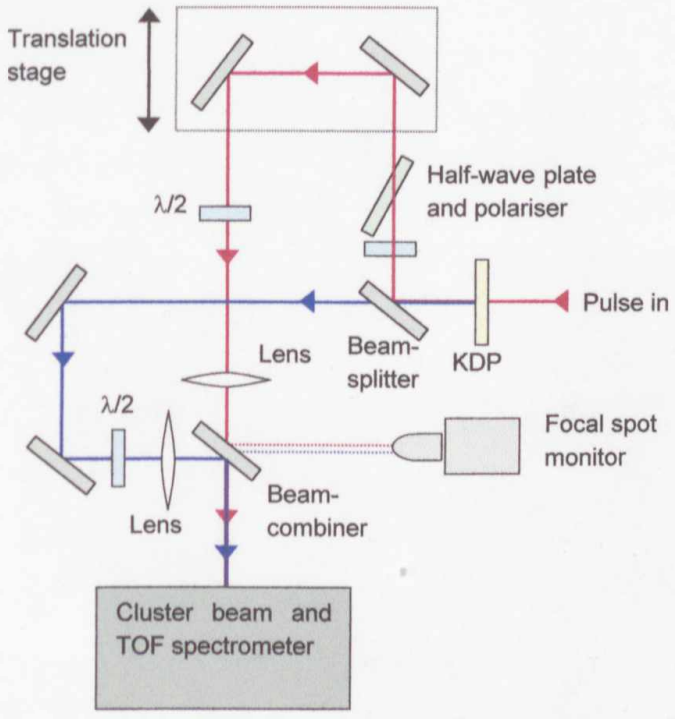


Figure 6.8 . Experimental set-up used to vary the relative delays, intensities and polarisations of the fundamental and second harmonic pulses.

and IR pulses were separately controlled by half-wave plates. These had a clear aperture of 40 mm and were the limiting aperture of the system in the vertical axis. The beams were clipped horizontally to less than 36 mm on passing through the 50 mm beamsplitters at 45°.

The blue and IR were focused separately by lenses with a focal length of 335 mm (IR) and 323 mm (blue). A focal spot monitor consisting of a ×40 microscope objective and CCD camera looking at the light leaking through the back of the final beam-combiner enabled us to ensure that the red and blue foci had not moved after initial alignment.

These experiments were carried out in 1998, so, at the exit of the compressor, the fundamental pulse was 255 fs and the second harmonic 180 fs long (table 3.2). Group velocity dispersion in the delay line increases both pulse-lengths by no more than 5 fs in the interaction region.

6.3.1.2 Spatial and temporal overlap of the two beams using N_2 breakdown

Spatial and temporal overlap of the IR and blue foci was obtained by filling the TOF chamber with dry N_2 until the pressure was high enough that the full power focused IR pulse caused a breakdown. This breakdown occurred at close to atmospheric pressure and was detected by the characteristic distortion of the beam at the exit of the chamber (figure 6.9b). The IR beam was then blocked and the blue intensity reduced by de-optimising the KDP crystal until the blue beam could propagate through the TOF chamber without causing a breakdown. Figure 6.9a shows the undistorted blue beam. The IR beam was then reintroduced into the chamber and the delay arm set so that the IR pulse preceded the blue. Spatial overlap could then be set by adjusting the final blue turning mirror until the blue beam was distorted at the exit of the chamber, as in figure 6.9c. This distortion was due to the blue beam propagating through the breakdown caused by the IR beam. Temporal overlap could then be set by moving the IR delay arm back until the distortion disappeared. We were able to consistently find temporal overlap to within 500 fs using this method. The relative *z*-positions of the two foci (adjusted by moving the lenses in the direction of laser propagation) could be set by looking at the spatial extent of the distortion across the blue beam. When the

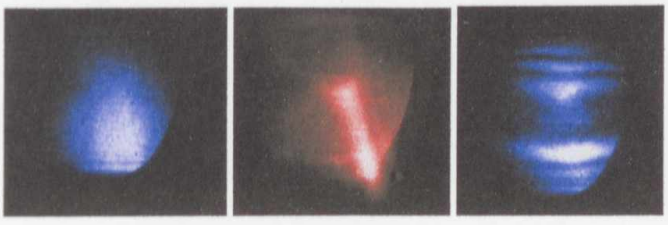


Figure 6.9. Using breakdown in N_2 to obtain spatial and temporal overlap of the red and blue foci. (a) Undistorted blue beam at the exit of the TOF chamber with the IR blocked. (b) IR beam at the exit of the TOF chamber showing distortion caused by breakdown in N_2. (c) Blue beam at the exit of the TOF chamber after it has passed through the plasma created by the IR focus. These are false-colour images.

foci were not overlapping in z, only a small portion of the blue beam was distorted on passing through the breakdown at the IR focus, but when they were coincident the entire beam was distorted.

The persistence of the distortion in the blue beam over 10 mm of IR translation stage movement indicated that the relative delay could be scanned over at least 66 ps without losing the overlap of the two foci.

6.3.1.3 Finding T-zero by looking at ionisation rates in Xe^{3+}

The translation stage position corresponding to zero time delay between the blue and IR pulses was found more accurately by looking at Xe^{2+} and Xe^{3+} ionisation rates. The TOF chamber was filled to a pressure of 2×10^{6} mbar with (monatomic) Xe and the blue and IR intensities were set to be separately just below the threshold for Xe^{3+} production (at $\sim 2.5 \times 10^{14}$ Wcm^{-2}). The blue and IR polarisations were set to be parallel (both horizontally polarised). The integrated Xe^{2+} and Xe^{3+} ion yields were then measured as a function of translation stage position (figure 6.10). Numerical integration of the ADK tunnelling

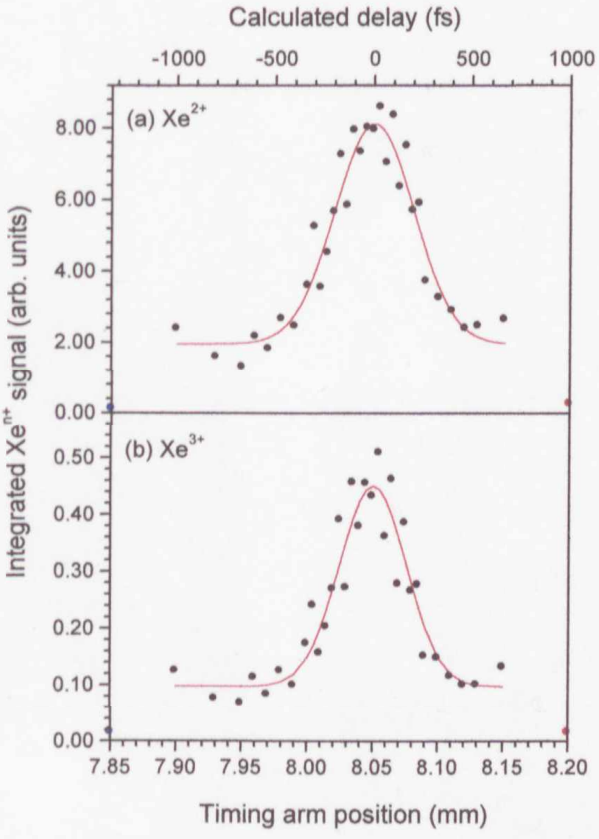


Figure 6.10. Measured ion yields of (a) Xe2+ and (b) Xe3+ as the delay between the blue and IR pulses is varied. The TOF chamber contained a static fill of Xe to a pressure of 2×10^{-6} torr. The blue intensity was 2.4×10^{14} Wcm^{-2} and the IR intensity was 2.7×10^{14} Wcm^{-2}. The red and blue points indicate the signal level with IR and blue alone. The red lines are Gaussian fits to the data. From the Xe^{2+} signal we obtain $T_0 = 8.050 \pm 0.001$ mm, and from the Xe3+ signal, $T_0 = 8.051 \pm 0.001$ mm. The error of 0.001 mm corresponds to 6.7 fs. The FWHM of the Gaussian fits are 475 ± 35 fs for Xe^{2+} and 400 ± 35 fs for Xe^{3+}

ionisation rates over the focal volume confirms that the ion yield peaks when the two pulses are coincident in time. By fitting a Gaussian to the data points, we were able to find T-zero (the position corresponding to zero delay) to ±0.001 mm, or ±6.7 fs.

6.3.2 Results

6.3.2.1 Varying the delay between the two pulses

We have obtained ion time-of-flight spectra from the explosion of 14,000-atom Xe clusters irradiated sequentially by 1.9 mJ ($\sim 0.6 \times 10^{15}$ Wcm^{-2}) at 780 nm and 1.3 mJ ($\sim 2.5 \times 10^{15}$ Wcm^{-2}) at 390 nm as the delay between the two pulses was varied (figure 6.11). The relative intensities of the blue and IR pulses were set to give approximately the same mean ion energy individually. Both the size and shape of the ion time-of-flight spectrum vary as the delay between the two pulses is varied. (As before, negative delay times mean the blue pulse is before the IR pulse). The optimum delay from this data appears to be at t = -200 fs. At this delay the peak of the spectrum shifts to earlier arrival times (corresponding to higher kinetic energies) and the total integrated ion yield is a maximum.

The mean and maximum ion energies calculated from the time-of-flight spectra are

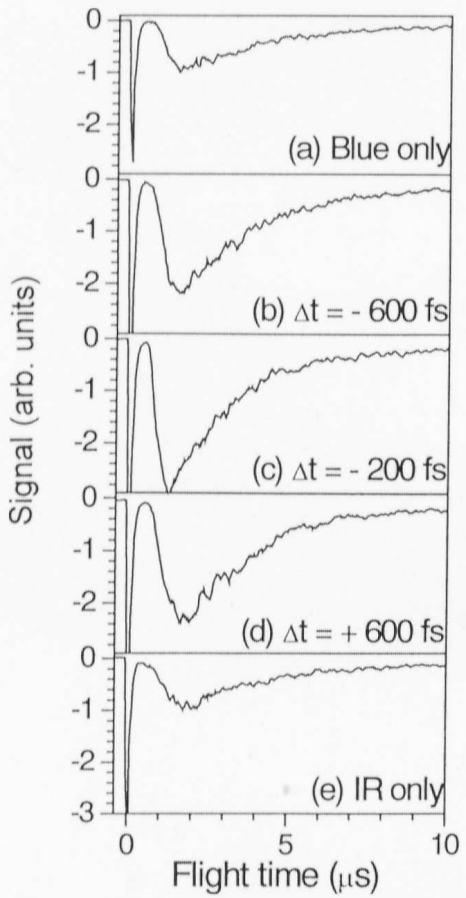


Figure 6.11. Measured ion TOF spectra from the irradiation of 14000-atom Xe clusters with a 780 nm and/or 390 nm laser pulse. (a) Blue pulse only. (b) Blue precedes IR by 600 fs. (c) Blue precedes IR by 200 fs. (d) Blue pulse 600 fs after IR. (e) IR pulse only. In each case the intensity of the 780 nm pulse was 6×10^{14} Wcm^{-2} pulse and that of the 390 nm pulse was 2.5×10^{15} Wcm^{-2}.

shown in figures 6.12a and b. Both the mean and the maximum ion energy vary with the delay between the two pulses for delays less than ~1 ps. The mean and maximum ion energy is approximately double that obtained with either pulse alone at the optimum delay. The mean and maximum cluster ion energies vary only weakly with incident laser intensity in this intensity range. For example, a laser energy of 5.75 mJ (~2×10^{15} Wcm^{-2}) at 780 nm is required to give mean ion energies of 30 keV. This is three times higher than the energy used in the two-colour experiment. The pulse energy required in the blue is well beyond the maximum we were able to obtain with our laser – we estimate it would require a factor of between 3 and 4 times higher intensity to produce ions with mean energies of 30 keV.

A Gaussian fit to the data points puts the optimum delay at -40 ± 35 fs or -60 ± 65 fs (blue pulse precedes the IR) from the mean and maximum ion energies respectively. The full width at half maximum of the fit is ~750 fs. For comparison, the results of the numerical

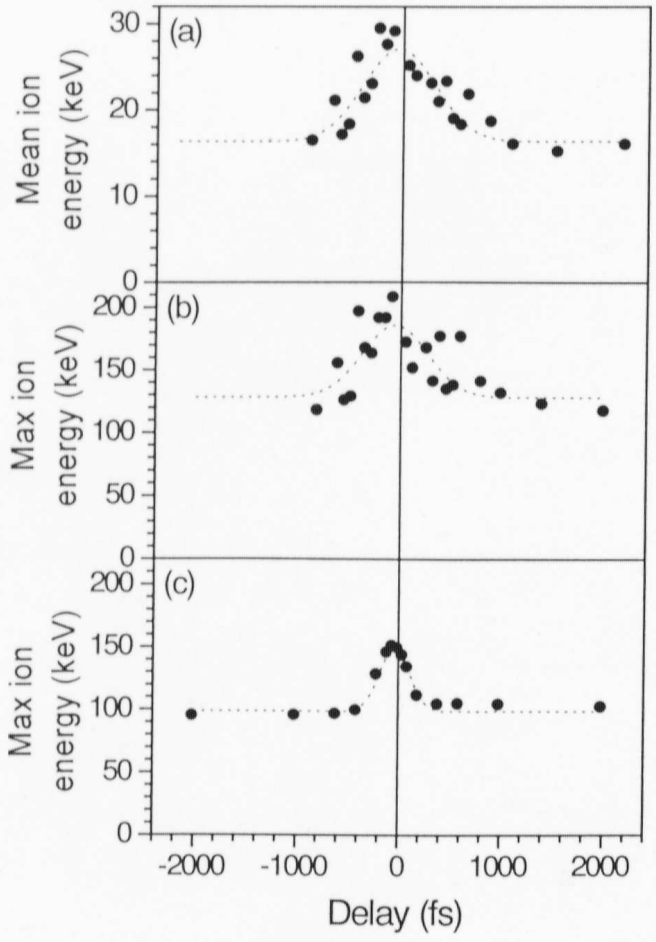


Figure 6.12. (a) Mean and (b) maximum ion energies measured from the irradiation of 14000 atom Xe clusters (6 bar Xe) with one 780 nm, 6 × 10^{14} Wcm^{-2} pulse (1.3 mJ) and one 390 nm, 2.5 × 10^{15} Wcm^{-2} pulse (1.9 mJ) as the delay between the two pulses is varied. The energies obtained with the 780 nm pulse alone were 14 keV mean and 143 keV max. With the 390 nm pulse alone, the mean was 19 keV and 140 keV the maximum. (c) Calculated ion energies. 14000 Xe atoms irradiated by 4 × 10^{15} Wcm^{-2}, 780 nm, 260 fs and 2.5 × 10^{15} Wcm^{-2}, 390 nm, 185 fs. The IR intensity was set at this value to match the measured maximum ion energies. The dotted lines are Gaussian fits to the data. (a)The centre of the fit is at –40 ±35 fs and the FWHM is 765 ± 130 fs, (b) centre at –60 ± 65 fs, FWHM 750 ± 200 fs, (c) centre at –36 ± 8 fs, FWHM 340 ± 25 fs.

model are shown in figure 6.12c.

The calculation uses the same cluster size, pulse lengths and blue intensity as we believe we used experimentally, but the IR intensity was adjusted to give an ion energy comparable with that due to the blue pulse. Our experimental calibrations suggested we had 6×10^{14} Wcm^{-2} at 780 nm, and the calculation uses a figure of 4×10^{15} Wcm^{-2}. Part of the discrepancy in the intensities could be due to errors in the experimental calibration. The red focal spot was quite large and an unusual shape due to the long path-length in optics in the delay line. The distorted focal volume may have hampered our ability to calibrate the intensity through the observation of the appearance of Xe^{n+} ion signal.

With the adjustment in intensity, the calculation successfully reproduces the trends in the experimental data. Both experiment and model can be fitted by a Gaussian with an optimum ion energy at a delay of ~ -40 fs. The measured enhancement in ion energies is 100%, better than the calculated 60%.

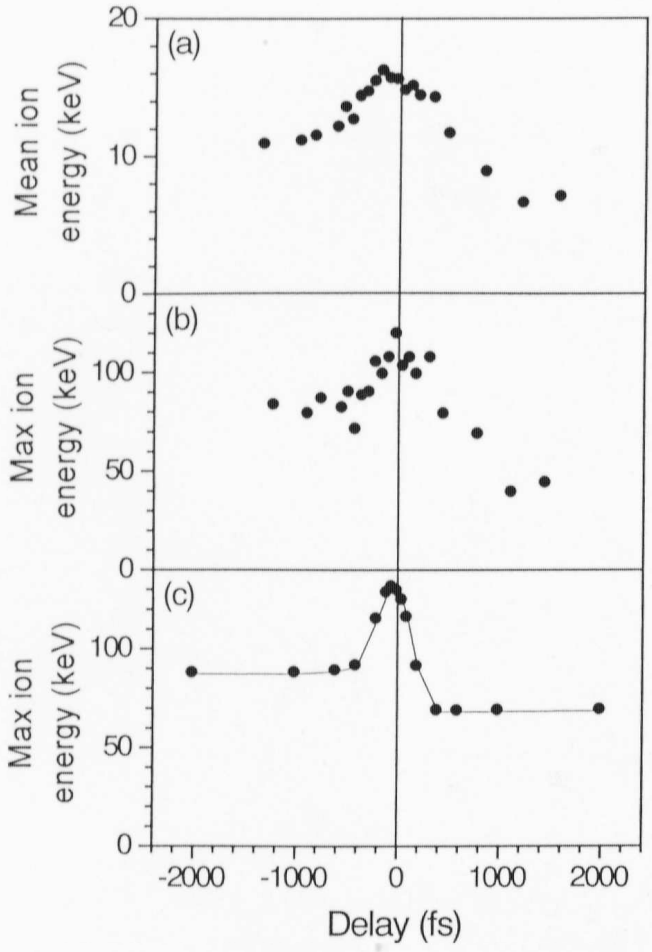


Figure 6.13. (a) Mean and (b) maximum ion energies measured from the irradiation of 14000 atom Xe clusters (6 bar Xe) with one 780 nm, 1.1 mJ pulse (~6×10^{14} Wcm^{-2}) and one 390 nm, 1.1 mJ pulse (~2.5×10^{15} Wcm^{-2}) as the delay between the two pulses is varied. With the 780 nm pulse alone the mean energy was 8 keV and the maximum was 40 keV. With the 390 nm pulse alone, the maximum was 80 keV. (c) Calculated max ion energies from a 14000-atom Xe cluster irradiated by 2×10^{15} Wcm^{-2}, 780 nm, 260 fs and 2×10^{15}, 390 nm, 185 fs. The IR intensity was set at this value to be consistent with that used in figure 6.10.

Figure 6.13 shows a second set of data from 14000 atom Xe clusters irradiated with 1.1 mJ at 780 nm (~4×10^{14} Wcm^{-2}) and 1.1 mJ at 390 nm (~2×10^{15} Wcm^{-2}). The mean ion energies (6.13a) increase from 11 keV when the blue precedes the IR by ~1400 fs to ~16 keV at a delay of –150 fs. The maximum ion energies follow a similar trend (6.13b). The results of the numerical model are shown in figure 6.13c. The intensities used in the calculation are consistent with those used in figure 6.12c. The calculation again successfully reproduces the trends in the experimental data, predicting a peak ion energy of 130 keV at a delay of –50 fs, compared to the 120 keV measured at –13 fs.

6.3.2.2 Effect of the relative polarisations of the two pulses

To gain further insight into the explosion mechanism with two pulses, we have compared the ion energies produced in the cluster explosion when the two laser fields have parallel and perpendicular polarisation (figure 6.14). To account for the slight anisotropy of the cluster explosion we have averaged over two orthogonal angles with respect to the direction of polarisation of the combined field. For example, the data for blue and IR

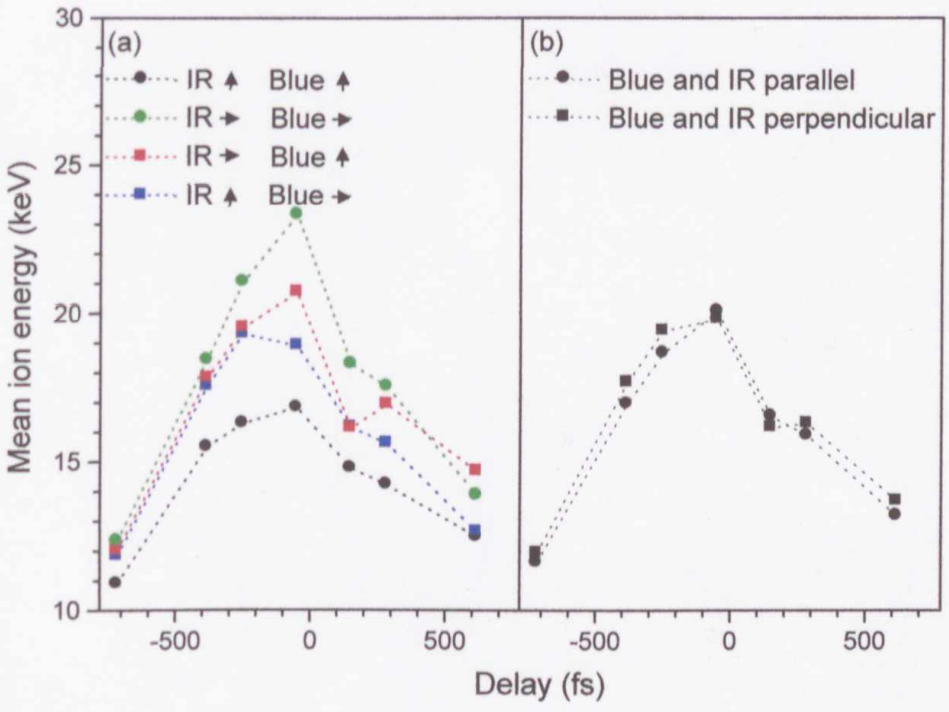


Figure 6.14.. Measured mean ion energies from the irradiation of 14000 atom Xe clusters with one 780 nm, 0.5×10^{15} Wcm^{-2} pulse and one 390 nm, 1.3×10^{15} Wcm^{-2} pulse as the delay between the two pulses is varied. Vertical polarisation means electric field is perpendicular to detection axis, with horizontal polarisation the electric field is parallel to the detection axis (a) Black circles: Blue and IR both vertically polarised. Green circles: Blue and IR both horizontally polarised. Red squares: IR horizontal, blue vertical. Blue squares: IR vertical, blue horizontal.(b) Circles: Blue and IR are polarised parallel to each other (average of green and black circles in (a)). Squares: Blue and IR are polarised perpendicular to each other (average of red and blue squares in (a)).

polarised parallel to each other is the average of data taken with both pulses polarised parallel to the detection axis, and both pulses polarised perpendicular to the detection axis.

The measured mean ion energies as a function of delay between the two laser pulses were found to be the same (to within the error on the mean ion energy) whether the blue and IR pulses had parallel or perpendicular polarisations. This implies that the explosion is not driven by a process that is strongly dependent on the peak value of the electric field (as tunnel ionisation is, for example).

6.4 Discussion

The measured mean ion energies were found to be the same whether the blue and IR pulses had parallel or orthogonal polarisations. This is consistent with the nanoplasma model, as the heating mechanism (collisional ionisation) is not strongly dependent on the peak electric field strength (equation 6.2). The tunnelling ionisation rate is, however, strongly dependent on the peak electric field strength. In the nanoplasma model, tunnelling ionisation is only important at the start of the explosion. It provides a seed for subsequent thermal collisional ionisation, but the final ion energies are not strongly dependent on the numbers of tunnel ionised electrons – as can be seen by the calculated lack of dependence on the relative phase of the two laser pulses. In contrast to this, the ionisation ignition model [Rose-Petruck 1997] rests on the enhancement of the tunnel ionisation rate due to the close proximity of other charged ions in the cluster. The tunnel ionisation rate will be significantly enhanced when the blue and IR fields have parallel polarisations compared to the case when they have orthogonal polarisations. We would expect the cluster dynamics to be different in the two cases, resulting in a difference in the final ion energies between the two cases.

Using two pulses of different frequencies to heat the cluster can provide a significant increase of the ion energies, as the ion energies have only a weak dependence on laser intensity (figure 6.7 and §5.3.4). To double the ion energy would require that the laser intensity be tripled. However, due to the very low conversion efficiency in the blue and the need to keep the blue and IR energies similar to ensure that the focal volumes were similar, the best ion energies we obtained using two colours were no higher than could be obtained using full-power IR (~17 mJ, 5×10^{15} Wcm^{-2}).

Experimental measurements of the electron energy spectra as a function of delay between the two pulses would provide further confirmation of the applicability of the nanoplasma model. We would expect to see two hot electron peaks in the spectrum, the energies of which would depend on the delay between the two pulses.

6.4.1 Cluster irradiation by two pulses of the same frequency

When the cluster is irradiated by two pulses with the same frequency, there is only one peak in the heating rate and only one hot electron peak in the electron energy spectrum. The final ion energies are dependent on the electric field strength at the $3\ n_{critical}$ resonant heating point and so will increase as the two laser pulses overlap in time. The explosion temperature is dependent on the relative phase of the two pulses when the two pulses overlap in time, as in this case the envelope of the electric fields changes (figure 6.15).

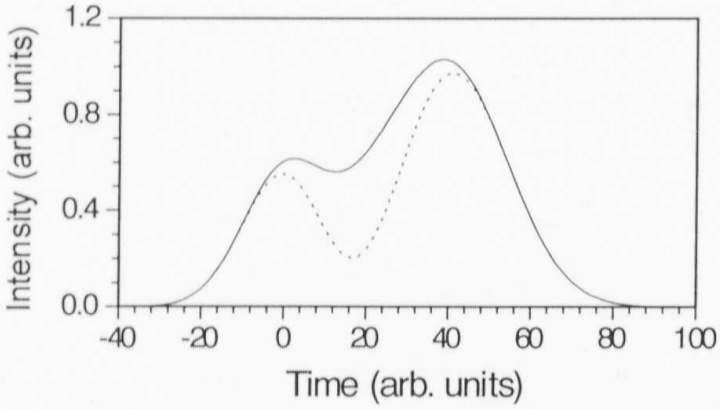


Figure 6.15. Intensity envelope from two pulses of the same frequency, one with ~ half the intensity of the other and relative phases of $\phi = 0$ (solid line) or $\phi = \pi$ (dashed line). (Pulsewidths 25 fs FWHM, delay 40 fs).

Zweiback *et al* [1999] have studied the disassembly of clusters irradiated by two pulses of the same colour in a pump probe experiment. They studied large Xe clusters (85 – 170 Å) irradiated by a 1.6×10^{16} Wcm^{-2} pump pulse and a 1.6×10^{17} Wcm^{-2} probe pulse, both at 810 nm with a 50 fs FWHM. They found that the absorption of probe radiation reaches a maximum for a particular time delay between pump and probe pulses and that this time depends on the cluster size. The optimum time is the time taken for the cluster to expand to the $3\, n_{critical}$ resonance condition.

It may also be possible to use two pulses of the same frequency with a controlled phase difference to optimise the explosion dynamics by effectively tailoring the shape of the electric field. The optimum shape of the electric field would probably be close to the shape of the electric field *inside* a cluster irradiated by a single pulse, so would have a small peak to start the ionisation followed by a low field to correspond to shielding of the electric field in the cluster, and then increase near the $3\, n_{critical}$ point. This is a different regime to that investigated by [Zweiback 1999] as the two pulses are separated by less than a pulsewidth.

6.5 Conclusions

In this chapter, we have presented numerical simulations and experimental results which show a change in the cluster dynamics when the cluster is irradiated by two pulses of different frequencies in sequence. The cluster experiences two peaks in its heating and electron temperature, which leads to an increase in the energies of the ions produced in the explosion.

We have measured experimentally the ion energies from Xe clusters irradiated at the laser fundamental frequency (780 nm) and its second harmonic. The mean and maximum ion energies are found to depend on the relative delay of the two pulses but not on their relative polarisations. The mean ion energy is doubled for the optimum value of the delay between the two laser pulses.

The calculations successfully reproduce the trends in the measured ion energies as the delay is varied, predicting the degree of enhancement and that the optimum ion energies will be produced when the blue pulse is approximately 50 fs before the IR pulse. These results support the idea that the cluster explosion is driven by an enhancement in the electron heating in the cluster which occurs when the electron density drops to three times the critical electron density.

Conclusions

7.1 Summary

This thesis has presented investigations of the interactions of clusters of $10^2 - 10^5$ atoms with high-intensity, femtosecond laser pulses. The experiments described in this thesis used a CPA Ti:Sapphire laser system, delivering 200 fs laser pulses at intensities of up to 10^{16} Wcm^{-2}. Studies of the interaction of intense laser pulses with clusters of atoms or molecules allow us to investigate the intermediate regime between laser-molecule and laser-solid interactions. Despite the fact that a cluster is very much smaller than a laser wavelength, it still behaves in many respects as a bulk solid target does. The ion and electron energies, and ion charge states, are very much higher than those produced from the irradiation of atoms or small molecules at the same intensity and comparable to those from solid targets.

A numerical model of the cluster as a spherical nanoplasma [Ditmire 1996] has been extensively tested against our experimental results. The model predicts that first the cluster is field ionised early on the rising edge of the laser pulse. As the cluster has near solid-density, the electron density in the cluster quickly rises to the point where the cluster is shielded from the external laser field and more electrons are created through collisional ionisation and are collisionally heated. The cluster starts to expand slowly due to the hydrodynamic pressure of the electrons, and some electrons are able to free-stream out of the cluster. The combined effect of the expansion and free-streaming is that the electron density starts to drop. When the electron density drops to three times the critical electron density, there is a dielectric enhancement of the field inside the cluster. This produces a sharp increase in the electron heating, which then leads to a very rapid expansion of the cluster.

The nanoplasma model predicts a characteristic two-peaked electron energy distribution, which we have observed experimentally (§5.2 and [Shao 1996]). The high ion

energies and charge states predicted have also been observed (§5.3 and [Ditmire 1997a, b]). Our experimental results successfully reproduce the theoretical variation in ion energy with cluster size (§5.3.3), cluster ion species (§5.3.6 and [Ditmire 1998a]) and laser intensity (§5.3.4). The existence of an optimum cluster size for a fixed laser pulsewidth (§5.3.3), and of an optimum pulsewidth for a given cluster size [Zweiback 1998] are also evidence for the $3\,n_{critical}$ resonance in the heating, as the cluster size determines the time taken for the electron density in the cluster to drop to this point and this has to be near the peak of the laser pulse for optimum heating.

To further test the validity of the nanoplasma model, we have studied the explosion of clusters sequentially irradiated by two pulses of different frequencies (Chapter 6 and [Springate 1998]). The nanoplasma model predicts that, as the resonant heating point will occur at a higher electron density for shorter wavelengths, a cluster irradiated by two pulses of different frequencies will experience enhanced heating twice in its expansion. Our experimental measurements confirm this prediction, reproducing the calculated variation of ion energy with delay between the two pulses. As expected, the delay for optimum heating occurs when the high frequency pulse precedes the low frequency pulse.

7.2 Further work and future directions

The experiments described in this thesis point towards several suggestions for future work, including improvements to the experimental techniques, further measurements to test the validity of the nanoplasma model, refinements of the modelling, and experiments using the energetic, highly stripped ions and hot plasma formed in the laser-cluster interaction. Some of these ideas are discussed in the following section.

7.2.1 Cluster size distribution measurements

The uncertainty on our measurement of the cluster sizes obtained through Rayleigh scattering experiments and evaluation of the Hagena parameter (§4.1) is approximately a factor of two (in the number of atoms). We are also uncertain about the distribution of cluster sizes, although a log-normal distribution with a width approximately equal to the mean cluster size has been measured by other groups [Gspann 1973, Lewerenz 1993, Karnbach 1993]. In order to reduce this uncertainty, we are currently carrying out time-of-flight studies on clusters which have been singly ionised with a nanosecond, UV laser pulse. This will enable us to more fully understand how sensitive the ion and hot electron energies are to the cluster size.

7.2.2 Self-similar expansions

Although the nanoplasma model is successful in predicting the electron energy spectrum and the variations of ion energies with cluster size, laser pulse-length and intensity, it is not able to model the ion energy spectrum. The self-similar solution of the ion fluid equations for an isotropic, radial expansion has been found for a Xe plasma with a Z of 20 and an electron temperature of 2.5 keV [Ditmire 1998a]. The calculated TOF trace and ion energy distribution are very close to those obtained from a 9000-atom Xe cluster, suggesting that the expansion is largely driven by hydrodynamic pressure. We now need to investigate how this solution varies with different electron temperatures and charge states and compare this with experimental measurements to determine whether it is a valid description of the cluster explosion.

7.2.3 Second peak in ion spectrum

Under some conditions (for example, figures 4.12 and 5.12), we observe a second, higher energy, peak in the ion spectrum at energies > 25 keV (corresponding to flight times of < 2 μs for Xe in a 38 cm flight tube). The MCP response peaks at this ion energy, but pulse-height analysis (figure 4.12) suggests that it may be a real effect rather than just an artefact of the MCP response. More detailed pulse-height analysis of this part of the spectrum (with higher oscilloscope resolution and more data-points per ion hit) will be needed to check whether this peak is real.

Wickens and Allen [1979] predicted an ion energy spectrum with two peaks would result from the self-similar expansion of a plasma with two electron temperatures. In this case, the free expansion of the hot electron component leads to the acceleration of the hot ions in the second peak, while the other electron component accelerates the less energetic ions which form the main peak. The authors predict that the relative size of the hot peak will be a sensitive function of the ratio of the two electron temperature, and of the fractions of electrons in each distribution. If pulse-height analysis shows that this second peak is real, an examination of its relation to the electron energy spectrum is called for.

7.2.4 Electron energy measurements

Further measurements of the electron energy spectra from exploding clusters are required, as the nanoplasma model predicts that the energy of the hot electron peak will vary as the laser pulse and cluster parameters are changed.

The electron energy measurements described in §5.2 were carried out by integrating the electron signal as the voltage on a set of retarding grids was varied, and then differentiating the resulting data-set. The differentiation can introduce a significant amount of noise into the data-set. An alternative way to measure the electron energy spectrum would

be to adapt the magnetic deflection time-of-flight technique which was used by Lezius *et al* [1998] to obtain charge state information. This technique uses a magnetic field perpendicular to the flight tube to deflect ions and electrons. Using a (time-integrated) imaging microchannel plate to detect the electrons, it should be possible to obtain an electron energy spectrum in just a few laser shots. We are now trying to build a magnetic defection electron spectrometer to add to our time-of-flight apparatus.

7.2.5 Molecular clusters

The nanoplasma model predicts that the maximum ion energy produced in the explosion depends (for a fixed number of atoms per cluster and laser pulse) on the square of the mean charge on the ions. We therefore expect that pure hydrogen clusters, which are limited to a mean charge of 1^+ compared to 20^+ for Xe clusters, will not produce multi-keV protons unless we go to extremely large cluster sizes. As hydrogen does not cluster well, a very high pressure (~50 kTorr), liquid helium cooled jet would be needed. In order to overcome this limitation, we have investigated the heating of hydrogen iodide clusters [Tisch 1999].

Although we are not yet able to simulate mixed species clusters with the nanoplasma model, the model does show that a pure iodine cluster would reach approximately the same temperature and charge state as a xenon cluster of the same size. However, we found that the ion energies from a 60,000-molecule HI cluster were comparable to those from a 5000-atom Xe cluster, with a maximum iodine energy of 90 keV and a mean of 9 keV. The iodine energies showed a monotonic increase with cluster size up to this point, which was the largest cluster size we could obtain. This indicates that the iodine energies from the HI clusters were lower than would be obtained from a pure iodine cluster of the same size. The degree of electron collisional heating should be the same for HI and pure I clusters (as the electron-proton equilibration time is longer than the time-scale of the heating). This suggests that the protons modify the dynamics of the cluster expansion, reducing the energy of the iodine ions.

We measured protons from 60,000 atom HI clusters with a mean energy of 250 eV and a maximum energy of 2.25 keV. The nanoplasma model predicts that to match these energies, much larger pure hydrogen clusters would be required. The irradiation of molecular clusters, such as HI, therefore enables us to produce energetic ions which do not cluster readily in their pure form and can potentially boost the energies of low-Z ions.

To enable us to discriminate between iodine and hydrogen ions with the same flight times pulse-height analysis was used. We obtained a pulse-height distribution for protons by using an extraction voltage to accelerate initially cold protons from the ionisation of contaminant H_20 out of the interaction region. Because of the technical difficulties in making

pure iodine clusters, we instead examined the pulse-height distributions of xenon clusters. The two distributions were markedly different: the xenon distribution was bi-modal, while the protons had a single peak. The TOF spectrum from HI clearly shows two groups of ion hits which are partially overlapping in time, but have pulse-height distributions closely similar to those from protons and Xe ions. This enables us to distinguish between H^+ and I^{q+} with the same flight times.

We are now planning future experiments on molecular clusters (in particular, deuterium iodide clusters). Pulse-height analysis will be indispensable in allowing us to differentiate between different ion species.

7.2.6 Highly stripped ions for particle accelerators

The high charge states in the explosion of atomic clusters has suggested the possibility of using a cluster source to provide highly stripped ions to accelerate in a particle accelerator. The mean charge state measured from Xe ions with energies of more than 10 keV was found to be 20^+ (figure 5.9). Two-thirds of all ions detected from clusters of 9000 Xe atoms had energies greater than this (although we only detect ions with energies above ~100 eV because of the finite length of the oscilloscope trace). Although the experiments described here used an average ion density of 10^{14} cm^{-3}, the ion density directly under the gas-jet is 10^{19} cm^{-3}. Experiments are planned which will allow us to quantify the absolute numbers of highly stripped ions that are produced in a cluster explosion.

7.2.7 Thermonuclear fusion

The hot plasma formed following the irradiation of a gas of clusters may make possible table-top fusion experiments. With 10^6-atom deuterium clusters irradiated by an 250 fs pulse at an intensity of 2×10^{16} Wcm^{-2}, the nanoplasma model predicts an ion temperature of ~25 keV. We assume that if fusion events occur, they will occur in the hot plasma produced after the clusters have disassembled. The ion density directly under the gas-jet would be ~10^{19} cm^{-3}, the plasma disassembly time is ~ 100 ps [Ditmire 1996] and the focal volume is ~ 10^{-6} cm^{-3}. The observable neutron yield under these conditions could be as much as 10^5 neutrons per shot [Teller 1981]. However, the Lawson criterion for energy breakeven requires that a 20 keV deuterium plasma be confined for 10^{15} s cm^{-3} [Beynon 1982], a factor of 10^6 higher than we can achieve.

Experiments to look for neutrons following the irradiation of deuterium clusters with intense laser pulses were pioneered here at Imperial College, but have so far been unsuccessful. Neutrons have now been observed in similar experiments [Ditmire 1999] using a 100 mJ, 35 fs table-top CPA laser system, indicating that nuclear fusion can occur in the hot plasma produced from exploding clusters. The yield was approximately 10^4 neutrons

per shot. This is equivalent to 10^5 neutrons per joule of laser energy – comparable to the yield from large-scale laser fusion experiments. This result opens up the possibility of carrying out laser-fusion experiments with laboratory-scale laser systems.

7.3 Conclusions

The irradiation of clusters with intense laser pulses will continue to be a fruitful area of research. The studies described in this thesis go some way towards allowing us to optimise the ion energies produced from exploding clusters, by showing how we can tailor the cluster size and ion species to a particular set of laser parameters. By using a sequence of two pulses of different frequencies, we were able to enhance the heating rate and vary the ion energies by changing the delay between the two pulses. This is just a small step towards being able to manipulate and control the dynamics of the explosion, and has enabled us to further examine the mechanism of the laser-cluster interaction.

References

A

Agostini 1988 P Agostini and G Petite, *"Photoelectric effect under strong irradiation"*, Contemp Phys **29** 57 (1988).

Ammosov 1986 MV Ammosov, NB Delone, and VP Krainov, *"Tunnel Ionisation of Complex Atoms and of Atomic Ions in an Alternating Electromagnetic Field"*, Sov Phys JETP **64** 1191 (1986).

Antonetti 1997 A Antonetti, F Blasco, JP Chambaret, G Cheriaux, G Darpentigny, C LeBlanc, P Rousseau, S Ranc, G Rey and F Salin, *"A laser system producing 5 × 10^{19} Wcm^{-2} at 10 Hz"*, Appl Phys B **65** 197 (1997).

Asaki 1993 MT Asaki, C-P Huang, D Garvey, J Zhou, HC Kapteyn and MM Murmane, *"Generation of 11-fs pulses from a self-mode-locked Ti-Sapphire laser"* Opt Lett **18** 977 (1993).

Augst 1989 S Augst, DD Meyerhofer, D Strickland, and SL Chin, *"Tunnelling ionisation of noble gases in a high-intensity laser field"*, Phys Rev Lett **63** 2212 (1989).

Augst 1991 S Augst, D Strickland, DD Meyerhofer, SL Chin and JH Eberly, *"Laser Ionisation of Noble Gases by Coulomb-Barrier Suppression"*, J Opt Soc B **8** 858 (1991).

B

Bell 1993 AJ Bell, JM Mestdagh, J Berlande, X Biquard, J Cuvellier, A Lallement, P Meynadier, O Sublemontier and J-P Visticot, *"Mean cluster size by Rayleigh scattering"*, J Phys D **26** 994 (1993).

Beynon 1982 TD Beynon, *"Laser Plasma Interactions 2"*, ed RA Cairns (Scottish Universities Summer School in Plasma Physics, 1982).

Blyth 1995 WJ Blyth, SG Preston, AA Offenburger, MH Key, JS Wark, Z Najmudin, A Modena, A Djaoui and AE Dangor, *"Plasma temperature in optical field ionisation of gases by intense ultrashort pulses of radiation"*, Phys Rev Lett **74** 554 (1995).

Borisov 1996 AB Borisov, A McPherson, K Boyer and CK Rhodes, *"Intensity dependence of the multiphoton induced Xe(L) spectrum produced by subpicosecond 248 nm excitation of Xe clusters"*, J Phys B: At Mol Opt Phys **29** L43 (1996).

Boyer 1994a K Boyer, BD Thompson, A McPherson and CK Rhodes, *"Evidence for coherent electron motions in multiphoton x-ray production from Kr and Xe clusters'*, J Phys B: At Mol Opt Phys **27** 4373 (1994).

Boyer 1994b K Boyer and CK Rhodes, *"Superstrong coherent multi-electron intense-field interaction"*, J Phys B: At Mol Opt Phys **27** L633 (1994).

Brewczyk 1998 M Brewczyk, CW Clark, M Lewenstein and K Rzążewski, *"Stepwise explosion of atomic clusters induced by a strong laser field"*, Phys Rev Lett **80** 1857 (1998).

Briant 1975 CL Briant and JJ Burton, *"Molecular dynamics study of the structure and thermodynamic properties of argon microclusters"*, J Chem Phys **63** 2045 (1975).

Brunner 1997 W Brunner, *"Intra-cluster ionisation and x-ray emission"*, Appl Phys B **64** 443 (1997).

Brunner 1998 W Brunner and H-H Ritze, *"Conditions for XUV amplification considering recombination in clusters"*, Appl Phys B **67** 47 (1998).

Buck 1996 U Buck and R Krohne, *"Cluster size determination from diffractive He atom scattering"*, J Chem Phys **105** 5408 (1996).

Burnett 1993 K Burnett, VC Reed and PL Knight, *"Atoms in ultra-intense laser fields"*, J Phys B: At Mol Opt Phys **26** 561 (1993).

C

Caruso 1969 A Caruso and R Gratton, *"Interaction of short laser pulses with solid materials"*, Plasma Phys **11** 839 (1969).

Castleman 1988 AW Castleman and RG Keesee, *"Gas-Phase Clusters: Spanning the States of Matter"*, Science **241** 36 (1988).

Codling 1989 K Codling, LJ Frasinski, PA Hatherly, *"On The Field-Ionisation Of Diatomic-Molecules By Intense Laser Fields"*, J Phys B: At Mol Opt Phys **22** L321 (1989).

Codling 1994 K Codling and LJ Frasinski, *"Coulomb Explosion of Simple Molecules in Intense Laser Fields"*, Contemp Phys **35** 243 (1994).

Constantinescu 1998 RC Constantinescu, S Hunsche, HB van Linden van den Heuvell, HG Muller, C LeBlanc and F Salin, *"Highly charged carbon ions formed by femtosecond laser excitation of C_{60}: a step towards an x-ray laser"*, Phys Rev A **58** 4637 (1998).

Corkum 1989 PB Corkum, NH Burnett and F Brunel, *"Above Threshold Ionisation in the Long-Wavelength Limit"*, Phys Rev Lett **62** 1259 (1989).

Cornaggia 1994 C Cornaggia, M Schmidt, and D Normand, *"Coulomb Explosion of CO_2 in an Intense Femtosecond Laser Field"*, J Phys B: At Mol Opt Phys **27** L123 (1994).

Coverdale 1995 CA Coverdale, CB Darrow, CD Decker, WB Mori, K-C Tzeng, KA Marsh, CE Clayton and C Joshi, *"Propagation of intense subpicosecond laser pulses through underdense plasmas"*, Phys Rev Lett **74** 4659 (1995).

Cuvellier 1991 J Cuvellier, P Meynardier, P de Pujo, O Sublemontier, J-P Visticot, J Berlande, A Lallement and J-M Mestdagh, *"A simple method to determine the mean cluster size in a molecular beam"*, Z Phys D **21** 265 (1991).

D

Darrow 1992 CB Darrow, C Coverdale, MD Perry, WB Mori, C Clayton, K Marsh and C Joshi, *"Strongly coupled Raman backscatter from subpicosecond laser-plasma interactions"*, Phys Rev Lett **69** 442 (1992).

De Martino 1993 A De Martino, M Menslimane, M Chatelet, C Crozes, F Pradere and H Vach, *"Average cluster size determination in supersonic beams from angular distribution measurements after scattering by a buffer gas"*, Z Phys D **27** 185 (1993).

Diels 1996 J-C Diels and W Rudolph, *"Ultrashort laser pulse phenomena: fundamentals, techniques, and applications on a femtosecond time scale"*, (San Diego London: Academic Press 1996).

Ditmire 1993 T Ditmire and MD Perry, *"Terawatt Cr-$LiSrAlF_6$ laser system"*, Opt Lett **18** 426 (1993).

Ditmire 1995 T Ditmire, T Donnelly, RW Falcone, and MD Perry, *"Strong X-ray Emission from High Temperature Plasmas Produced by Intense Irradiation of Clusters"*, Phys Rev Lett **75** 3122 (1995).

Ditmire 1996 T Ditmire, T Donnelly, AM Rubenchik, RW Falcone, and MD Perry, *"Interaction of Intense Laser Pulses with Atomic Clusters"*, Phys Rev A **53** 3379 (1996).

Ditmire 1997a T Ditmire, JWG Tisch, E Springate, MB Mason, N Hay, RA Smith, J Marangos, and MHR Hutchinson, *"High-Energy Ions Produced in Explosions of Superheated Atomic Clusters"*, Nature (London) **386** 54 (1997).

Ditmire 1997b T Ditmire, JWG Tisch, E Springate, MB Mason, H Hay, JP Marangos, and MHR Hutchinson, *"High Energy Ion Explosion of Super-Heated Clusters: Transition from Molecular to Plasma Behaviour"*, Phys Rev Lett **78** 2732 (1997).

Ditmire 1997d T Ditmire, RA Smith, JWG Tisch and MHR Hutchinson, *"High intensity laser absorption by gases of atomic clusters"*, Phys Rev Lett **78** 3121 (1997).

Ditmire 1997e T Ditmire, RA Smith, RS Marjoribanks, G Kulcsar and MHR Hutchinson, *"X-ray yields from Xe clusters heated by short pulse high intensity lasers"*, Appl Phys Lett **71** 166 (1997).

Ditmire 1998a T Ditmire, E Springate, JWG Tisch, YL Shao, MB Mason, N Hay, JP Marangos and MHR Hutchinson, *"Explosion of atomic clusters heated by high-intensity femtosecond laser pulses"* Phys Rev A **57** 369 (1998).

Ditmire 1998b T Ditmire, PK Patel, RA Smith, JS Wark, SJ Rose, D Milathianaki, RS Marjoribanks and MHR Hutchinson, *"keV x-ray spectroscopy of plasmas produced by the intense picosecond irradiation of a gas of xenon clusters"* J Phys B: At Mol Opt Phys **31** 2825 (1998).

Ditmire 1998c T Ditmire, *"Simulation of exploding clusters ionised by high-intensity femtosecond laser pulses"*, Phys Rev A **57** R4094 (1998).

Ditmire 1999 T Ditmire, J Zweiback, VP Yanovsky, TE Cowan, G Hays and KB Wharton, *"Nuclear fusion from explosions of femtosecond-laser heated deuterium clusters"*, Nature (London) **398** 489 (1999).

Dobosz 1997 S Dobosz, M Lezius, M Schmidt, P Meynardier, M Perdrix and D Normand, *"Absolute keV photon yields from ultrashort laser-field-induced hot nanoplasmas"*, Phys Rev A **56** R2526 (1997).

Dobosz 1998 S Dobosz, M Schmidt, M Perdrix, P Meynardier, O Gobert, D Normand, AYa Faenov, AI Magunov, TA Pikuz, IYu Skobelev, and NE Andreev, *"Characteristic features of the x-ray spectra of a plasma produced by heating CO_2 clusters by intense femtosecond laser pulses with λ = 0.8 and 0.4 μm"*, JETP Letters **68** 485 (1998).

E

Eder 1994 DC Eder, P Amendt, LB DaSilva, RA London, BJ MacGowan, DL Matthews, BM Penetrante, MD Rosen, TD Donnelly, RW Falcone and GL Strobel, *"Tabletop x-ray laser"*, Phys Plasmas **1** 1744 (1994).

F

Faldon 1992 ME Faldon, *"A high intensity, short pulse neodymium laser"*, PhD thesis, University of London (1992).

Farges 1986 J Farges, MF de Feraudy, B Raoult and G Torchet, *"Non-crystalline structure of argon clusters II Multilayer icosahedral structure of ArN clusters 50 < N < 750"*, J Chem Phys **84** 3491 (1986).

Fork 1987 RL Fork, CH Brito-Cruz, PC Becker and CV Shank, *"Compression of optical pulses to six femtoseconds by using cubic phase compensation"*, Opt Lett **12** 483 (1987).

Fraser 1996 DJ Fraser and MHR Hutchinson, *"A high-intensity titanium-doped sapphire laser"*, J Mod Opt **43** 1055 (1996).

Frasinski 1994 LJ Frasinski, PA Hatherly, K Codling, M Larsson, A Persson, CG Wahlstrom, "Multielectron Dissociative Ionization of CO_2 in Intense Laser Fields", J Phys B: At Mol Opt Phys **27** L109 (1994).

Freeman 1987 RR Freeman, PH Bucksbaum, H Milchberg, S Darack, D Schumacher and ME Geusic, *"Above-threshold ionisation with sub-picosecond laser pulses"*, Phys Rev Lett **59** 1092 (1987).

French 1995 PMW French, *"The Generation Of Ultrashort Laser-Pulses"*, Rep Prog Phys **58** 169 (1995).

G

Gibbon 1996 P Gibbon and S Forster, *"Short-pulse laser-plasma interactions"*, Plasma Phys Control Fusion **38** 769 (1996).

Gitomer 1996 SJ Gitomer, RD Jones, F Begay, AW Ehler, JF Kephart, and R Kristal, *"Fast Ions and Hot Electrons in the Laser-Plasma Interaction"*, Phys Fluids **29** 2679 (1986).

Glover 1994 TE Glover, TD Donnelly, EA Lipman, A Sullivan and RW Falcone, *"Subpicosecond Thompson Scattering Measurements of Optically Ionized Helium Plasmas"*, Phys Rev Lett **73** 78 (1994).

Gspann 1973 J Gspann and K Korting, *"Cluster beams of hydrogen and nitrogen analysed by time-of-flight mass spectrometry"*, J Chem Phys **59** 4726 (1973).

Gspann 1982 J Gspann, *"Electronic and atomic impacts on large clusters"* in *"Physics of Electronic and Atomic Collisions"* ed S Datz (North Holland Publishing Company, 1982).

Guethlein 1996 G Guethlein, ME Foord and D Price, *"Electron temperature measurements of solid density plasmas produced by intense ultrashort laser pulses"*, Phys Rev Lett **77** 1055 (1996).

H

Hagena 1972 OF Hagena and W Obert, *"Cluster formation in expanding supersonic jets: effect of pressure, temperature, nozzle size and test gas"*, J Chem Phys **56** 1793 (1972).

Hagena 1991 OF Hagena, *"Cluster ion sources"*, Rev Sci Inst **63** 2374 (1992).

Hay 1999 N Hay, E Springate, M B Mason, J W G Tisch, M Castillejo and J P Marangos, *"Explosion of C_{60} irradiated with a high-intensity femtosecond laser pulse"*, J Phys B: At Mol Opt Phys **32** L17 (1999).

Haught 1970 AF Haught and DH Polk, *"Formation and heating of laser irradiated solid particle plasmas"*, Phys Fluids **13** 2825 (1970).

Hu 1997a SX Hu and ZZ Xu, *"Enhanced harmonic emission from ionized clusters in intense laser pulses"*, Appl Phys Lett **71** 2605 (1997).

Hu 1997b SX Hu and ZZ Xu, *"Dynamics of an intense laser-driven multiwell system: a model of ionized clusters"*, Phys Rev A **56** 3916 (1997).

I

J

Jackson 1975 JD Jackson, *"Classical Electrodynamics"*, (New York: John Wiley & Sons 1975).

K

Karnbach 1993 R Karnbach, M Joppien, J Stapelfeldt and J Wörmer, *"CLULU: An experimental setup for luminescence measurements on van der Waals clusters with synchrotron radiation"*, Rev Sci Inst **64** 2838 (1993).

Keldysh 1965 IV Keldysh *"Ionisation in the field of a strong electromagnetic wave"*, Sov Phys JETP **20** 1307 (1965).

Kerker 1969 M Kerker, *"The scattering of light and other electromagnetic radiation"*, (Academic Press, New York London 1969).

Kieffer 1989 JC Kieffer, P Audebert, M Chaker, JP Matte, H Pepin, TW Johnston, P Maine, D Meyerhofer, J Delettrez, D Strickland, P Bado and G Mourou, *"Short-pulse laser absorption in very steep plasma density gradients"*, Phys Rev Lett **62** 761 (1989).

Klauder 1960 JR Klauder, AC Price, S Darlington and WJ Albersheim, *"The theory and design of chirp radar"*, Bell Syst Tech J **4** 745 (1960).

Koechner 1992 W Koechner, *"Solid-state laser engineering"*, 3rd ed, (Springer-Verlag 1992).

Kondo 1997 K Kondo, AB Borisov, C Jordan, A McPherson, WA Schroeder, K Boyer and CK Rhodes, *"Wavelength dependence of multiphoton-induced Xe(M) and Xe(L) emissions from Xe clusters"*, J Phys B: At Mol Opt Phys **30**, 2707 (1997).

Kruer 1988 WL Kruer, *"Physics of Laser Plasma Interactions"*, (Addison-Wesley 1988).

Krylov 1995 V Krylov, A Rebane, AG Kalintsev, H Schwoerner and UP Wild, *"Second-harmonic generation of amplified femtosecond Ti:Sapphire laser pulses"*, Opt Lett **20** 198 (1995).

L

Landau and Lifshitz 1960 LD Landau and EM Lifshitz, *"Electrodynamics of continuous media"*, (Pergamon Press: Oxford 1960).

Last 1997 I Last, I Scheck and J Jortner, *"Energetics and dynamics of Coulomb explosion of highly charged clusters"*, J Chem Phys **107** 6685 (1997).

Last 1998 I Last and J Jortner, *"Theoretical study of dissociative ionisation of diatomic molecules and clusters in a strong laser field"*, Phys Rev A **58** 3826 (1998).

LeBlanc 1996 C LeBlanc, P Curley and F Salin , *"Gain-narrowing and gain-shifting of ultra-short pulses in Ti:sapphire amplifiers"*, Opt Comms **131** 391 (1996).

Lemoff 1993 E Lemoff and CPJ Barty, *"Quintic-phase-limited, spatially uniform expansion and compression of ultrashort optical pulses"*, Opt Lett **18** 1651 (1993).

Lewerenz 1993 M Lewerenz, B Schilling and JP Toenies, *"A new scattering deflection method for determining and selecting the sizes of large liquid clusters of $_4He$"*, Chem Phys Lett **206** 381 (1993).

Lezius 1997 M Lezius, S Dobosz, D Normand and M Schmidt, *"Hot Nanoplasmas from Intense Laser Irradiation of Argon Clusters"*, J Phys B: At, Mol Opt Phys **30** L251 (1997).

Lezius 1998 M Lezius, S Dobosz, D Normand and M Schmidt, *"Explosion dynamics of rare gas clusters in strong laser fields"*, Phys Rev Lett **80** 261 (1998).

Lotz 1968 W Lotz, *"Electron-Impact Ionisation Cross-Sections and Ionisation Rate Coefficients for Atoms and Ions from Hydrogen to Calcium"*, Z Phys **216** 241 (1968).

M

Maine 1988 P Maine, D Strickland ,P Bado ,M Pessot and G Mourou , *"Generation of ultrahigh peak power pulses by chirped pulse amplification"*, IEEJ Quant Elec **24** 398 (1988).

Martinez 1987 E Martinez, *"Design of ultrashort pulse amplifiers by expansion and recompression"*, IEEJ Quant Elec **23** 1385 (1987).

Mason 1999 MB Mason, *"A sub-50 fs Titanium-Sapphire Chirped Pulse Amplification Laser System"*, PhD Thesis, University of London (1999).

Matthews 1995 DL Matthews, *"Review of x-ray lasers"*, Nucl Inst Methods Phys Res B **98** 91 (1995).

McPherson 1993 A McPherson, TS Luk, BD Thompson, K Boyer, and CK Rhodes, *"Multiphoton-Induced X-Ray Emission and Amplification from Clusters"*, App Phys B **57** 337 (1993).

McPherson 1994a A McPherson, BD Thompson, AB Borisov, K Boyer, and CK Rhodes, *"Multiphoton-induced X-Ray Emission at 4-5 keV from Xe Atoms with Multiple Core Vacancies"*, Nature (London) **370** 631 (1994).

McPherson 1994b A McPherson, TS Luk, BD Thompson, AB Borisov, OB Shiryaev, X Chen, K Boyer, and CK Rhodes, *"Multiphoton Induced X-Ray Emission from Kr Clusters on M-Shell and L-Shell Transitions"*, Phys Rev Lett **72** 1810 (1994).

McPherson 1996 A McPherson, A B Borisov, K Boyer and C K Rhodes, *"Competition between multiphoton xenon cluster excitation and plasma wave Raman scattering at 248 nm"*, J Phys B: At Mol Opt Phys, **29** L291 (1996).

Meyerhofer 1993 DD Meyerhofer, H Chen, JA Delettrez, B Soom, S Uchida, and B Yaakobi, *"Resonance Absorption in High-Intensity Contrast, Picosecond Laser-Plasma Interactions"*, Phys Fluids B **5** 2584 (1993).

Meyer-ter-Vehn 1997 J Meyer-ter-Vehn, *"Prospects of inertial confinement fusion"*, Plasma Phys Control Fusion **39** B39 (1997).

Mohideen 1993 U Mohideen, MH Sher, HWK Tom, GD Aumiller, OR Wood II, RR Freeman, J Bokor, and PH Bucksbaum, *"High Intensity Above-Threshold Ionization of He"*, Phys Rev Lett **71** 509 (1993).

Moulton 1986 PF Moulton, *"Spectroscopic and laser characteristics of Ti:Al_2O_3"*,J Opt Soc Am B **3** 125 (1986).

Muller 1990 HG Muller, PH Bucksbaum, DW Schumacher and A Zavriyev, *"Above-threshold ionisation with a two-colour laser field"*, J Phys B: At Mol Opt Phys **23** 2761 (1990).

Murnane 1988 MM Murnane and RW Falcone, *"High-power femtosecond dye-laser system"*, J Opt Soc Am B **5** 1573 (1988).

Murnane 1989 MM Murnane, HC Kapteyn and RW Falcone, *"High-density plasmas produced by ultrafast laser pulses"*, Phys Rev Lett **62** 155 (1989).

Murnane 1991 MM Murnane, HC Kapteyn, MD Rosen, and RW Falcone, *"Ultrafast X-ray Pulses from Laser-Produced Plasmas"*, Science **251** 531 (1991).

Murnane 1993 MM Murnane, HC Kapteyn, SP Gorgon, J Bokor, EN Glytsis and RW Falcone, *"Efficient coupling of high-intensity subpicosecond radiation into solids"*, Appl Phys Lett **62** 1068 (1993).

N

Nuckolls 1972 J Nuckolls, L Wood, A Thiessen and G Zimmerman, *"Laser compression of matter to super-high densities: Thermonuclear (CTR) Applications"*, Nature (London) **239** 139 (1972).

O

P

Panofsky 1978 WKH Panofsky and M Phillips, *"Classical Electricity and Magnetism"*, (Addison-Wesley London 1978).

Patterson 1991 FG Patterson, MD Perry and J Weston, *"Spectral shaping in chirped-pulse amplification"*, J Opt Soc Am B **8** 2384 (1991).

Paulus 1994 GG Paulus, W Nicklich, H Xu, P Lambropoulos, and H Walther, *"Plateau in Above Threshold Ionisation Spectra"*, Phys Rev Lett **72** 2851 (1994).

Payne 1989 SA Payne, LL Chase, LK Smith, WL Kway and HW Newkirk, *"Laser Performance Of $LiSrAlF_6$-Cr^{3+}"*, J Appl Phys **66** 1051 (1989).

Perelomov 1966 AM Perelomov, VS Popov and MV Terentev, *"Ionisation of atoms in an alternating electric field"*, Sov Phys JETP **23** 924 (1966).

Perry 1990 MD Perry and FG Patterson, *"Spectral Shaping In Chirped-Pulse Amplification"*, Opt Lett **15** 381 (1990).

Perry 1994 MD Perry and G Mourou, *"Terawatt To Petawatt Subpicosecond Lasers"*, Science **264** 917 (1994).

Pessot 1987 M Pessot, P Maine and G Mourou, *"1000 times expansion/compression of optical pulses for chirped pulse amplifiers"*, Opt Comm **62** 419 (1987).

Protopapas 1997 M Protopapas, CH Keitel, PL Knight, *"Atomic physics with super-high intensity lasers"*, Rep Prog Phys **60** 389 (1997).

Purnell 1994 J Purnell, EM Snyder, S Wei, and AWCastlemaN Jr, *"Ultrafast Laser-Induced Coulomb Explosion of Clusters with High Charge States"*, Chem Phys Lett **229** 333 (1994).

Q

R

Reid 1998 DT Reid and W Sibbett, *"Commercial semiconductor devices for two-photon absorption auto-correlation of ultrashort light pulses"*, Appl Optics **37** 8142 (1998).

Rexer 1997 EF Rexer, RL DeLeon and JF Garvey, *"Metastable and collision induced Coulomb explosion of doubly charged ammonia cluster ions"*, J Chem Phys **107** 4760 (1997).

Rose-Petruck 1997 C Rose-Petruck, KJ Schafer, KR Wilson, and CPJ Barty, *"Ultrafast Electron Dynamics and Inner-Shell Ionisation in Laser Driven Clusters"*, Phys Rev A **55** 1182 (1997).

S

Shao 1996 YL Shao, T Ditmire, JWG Tisch, E Springate, JP Marangos, and MHR Hutchinson, *"Multi-keV Electron Generation in the Interaction of Intense Laser Pulses with Xe Clusters"*, Phys Rev Lett **77** 3343 (1996).

Sheehy 1996 B Sheehy and LF DiMauro, *"Atomic and molecular dynamics in intense optical fields"*, Annu Rev Phys Chem **47** 463 (1996).

Shepherd 1994 R Shepherd, D Price, W White, S Gordan, A Osterheld, R Walling, W Goldstein, and R Stewart, *"Characterisation of Short Pulse Laser-Produced Plasmas"*, J Quant Spec Rad Trans **51** 357 (1994).

Siegman 1986 AE Siegman, *"Lasers"*, (University Science Books 1986).

Silin 1965 VP Silin, *"Non-linear High-Frequency Plasma Conductivity"*, Sov Phys JETP **20** 1510 (1965).

Smith 1998 RA Smith, T Ditmire and JWG Tisch, *"Characterisation of a cryogenically cooled high pressure gas jet for cluster production"*, Rev Sci Inst **69** 3798 (1998).

Snyder 1996 EM Snyder, SA Buzza, and AW Castleman, *"Intense Field-Matter Interactions: Multiple Ionisation of Clusters"*, Phys Rev Lett **77** 3347 (1996).

Spence 1991 DE Spence, PN Kean and W Sibbert, *"60-fsec pulse generation from a self-mode-locked Ti:sapphire laser"*, Opt Lett **16** 42 (1991).

Spitzer 1962 L Spitzer, *"Physics of fully ionised gases"*, (Interscience: New York London 1962).

Springate 1998 E Springate, N Hay, JWG Tisch, MB Mason, JP Marangos, MHR Hutchinson and T Ditmire, *"High-temperature explosion of atomic clusters irradiated by a sequence of two high-intensity laser pulses"*, in *International Quantum Electronics Conference*, OSA Technical Digest Series **7**, 39 (Optical Society of America, Washington DC 1998).

Springate 1999 E Springate, N Hay, JWG Tisch, MB Mason, T Ditmire, JP Marangos and MHR. Hutchinson, *"Enhanced explosion of atomic clusters irradiated by a sequence of two high-intensity laser pulses"*, submitted to Phys Rev Lett (1999).

Strickland 1985 D Strickland and G Mourou, *"Compression of amplified chirped optical pulses"*, Opt Comm **56** 219 (1985).

Svelto 1989 O Svelto, *"Principles of Lasers"*, (Plenum 1989).

T

Teller 1981 E Teller, *"Fusion"*, (Academic: New York 1981).

Thompson 1994 BD Thompson, A McPherson, K Boyer and CK Rhodes, *"Multi-electron ejection of inner-shell electrons through multiphoton excitation of clusters"*, J Phys B: At Mol Opt Phys **27** 4391 (1994).

Tisch 1999 JWG Tisch, N Hay, E Springate, ET Gumbrell, MHR Hutchinson and JP Marangos, *"Measurement of ion energies from the explosion of large hydrogen iodide clusters irradiated by intense femtosecond laser pulses"*, submitted to Phys Rev Lett.

Treacy 1969 EB Treacy, *"Optical pulse compression with diffraction gratings"*, IEEJ Quant Elec **5** 454 (1969).

U

V

W

Walker 1994 B Walker, B Sheehy, LF DiMauro, P Agostini, KJ Schafer, and KC Kulander, *"Precision Measurement of Strong Field Double Ionisation of Helium"*, Phys Rev Lett **73** 1227 (1994).

White 1993 WE White, FG Patterson, RL Combs, DF Price and RL Shepherd, *"Compensation Of Higher-Order Frequency-Dependent Phase Terms In Chirped-Pulse Amplification Systems"*, Opt Lett **18** 1343 (1993).

Wickens 1979 LM Wickens and JE Allen, *"Free Expansion of a Plasma with Two Electron Temperatures"*, J Plas Phys **22** 167 (1979).

Wörmer 1989 J Wörmer, V Guzielski, J Stapelfeldt, and T Möller, *"Fluorescence Excitation Spectroscopy of Xenon Clusters in the VUV"*, Chem Phys Lett **159** 321 (1989).

Wülker 1994 C Wülker, W Theobald, D Ouw, FP Schäfer, and BN Chichkov, *"Short-Pulse Laser-Produced Plasma from C_{60} Molecules"*, Opt Comm **112** 21 (1994).

X

Y

Z

Zavriyev 1990 A Zavriyev, PH Bucksbaum, HG Muller and DW Schumacher, *"Ionisation and Dissociation of H_2 in Intense Laser Fields at 1.064 μm, 532 nm, and 355 nm"*, Phys Rev A **42** 5500 (1990).

Zweiback 1999 J Zweiback, T Ditmire and MD Perry, *"Femtosecond time-resolved studies of noble gas cluster dynamics"*, Phys Rev A **59** to be published (1999).